

UNIVERSITÀ DEGLI STUDI DI NAPOLI “FEDERICO II”



Facoltà di Scienze MM. FF. e NN.
Corso di Laurea in Fisica

Development of the RPC control and
monitoring system in CMS; first muon
trigger results with 2006 cosmic ray runs

Relatori:

Ch.mo prof. Crisostomo Sciacca
Dott. Pierluigi Paolucci

Candidata:

Anna Cimmino
Matr. 60/953

Anno Accademico 2005/2006

Introduction

The Standard Model (SM) predicts the existence of a yet to be seen particle, the Higgs boson. In this theoretical model, the Higgs boson is held responsible for electroweak symmetry breaking. Although its great merits, the SM is still unsatisfactory from several points of view. Many extensions of the SM, like Supersymmetry, try to overcome these difficulties by introducing an entire new class of undiscovered particles. Regardless of the correctness of the above statements, there is widespread consensus that new physics must appear at energies higher than those reached by present particle accelerators. It was the quest for the Higgs boson, the desire to investigate the limits of the Standard Model and its possible extensions, that have brought to the construction of the Large Hadron Collider (LHC), that will be the most powerful particle accelerator ever. The LHC is a proton - proton collider with 14 TeV center of mass energy and a design luminosity of $10^{34} \text{ cm}^{-2} \text{ s}^{-1}$. These numbers make the LHC a challenging machine to construct and operate. This holds true also for the main LHC detectors: Atlas, CMS, Alice, and LHCb. In CMS, the challenges are: the complexity of the detector (7 different detector technologies), the high number of frontend electronic channels ($\sim 10^7$), an input rate of 10^9 interactions per second, a trigger able to reduce the frequency by a factor 10^5 and online computer farms with a storage capability of $\sim 10^2$ Hz at data rates of $\sim 10^2$ MB/s. With such a complex detector, it is crucial to design and develop a Detector Control System (DCS) able to verify the correct functioning of all the experiment. The DCS must control and monitor the detectors, electronic equipment, all related subsystems, hardware and software components of trigger and of the data acquisition system. Therefore, the DCS has to control and monitor about 300000 components and it must be integrated in the data acquisition system.

As physics experimental apparatuses grow in size and complexity, the number of electronic channels and the sophistication of auxiliary systems increase proportionally. In this scenario, the DCS assumes a key role. Its functionalities have extended well over the simple control and monitoring of the experiment. DCSs, nowadays, are highly advanced and automated online data acquisition systems, with less stringent requirements compared to the DAQ. The CMS DCS is based on the commercial software PVSS. The

later offers all the functionalities of a SCADA software. Unfortunately, this is not enough for particle physics. To meet the very unique requirements of the LHC experiments, a dedicated team of CERN control experts have tailored on PVSS an additional software tool, the JCOP Framework.

The LHC will start its pilot run in the year 2007. To prepare for this event the CMS Commissioning Task Force proposed to test a slice of the detector in presence of B field. This test was the Magnet Test & Cosmic Challenge (MTCC), conducted in the summer of 2006. The MTCC aimed to check key installation and maintenance strategies and to demonstrate the operation of CMS as a collective system. All subdetectors have participated to the MTCC, including the RPCs. To operate singularly and as a whole, almost every aspect of CMS, from the detector to the software, had to be operational. This included a fully working DCS, responsible for the correct functioning of the experiment.

The work described in this thesis was focused on the design and development of the DCS for the RPC detectors and its optimization for the MTCC. The main aims of the RPC DCS are to control and monitor more than 1000 chambers, ~ 100000 frontend electronic channels, trigger electronics, and all related subsystems. All RPC hardware components and software tools, chosen by the CMS collaboration, have been carefully analyzed and studied before designing the RPC DCS. This system has been developed to be comprehensive, scalable and user friendly.

This thesis is organized as follows. In the first chapter we review the principal characteristics of the LHC and its physics potential. The merits and the limits of the electroweak SM are concisely reviewed. Chapter two is dedicated to the description of the detector CMS, its subsystems and its trigger. Particular attention is given to the muon system and muon trigger. The RPC chambers are described in detail: their operational principle and their construction choices, motivated by muon trigger requirements. The functionalities of the DAQ, RCMS and DCS, as well as their specific requirements in CMS are given in chapter three. How these requirements have been fulfilled in the development of the RPC DCS system are also argument of the third chapter. The work done for the integration of the control system in the central CMS DCS for its use during the MTCC introduces the fourth chapter. This conclusive chapter aims to show the correct functioning of the RPC DCS and its role in the MTCC. The slow control data, acquired in this occasion, is presented along with preliminary chamber data.

Contents

Introduction	i
1 Physics at the Large Hadron Collider	1
1.1 Theoretical Introduction	1
1.1.1 The Standard Model	1
1.1.2 Beyond the Standard Model	5
1.2 The Large Hadron Collider	7
1.2.1 Design Considerations	7
1.2.2 Physics at the LHC.	12
2 The Compact Muon Solenoid Detector	16
2.1 Overall Design	16
2.2 The Central Tracker Detector	19
2.2.1 The Pixel Detector	19
2.2.2 The Strip Tracker Detectors	19
2.3 The Electromagnetic Calorimeter	20
2.4 The Hadronic Calorimeter	22
2.5 The Muon System	22
2.5.1 The Drift Tubes	23
2.5.2 The Cathode Strip Chambers	24
2.5.3 Resistive Plate Chambers	25
2.6 The RPC Detectors: a closer look	25
2.6.1 Avalanche Formation in Gaseous Detectors	27
2.6.2 Signal Formation in RPCs	31
2.6.3 Specific conditions and requirements for CMS RPCs .	33
2.7 The RPC Detectors: preliminary results on chamber produc- tion	39
2.8 The CMS Trigger	42
2.8.1 The Calorimetric Trigger	45
2.8.2 The Muon Trigger	45

3 Development of the RPC Control and Monitoring System in CMS	49
3.1 Data Acquisition System in CMS	50
3.2 Run Control in CMS	52
3.3 The Detector Control System	56
3.3.1 General Requirements	56
3.3.2 DCS Architecture	57
3.4 DCS software tools	59
3.4.1 PVSS	60
3.4.2 JCOP Framework	61
3.5 The RPC DCS: hardware system	63
3.5.1 Power system: the High and Low Voltage systems . .	63
3.5.2 Temperature Monitoring	70
3.6 Design and Development of the RPC DCS	75
3.6.1 Architecture of the DCS	75
3.6.2 The Final State Machine: design and implementation	77
3.6.3 Alarm Handling	80
3.6.4 The Configuration and Condition Databases	81
3.6.5 The Graphical User Interface	82
3.6.6 Integration in the Central CMS DCS	90
4 The MTCC: preliminary results	92
4.1 Main objectives	92
4.2 Subdetectors in MTCC	94
4.3 MTCC Phase I and Phase II	96
4.4 The RPC DCS in the MTCC	98
4.5 Results of DCS data	100
4.6 Results of chamber data	106
Conclusions	110
Acknowledgments	112
Bibliography	113

Chapter 1

Physics at the Large Hadron Collider

The Large Hadron Collider (LHC) is a proton-proton storage ring under construction at the CERN laboratories in Geneva. It is expected to be up and running by the end of the year 2007. The LHC will work at a center of mass energy of 14 TeV and with a design luminosity of $10^{34} \text{ cm}^{-2} \text{ s}^{-1}$. The collider will also allow the study of heavy ion physics, i.e. Pb. When the Pb-beam is present, which will not be before 2008, the design luminosity will be only $10^{27} \text{ cm}^{-2} \text{ s}^{-1}$, while the center of mass energy will increase to 1150 TeV.

The focus of this chapter is to present a concise overview of the theoretical motivations, of the design, and of the physics program of the LHC. In Section 1.1 a short introduction of the Standard Model is given, focusing on its opened issues and possible extensions. The main design characteristics and the physics potential of the LHC is presented in Section 1.2.

1.1 Theoretical Introduction

1.1.1 The Standard Model

The Standard Model (SM) of particle physics [1] is a quantum field theory capable of explaining strong, weak and electromagnetic interactions between elementary particles: gravitation is not relevant at the distances and mass scales typical of particle physics. The SM accomplishes this goal through two gauge theories:

- the theory of strong interaction or Quantum Chromodynamics (QCD), based on the $SU(3)_C$ symmetry group.
- the theory of weak and electromagnetic interaction or electroweak

Standard Model, based on $SU(2)_I \otimes U(1)_Y$ group, direct product of isospin and hypercharge symmetry.

A comprehensive description of these theories is beyond the scope of this work. However, the main features of the Electroweak SM are reviewed in the present section.

Electroweak Standard Model

The attempt to unify electromagnetic and weak forces brought to the formulation of the Glashow-Salam-Weinberg gauge theory of electroweak interactions; the relevant symmetry group is $SU(2)_I \otimes U(1)_Y$ [2]. Thus, the theory holds three SU(2) gauge fields, $W_{1,2,3}^\mu$ and one U(1) gauge field B^μ , which couple to the fermions by two coupling constants, g and g' . The corresponding physical fields are linear combinations of these four gauge fields. The charged bosons, W^+ and W^- are given by

$$W_\mu^\pm = \frac{(W_\mu^1 \mp W_\mu^2)}{\sqrt{2}},$$

while the photon and the neutral Z boson are obtained, by the introduction of the Weinberg angle θ_W , as follows:

$$\begin{aligned} Z_\mu &= W_\mu^3 \cos \theta_W - B_\mu \sin \theta_W, \\ A_\mu &= W_\mu^3 \sin \theta_W + B_\mu \cos \theta_W. \end{aligned}$$

The A_μ field is identified with the electromagnetic field by requiring the identities:

$$g \sin \theta_W = g' \cos \theta_W = e.$$

In this purely symmetric gauge theory all particles are massless. In fact, gauge invariance forbids a mass term in the Lagrangian for both Abelian and non-Abelian gauge fields. But this would implies that the associated forces must have a long range. As this is true for photons and electromagnetism, it does not hold for weak interactions. The W^\pm and Z bosons are believed to acquire mass through spontaneous symmetry breaking, i.e. the Higgs mechanism, which preserves gauge invariance and renormalization. It must be pointed out that the U(1) symmetry is left unbroken and the photon remains massless.

An $SU(2)$ doublet complex scalar field, the Higgs field, is introduced in the theory. The Lagrangian density for the Higgs sector is:

$$\mathcal{L}_H = (D^\mu \phi)^\dagger (D_\mu \phi) - \mu^2 \phi^\dagger \phi - \lambda (\phi^\dagger \phi)^2, \quad (1.1)$$

where $\mu^2 < 0$, $\lambda > 0$ and

$$D^\mu = \partial^\mu + ig\frac{\tau}{2}W^\mu + ig'YB^\mu. \quad (1.2)$$

The Higgs potential has its minimum for

$$\phi^\dagger\phi = \frac{-\mu^2}{2\lambda} = \frac{v^2}{2}. \quad (1.3)$$

Thus, the ground state, ϕ_0 , is degenerate and choosing a particular value for it leads to spontaneous symmetry breaking. Without loss of generality, we can write:

$$\phi_0 = \begin{pmatrix} 0 \\ v/\sqrt{2} \end{pmatrix}.$$

Boson masses derive from the coupling of the boson fields to the non-zero vacuum value of the Higgs field. The fermions, instead, acquire mass through a Yukawa-like coupling terms put “by hand” in the electroweak Lagrangian. This difference in treatment between bosons and fermions has an important consequence in the theory: the coupling of the Higgs field to the gauge fields is determined by gauge symmetry, while the Yukawa-like coupling of fermions is not a gauge interaction. Thus, the fermion masses are free parameters.

The Higgs mechanism gives rise to a scalar massive gauge boson, i.e. the Higgs boson. Its mass depends on the two parameters v and λ :

$$m_H = \sqrt{2\lambda}v.$$

The value of v can be inferred from the masses of the W_\pm and Z bosons:

$$m_W = \frac{1}{2}vg \quad \text{and} \quad m_Z = \frac{gv}{2\cos\theta_W}, \quad (1.4)$$

Instead, λ is characteristic of the Higgs field and can not be determined from experimental quantities. This makes the Higgs mass the only unknown parameter of the Standard Model.

The Higgs Mass

As shown above, the Higgs mass is not predicted by the SM; however it is possible to place strong theoretical and experimental constraints on its value.

A lower bound can be derived asking for λ to remain positive at all energy scales. A negative value, in fact, would imply an unbound potential and vacuum instability[3]. The resulting lower limit for the Higgs mass actually

depends on the energy scale Λ up to which the SM is supposed valid. On the other hand, λ is the coupling constant for the Higgs self-interaction. As such, it runs increasing with the energy. If λ is allowed to grow indistinctively, the theory becomes non-perturbative at a certain energy scale. For it to remain valid at all energies, we must require an upper bound on λ , resulting in an upper bound on the Higgs mass too (*triviality bound*). Figure 1.1

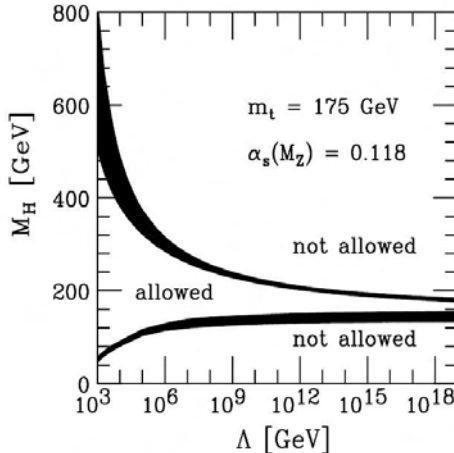


Figure 1.1: Theoretical bounds on the Higgs mass as a function of the energy scale Λ . The shaded areas take in account the uncertainties in the calculations [4].

shows that, supposing the SM valid up to the Plank scale ($\Lambda = 10^{19} \text{ GeV}$), the Higgs mass must be in the range $130\text{-}200 \text{ GeV}/c^2$. With the alternative assumption, $\Lambda \approx \text{TeV}$, m_H must be lighter than $700 \text{ GeV}/c^2$.

Experimental bounds on m_H are given by measurements at the LEP, SLC, and Tevatron colliders [5] [6]. Direct search has excluded the region below $114.4 \text{ GeV}/c^2$ at 95% confidence level. An upper limit can be set fitting electroweak data and taking m_H as a free parameter. Indeed it can be proven that all electroweak parameters, at the first order, depend logarithmically on m_H [7]. Figure 1.2 shows the trend of the χ^2 of the fit as a function of the Higgs mass. The curve's minimum falls in the excluded region (highlighted in yellow), but it is still safe to say, the theory prefers a light Higgs boson. The upper bound of $219 \text{ GeV}/c^2$ is set with a 95% confidence level.

The existence of the Higgs boson remains the most significant prediction of the electroweak theory which has not been verified by experimental proof. The search for this elusive particle is, therefore, the highest priority at present and future accelerators.

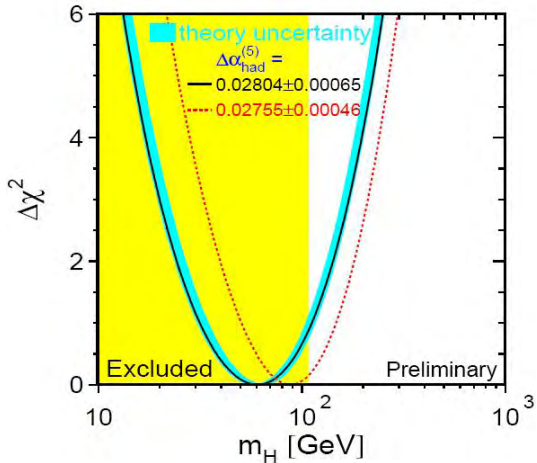


Figure 1.2: $\Delta\chi^2 = \chi^2 - \chi^2_{min}$ of the fit of electroweak measurements done at LEP, SLC and Tevatron [5].

1.1.2 Beyond the Standard Model

The Standard Model has been outstandingly successful in accounting for essentially all experimental data up to date. It has been tested, over a wide range of energies, to a precisions of the order 0.1% [8]. However, there are a number of shortcomings and problems, aside from the fact that the Higgs boson has not yet been observed. As we have already seen, theoretical bounds on the Higgs mass can be derived from the request that the theory remains valid up to a given energy scale. Thus, it is natural to seek for a truly fundamental theory, which holds at higher energies and, possibly, accounts for all interactions. In the SM, in fact, strong interactions are described beautifully by QCD, but they are not unified with the electroweak description. At the same time, gravity, whose strength would be comparable with that of the other interactions at the Plank scale, is completely left out. Moreover, at one loop level, we find quadratically divergent contributions to the Higgs mass. For the SM to be valid at high energy scales, these divergences must be cancelled by mass counterterms. This would imply a fine tuning at every perturbation order which, even if possible, appears quite artificial (*naturalness problem*).

The most serious drawback in the SM is the hierarchy problem [9]. In simple words, there is no explanation for the fact that particle masses should be significantly smaller than the energy scale up to which the theory is valid. In addition, the SM does not explain the origin of six flavors in both quarks and leptons, nor CP violation. Finally, the number of free parameters¹ ap-

¹Neglecting neutrino masses and mixing, the total number of free parameters in the Electroweak SM is 17: nine fermion masses (neutrinos are considered massless), three

pears too high to not be artificial.

SuperSymmetry

For all reasons previously exposed, the Standard Model is accepted as an effective theory, valid to some energy scale Λ while theorists are working on the appealing idea of a wider unified theory. In this contest SuperSymmetry (SUSY) [10] is the currently favored solutions. SUSY predicts that all particle have a supersymmetric partner, a sparticle, with opposite statistics. So far, no supersymmetric partner of any known particle has been observed. So, supersymmetry, if it exists, is broken at all energy scale accessible at present day accelerators. Nevertheless, SUSY offers many attractive features. First of all, it provides the only known solution to the hierarchy problem. In fact loop contributions from fermions and bosons have opposite signs and therefore cancel in the corrections to the Higgs mass. In addition, some (extended) supersymmetric theories are completely finite, in the sense they do not force to deal with and manipulate infinite quantities. The third, and most recent, reason for supersymmetry being such an appreciated theory is that it appears to be an indispensable ingredient for superstring theories.

An important phenomenological consequence comes from the fact that the theory contains a multiplicative quantum number, R-parity. R-parity takes opposite value for particle and sparticle and its conservation is assumed by cosmological arguments [11]. This means that sparticles are produced in pairs and they all decay to the Lightest Supersymmetric Particle (LSP). In most theories, the LSP is a neutral, stable, massive and weakly interacting particle: a perfect candidate for cold dark matter.

The simplest supersymmetric model, called the Minimal Supersymmetric Standard Model (MSSM), requires at least two Higgs doublets, corresponding to five Higgs particles: two charged bosons, H^\pm , two scalar bosons, h and H , and one pseudo-scalar, A . The masses of these particles can be determined through radiative corrections if the sparticles have masses at the TeV scale.

Extra Dimensions

The idea of extra dimensions was historically originated from the attempt of Kaluza and Klein to unify gravity and electromagnetism. Nowadays, extra dimensions are a key ingredient of string theory. They could allow unification of all four interactions if they were much larger than the Planck length [13]. The idea is that the presence of extra dimensions lowers the characteristic energy scale of quantum gravity to the TeV scale.

CP Violation

angle and a non-zero phase in the CKM matrix, two coupling constants the Higgs vacuum expectation value, and the Higgs mass.

Another way of testing the internal coherence of the SM can come from precise studies of CP-violation [14] effects. In the SM, it is a consequence of the quark mass generation mechanism and of the presence of a non-zero phase in the elements V_{ub} and V_{td} of the quark-mixing CKM matrix. Up to today, all the experimental evidence confirms the CP-violation predicted by the SM. The problem is that this amount of CP-violation is insufficient to explain baryogenesis² and matter-antimatter asymmetry in the universe.

Since its discovery, CP-violation has been intensely studied in the neutral K meson decays. However, larger effects are present in the B^0 system, which is the main motivation for the construction of B-factories.

1.2 The Large Hadron Collider

1.2.1 Design Considerations

As explained in the previous section, the main objective of modern particle physics is the discovery (or exclusion) of the SM Higgs boson and of new physics at the TeV scale. To explore these energies, the choice naturally falls on hadron colliders. In circular colliders, in fact, the synchrotron energy lost per turn is $\propto E^4/(m^4 R)$, where E and m are the energy and mass of the accelerated particle and R is the colliders radius. Lepton machines would need enormous dimensions to reach energies of ~ 500 GeV per beam. On the other hand, protons, which are 2000 times heavier than electrons, suffer less energy loss by synchrotron radiation and are easily produced. The drawback is that protons are not elementary particles. So, the center of mass rest frame is unknown and only a fraction of the proton's energy is exchanged in the scattering. This forces to reach energies well above the mass of the particle to be produced, but, on the other hand, it allows to explore a wide range of energies with fixed energy beam.

Let us consider a process with cross section σ . Then, the production rate R is given by:

$$R = L\sigma. \quad (1.5)$$

The factor L is called luminosity³ and is specific to the collider's parameters. That is, it does not depend on the nature of the colliding particles, nor on the

²In cosmology, baryogenesis indicates all physical processes responsible of an asymmetric production of baryons and anti-baryons in the very early universe.

³Luminosity represents the number of collisions per unit time and cross-sectional area of the beams. For circular accelerators, colliding bunches of n_1 and n_2 particles at a frequency f , the luminosity reads:

$$L = f \frac{n_1 n_2}{4\pi\sigma_x\sigma_y},$$

undergone interactions. Therefore, to obtain the highest possible statistics, one could operate on the luminosity and/or the collision energy. Figure 1.3 shows the cross sections for different processes as a functions of the center of mass energy in p - p collisions. As it can be seen, the Higgs cross section increases steeply with \sqrt{s} , while the background remains almost constant. Therefore, the highest possible center of mass energy should be used.

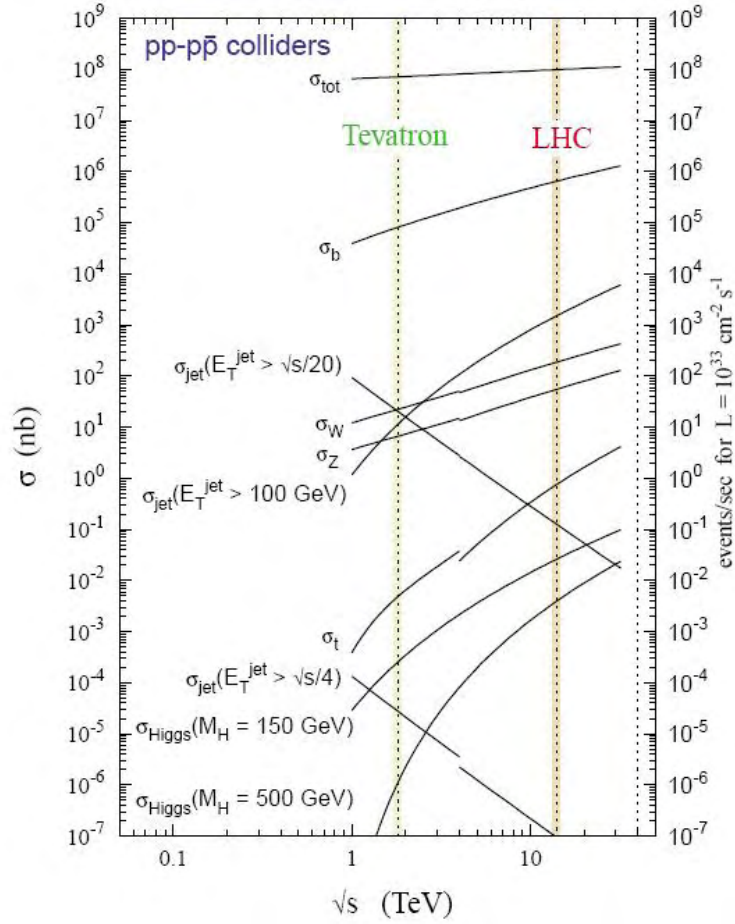


Figure 1.3: Production cross sections (scale on the left) and event rates (scale on the right) for various scattering processes at hadron colliders as a function of the machine center of mass energy (Tevatron and LHC operating c.m. energies are explicitly shown) [15].

To compensate for small production cross sections, as in the Higgs case, a high luminosity must be achieved. This has the disadvantage of increasing

where σ_x and σ_y characterize the Gaussian transverse beam profiles in the horizontal and vertical directions.

the total number of events (that depends linearly on L) so many events overlap during the same bunch crossing (*pile up*). A way to reduce the pile-up while keeping constant the luminosity is to increase the collision frequency and reduce the number of particles per bunch. This, however, poses more and more demanding timing requirements on the detectors.

Baring all this in mind and remembering the issues presented in Section 1.1, particle physicists from around the world, proposed, in the early 1980's, the construction of what will be the most powerful hadron collider ever built: the Large Hadron Collider [16]. The main LHC parameters are listed in Table 1.1.

Parameter	$p - p$	^{208}Pb
center of mass energy (TeV)	14	1148
Number of particles per bunch	1.1×10^{11}	$\sim 8 \times 10^7$
Number of bunch	2808	608
Design luminosity ($cm^{-2}s^{-1}$)	10^{34}	2×10^{27}
Bunch length(mm)	53	75
Beam radius at interaction point (μm)	15	15
Time between collisions (ns)	24.95	124.75×10^3
Circumference (km)	26.659	26.659
Dipole field (T)	8.3	8.3

Table 1.1: LHC main parameters for proton and Pb beams.

The design luminosity will be reached only after a start-up phase at low luminosity ($L = 2 \times 10^{33} cm^{-2}s^{-1}$) that could last until 2010, since part of the beam dump and collimating system are staged. This period will be used for the study of high cross section phenomena, to prepare for the high luminosity run, and to complete the detectors. The beam's energy will be limited to 7 TeV due to the maximum dipole magnetic field. Higher energies could have been reach with a larger curvature radius. But the LHC will use the already existing tunnel of the LEP experiment (diameter $\sim 27 Km$) to limit construction costs. The LHC will also allow the study of heavy ion physics, i.e. Pb. The luminosity and center of mass energy reached will be over 30 times higher than at all present day accelerators, allowing to further extend the range of heavy-ion physics to include studies of hot nuclear matter.

Experimental Challenges at LHC.

The proton-proton inelastic cross-section at $\sqrt{s} = 14$ TeV is roughly 70 mb (see Figure 1.3). At design luminosity, the LHC general purpose detectors will therefore observe an event rate of 6.5×10^8 inelastic events/s. This leads to a number of formidable experimental challenges[17].

First of all, the event selection process, i.e. the trigger, must reduce the \sim billion interactions/s to no more than $\sim 10^2$ events/s, for storage and subsequent analysis. The short time between bunch crossings, 25 ns, has major implications for the design of the readout and trigger systems (see Section 2.8). It is enough to say that, in both general purpose LHC detectors, the Level-1 trigger alone takes about $3\mu\text{s}$ to make its decision. Unfortunately, new events may occur at every bunch crossing. In order to avoid dead-time, pipelined trigger processing and readout architectures are required.

At the design luminosity a mean of 20 minimum-bias events⁴ will be superimposed on the event of interest. This number results from eq. 1.5 and from the fact only 80% of the bunches will be full. Each collision will give rise to an average of 50 charged tracks, i.e. around 1000 charged particles will emerge from the interaction region every 25 ns. The products of an interaction may be confused with those from other interactions in the same bunch crossing. This problem is known as pileup. Its effects can be reduced by using highly granular detectors with good time resolution, at the expense of having a large numbers of electronic channels and high costs.

The large flux of particles coming from the interaction region leads to high radiation levels, requiring radiation-hard detectors and front-end electronics.

The LHC Experiments.

Figure 1.4 gives a schematic view of the LHC rings, its preaccelerators, and the four interaction point locations. A particle detector is being installed at each one of these points: ATLAS [18], CMS [19], ALICE [20], and LHCb [21]. A fifth experiment, TOTEM [22], will be situated in the far forward regions of CMS. TOTEM will measure the total $p - p$ cross section and study elastic and diffractive processes at the LHC. Both ATLAS and CMS are general purpose detectors, whose research domain is very large, although focused on the search for new particles. Whereas ALICE and LHCb are respectively specialized in heavy-ions physics (quark-gluon plasma) and b-physics (CP violation). In the previous section we reviewed the main challenges for ATLAS and CMS. ALICE, instead will have to handle events containing $\sim 10^4$ tracks, while the main challenges for LHCb detector will be an efficient online selection of events containing b-flavored hadrons, particle identification and vertex reconstruction.

Despite the common scope, ATLAS and CMS have a very different design: CMS has a solenoid 4 Tesla magnetic field, while ATLAS uses three sets of air-core toroid magnets and an additional inner solenoid. The advantage of a toroidal magnet field is a constant transverse momentum resolution as a

⁴Here we call minimum-bias events the bulk of events produced in $p - p$ inelastic collisions.

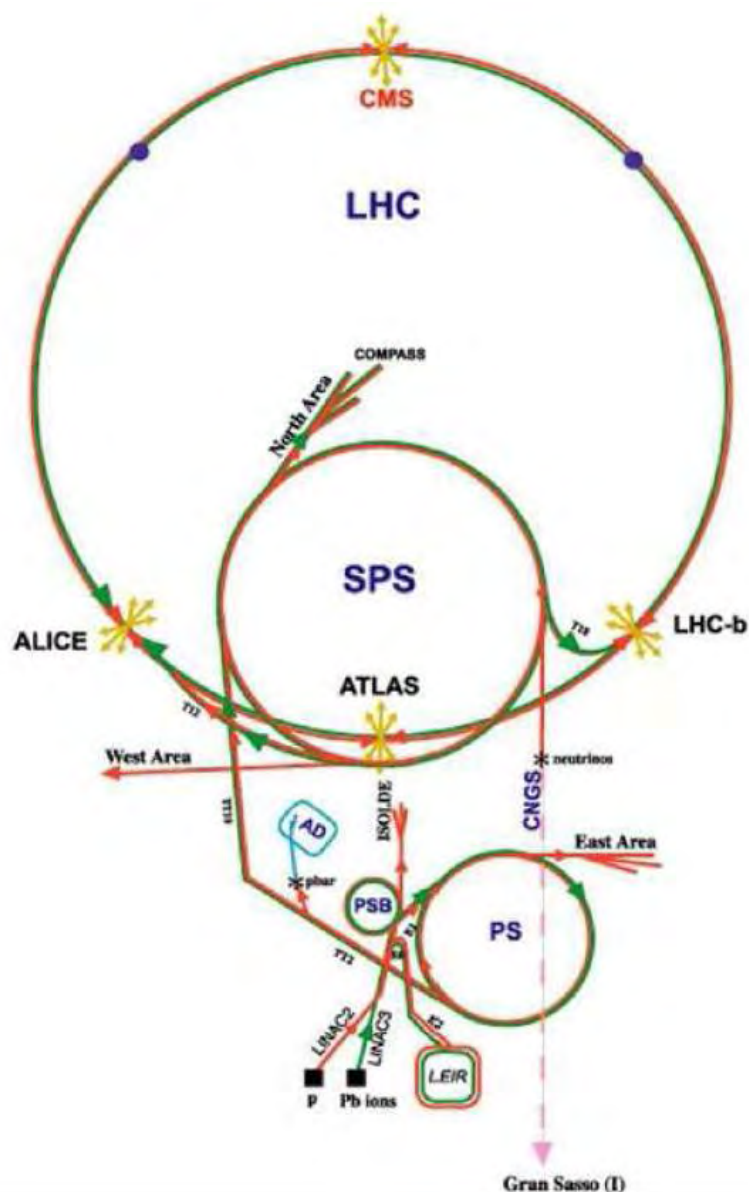


Figure 1.4: Schematic illustration of the LHC rings with the location of the four interaction points

function of pseudorapidity⁵. A good momentum resolution can be achieved without the use of an inner tracker and with modest chamber space resolution and alignment (of order $\sim 100 \mu\text{m}$). In contrast, an iron-core solenoid can generate an intense magnetic field. The system is, therefore, compact. The calorimeters can be put inside the magnet improving the detection and energy measurements of electrons and photons. Moreover, track exiting the yoke point back to the interaction point, but multiple scattering in the yoke itself degrades the resolution of the muon system. The CMS detector is analyzed in more detail in Chapter 2.

1.2.2 Physics at the LHC.

Thanks to the high center of mass energy and luminosity, the LHC has an outstanding physics potential. This machine will, hopefully, give a definite answer to the existence of the Higgs boson. It will also allow electroweak precision measurements, study of quark-gluon plasma and search for new physical phenomena (supersymmetry) at the TeV scale. The LHC will vaunt $b\bar{b}$ and $t\bar{t}$ production rates respectively of 10^{12} evts/year ($L = 2 \times 10^{32} \text{cm}^{-2}\text{s}^{-1}$ at LHCb) and 10^{12} evts/year ($L = 10^{33} \text{cm}^{-2}\text{s}^{-1}$). This will consent extensive studies of b and t-physics. An overview of the LHC physics program is given in the present section.

The SM Higgs

In $p - p$ collisions the main mechanism for Higgs production, at the SM tree level, are displayed in figure 1.5. The cross section for the different processes is shown in figure 1.6 left as a function of the Higgs mass. Gluon fusion is the dominate process. Boson fusion becomes comparable only for $m_H \gtrsim 800 \text{ GeV}/c^2$, but it offers an excellent signature with two forward jets in the final state. Also associated production processes, despite the low cross section, allow an easy background suppression. All the cross sections are of the order of a few picobarns. At the LHC's design luminosity this means an event rate of 10^2 Hz.

Figure 1.6 right shows the branching ratio for several Higgs decay channels as a function of m_H [23]. For $m_H < 130 \text{ GeV}/c^2$, the channel $H \rightarrow b\bar{b}$ dominates. However, the QCD jet background is so high at LHC that it will be almost impossible to observe this decay (except maybe by exploiting associated $t\bar{t}H$ or WH production.) The most promising channel is $H \rightarrow \gamma\gamma$ which despite the very low branching ratio ($\sim 10^{-3}$) has a very clean signature. The main background comes from π^0 decay.

For higher Higgs masses ($130 \text{ GeV}/c^2 \lesssim m_H \lesssim 600 \text{ GeV}/c^2$), the production of $W^{(*)}W^{(*)}$ and $Z^{(*)}Z^{(*)}$ pairs becomes possible. Still, purely hadronic are non accessible. The useful channel are $H \rightarrow Z^{(*)}Z^* \rightarrow 4l$

⁵Pseudorapidity is defined as: $\eta = -\ln \tan \frac{\theta}{2}$, where θ is the angle between the particle's momentum and the beam direction.

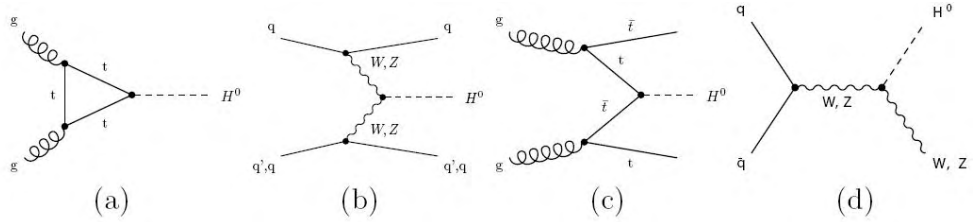


Figure 1.5: Higgs production mechanisms at tree level in proton-proton collisions: (a) Gluon-gluon fusion; (b) W and Z fusion; (c) $t\bar{t}$ associated production; (d) W and Z associated production.

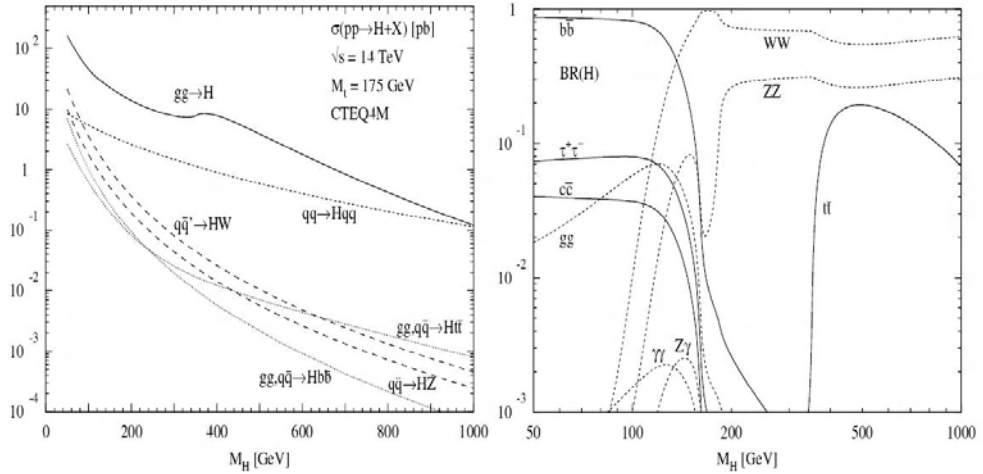


Figure 1.6: Higgs production cross section (left) and branching ratios (right) as a function of the Higgs mass [23].

and $H \rightarrow W^{(*)}W^{(*)} \rightarrow ll\nu\nu$. The latter becomes important for $m_H \approx 2m_W$, where the ZZ branching ratio drops to 20%. The four lepton decay of the ZZ boson pair is a gold-plated channel, with a clean experimental signature.

For $m_H > 600$ GeV/ c^2 the Higgs cross section becomes significantly small. Semi-leptonic channels ($H \rightarrow ZZ \rightarrow ll\nu\nu$, $H \rightarrow ZZ \rightarrow lljj$, and $H \rightarrow WW \rightarrow lljj$), that have a higher branching ratio compared to the purely leptonic decays, must be used. The presence of neutrinos imply a high missing transverse energy.

Supersymmetry

As already discussed, the MSSM (Minimal Supersymmetric Standard Model) predicts the existence of five Higgs bosons: two charged bosons, H^\pm , two scalar bosons, h and H , and one pseudo-scalar, A . The charged

Higgs bosons decay predominantly to $\tau\nu$. For the neutral Higgs bosons the dominant decays modes are those to $b\bar{b}$ and $\tau^+\tau^-$ [23], but the former is hidden by the large background of b -jets. The observation of MSSM Higgs bosons will therefore rely on the identification of leptons coming from τ decays and τ -jets.

All possible supersymmetric theories predict a rich phenomenology of supersymmetric particles. At the LHC, the dominant SUSY process is expected to be the production of squarks and gluinos, both strongly-interacting particles with QCD-type cross sections[11]. These sparticles are thought to have a very spectacular signatures due to an abundance of leptons and jets in the final state and large missing energy. This is due to the fact in every SUSY event two neutral LSPs are produced and escape detection. These can be separated from SM processes selecting events with many high- p_t jets and large missing energy. The LHC general purpose experiments, ATLAS and CMS, will certainly be able to confirm or deny the existence of supersymmetry.

Top physics

The top quark's mass, m_t , is a fundamental parameter of the Standard Model. It enters into calculations of the W and Z boson masses through higher order loop effects. Furthermore, the Higgs boson mass depends logarithmically on the top quark mass, and so a precise measurement of the top quark's mass leads to limits on the allowed mass of the Higgs boson. Figure 1.7 shows how this precise measurements of m_t , combined with the W boson mass measurement, restrict the allowed Higgs boson mass range in both the Standard Model and in the Minimal Supersymmetric Standard Model. The present value of the top's mass is set by the CDF collaboration to $m_t = 170.9 \pm 2.2(\text{stat}) \pm 1.4(\text{syst})$ GeV [12].

The LHC, with its top production cross section of 830pb (figure 1.3), will act as a t -factory. The study of $t\bar{t}$ production and decay processes are of great interest. It could complete our knowledge of the electroweak spontaneous symmetry breaking since the top quark is the only known particle with a mass comparable to the electroweak energy scale. Since the top quark decays before it can hadronize. At the LHC the main decay channel is $t\bar{t} \rightarrow W^+W^-b\bar{b}$, with one leptonic and one hadronic W decay. The hadronic part will be used to reconstruct the top mass with a final uncertainty better than 2 GeV. The leptonic part will be used in the event trigger.

B-physics

At the LHC the $b\bar{b}$ cross section will be $\sim 500\mu\text{b}$. The main interest is the study of the B^0 decay and CP-violation. B mesons are identified through their leptonic decays. The difficulty is that these leptons are quite soft and are covered by a huge background due to pion, kaon and charm decays. The LHCb experiment is dedicated to b -physics, but also ATLAS and CMS will

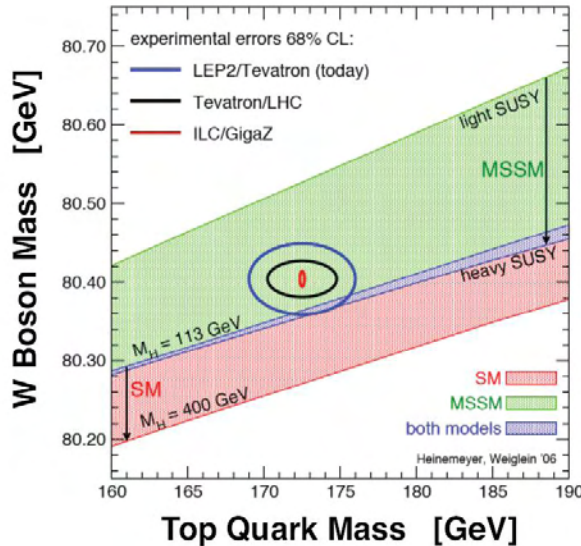


Figure 1.7: Limits on the Higgs boson mass from measurements of the masses of the top quark and W boson [12].

study it during the low luminosity phase.

Quark-gluon plasma physics

As already mentioned, at the LHC it will be possible to collide lead ion beams at a center of mass energy of 1150 TeV. These collisions will allow the study of strongly interacting matter in unprecedent conditions of energy and temperature. At these conditions, a phase transition from ordinary hadronic matter to a plasma of deconfined quarks and gluons is supposed to take place. Since it is believed that the opposite transition occurred $\sim 10\mu\text{s}$ after the Big Bang, these study will shed light on the evolution of the early universe. At the LHC, the ALICE detector is a dedicated experiment, optimized to explore the proprieties of quark-gluon plasma. Also ATLAS and CMS will participate at the heavy ion physics programm.

Chapter 2

The Compact Muon Solenoid Detector

The Compact Muon Solenoid (CMS) [19] is a general purpose detector designed to run at the highest luminosity at the LHC. It is optimized for the search of the SM Higgs boson over the mass range from $90 \text{ GeV}/c^2$ to $1 \text{ TeV}/c^2$, but it will also allow the detection of other possible electroweak symmetry breaking mechanisms. At low luminosity, the study of top, beauty, and tau physics will be possible. In addition, CMS will cover different aspects of the heavy ion physics programm.

The general design of CMS and of its subdetectors is presented in the present chapter. Section 2.8 offers a concise but complete description of the CMS trigger system.

2.1 Overall Design

To meet the physical goals of the LHC programm, discussed in Section 1.2, the detector requirements for CMS are [25]:

- A good and redundant muon system. Good muon identification and momentum resolution is asked in the region $|\eta| < 2.5$.
- A high resolution electromagnetic calorimeter designed to observe the possible decay of the Higgs boson in two photons.
- A high quality inner tracker with of a good charged particle momentum resolution and reconstruction efficiency. Efficient triggering and offline tagging of τ and b -jets need a pixel detector close to the interaction region.
- A trigger and DAQ system able to work at high luminosity and bunch crossing frequency.

The design of CMS, schematically illustrated in Figure 2.1, follows these requirements. The detector is composed of a cylindrical section (the barrel), 21.6 m long and 15 m in diameter, closed by eight endcap disks (four per side) in the forward region. The entire structure weighs ~ 12500 tonnes. A longitudinal view of one quarter of the barrel region of CMS is shown in Figure 2.2. Please note the coordinate system in the low right corner. The

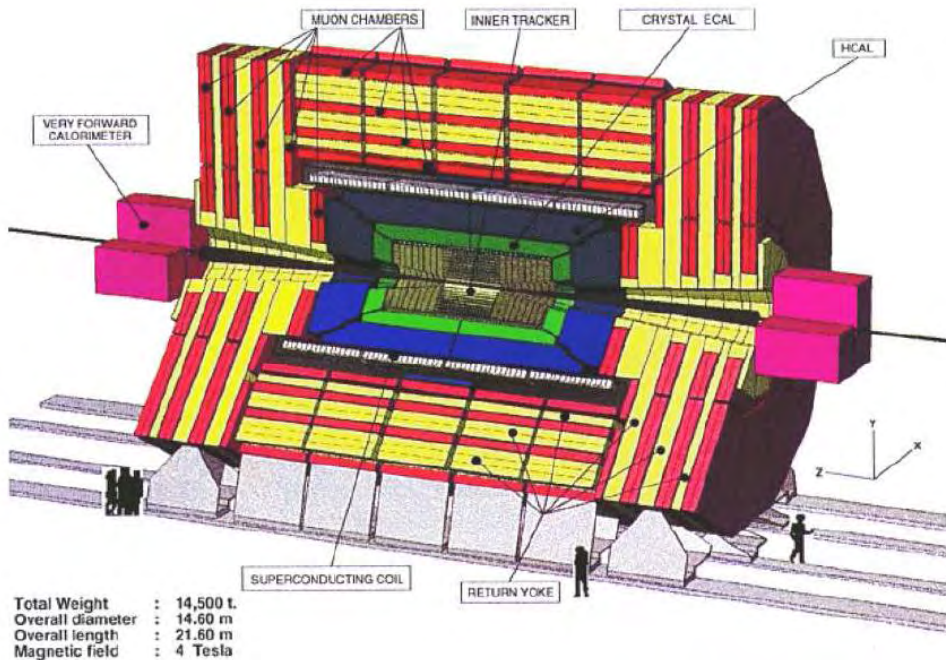


Figure 2.1: Overall layout of the CMS detector

origin coincides with the nominal collision point, the y -axis points vertically upward, the x -axis points toward the center of the LHC, and the z -axis points along the beam direction. The reconstruction algorithms, instead, use spherical coordinates based on the distance r from the z -axis, on the azimuthal angle from the x -axis in the $x-y$ plane, and on the pseudorapidity $\eta = -\ln \tan(\frac{\theta}{2})$. The polar angle θ is measured from the z -axis.

The magnetic field configuration influences the entire detector design. CMS has a 13 m long solenoid magnet, with an inner diameter of 5.9 m [26]. It will generate a magnetic field of 4 T, kept uniform by a massive iron return yoke instrumented with the muon chambers. The return field is large enough to saturate 1.8 m of iron (1.8 T), hence allowing the integration of four muon stations. Each station is made of several layers of aluminium drift tubes in the barrel region and cathode strip chambers in the endcap region. Resistive plate chambers complete the muon stations in both detector sec-

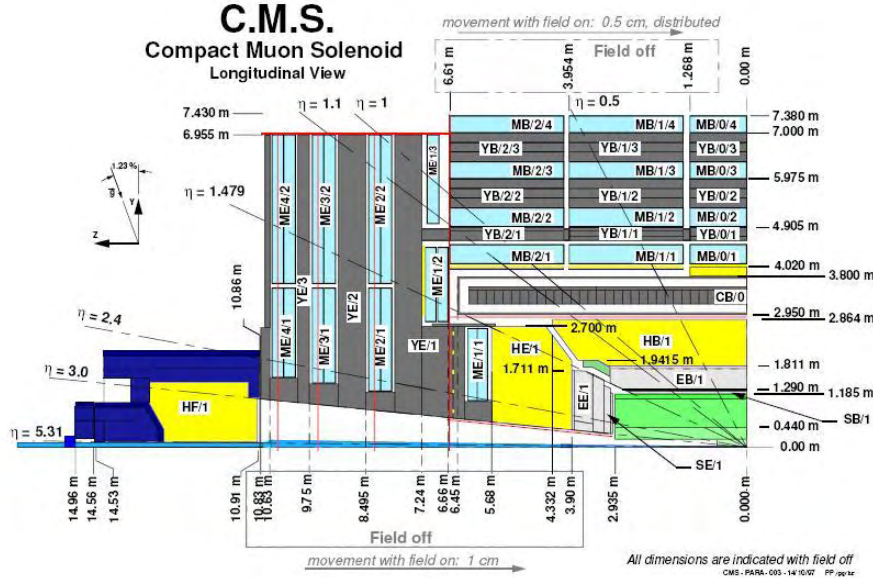


Figure 2.2: Longitudinal view of a quarter of the CMS detector.

tions insuring a geometrical coverage up to $|\eta| < 2.1$. The muon system is extensively described in Sections 2.5 and 2.6.

The inner tracker and calorimeters are accommodated inside the magnet coil. The tracker is composed of layers of silicon microstrip detectors, which provide the required granularity to deal with the expected high track multiplicity. In addition, 3 barrel layers and 2 endcap disks of silicon pixel detectors are located immediately around the interaction point. The pixels improve the measurement of the impact parameter of charged particles and of the position of secondary vertices. More information on the CMS tracker is given in Section 2.2.

The electromagnetic calorimeter (ECAL) uses ~ 8000 lead tungstate crystals covering the region $|\eta| < 3.0$. The endcap region is complemented by a lead and silicon preshower detector for π^0 rejection. The CMS ECAL, described in Section 2.3, is surrounded by a brass/scintillator sampling hadronic calorimeter (HCAL), always with coverage up to $|\eta| < 3.0$. A very forward iron/quartz fiber calorimeter extends this coverage to $|\eta| < 5.0$ and ensures that hadronic showers are sampled with almost 11 hadronic interaction lengths. The HCAL is further documented in Section 2.4.

2.2 The Central Tracker Detector

The inner CMS tracker [27] was designed to achieve, combined with the 4 T central magnetic field, a lepton momentum resolution of $\Delta p_t/p_t \approx 0.1p$ (p_t in TeV). This will allow to measure lepton charge up to $p_t \approx 2\text{TeV}$. In addition, using the high rate of precisely measured electrons from W and Z decays, frequent calibrations of the electromagnetic calorimeter cells will be possible. The high p_t isolated tracks ($p_t > 2\text{GeV}$) must be reconstructed with an efficiency of better than 95%, and high p_t tracks within jets with an efficiency of better than 90% over the pseudorapidity range $|\eta| < 2.5$.

Two different detector technologies have been chosen, each best matched to the task of satisfying our stringent resolution and granularity requirements in the high and lower particle density regions. These are the pixels (section 2.2.1) and silicon strips (section 2.2.2). All detectors are fast on the scale of 25 ns, allowing event pile-up to be limited to a single bunch crossing.

2.2.1 The Pixel Detector

It has already been stressed that important discoveries may depend on the ability of the tracking system to perform efficient flavour-tagging even at the highest luminosities. Several layers of silicon pixel detectors have been placed close to the interaction vertex to serve this purpose. The goal is to achieve an impact parameter resolution at high p_t of order $20\ \mu\text{m}$ in the transverse plane and $100\ \mu\text{m}$ in the z direction. The whole pixel detector consists of 4.4 million pixels: n-type silicon pixels with a size of $150\mu\text{m} \times 150\mu\text{m}$ on a p-type silicon substrate. It includes three barrel layers at mean radii of 4.4 cm, 7.3 cm and 10.2 cm, extending for a total length of 53 cm.

The significant charge is shared across neighboring cells resulting in expected hit resolutions of approximately $10\ \mu\text{m}$ and $15\ \mu\text{m}$ in the ϕ and z coordinates respectively. Similar resolutions, between 15 and $20\ \mu\text{m}$, are obtained in the end-cap pixels.

2.2.2 The Strip Tracker Detectors

The layers following the pixel are made by single-sided and double-sided silicon strip detectors (10 in the barrel and 12 in the endcaps for a total of ~ 15000 micro strip detectors and 10 million electronic channels). Their high spatial precision and time resolution combined with adequate radiation hardness make them ideal for the intermediate tracking region (22 to 60 cm from the interaction point). The double-sided modules result by combining two detectors back-to-back with the strips rotated by 100 mrad. The typical strip length is 12.5 cm, and the pitch ranges from 61 to $122\ \mu\text{m}$ and from

81 to 244 μm for the primary and stereo views, respectively. The stereo geometry is used to measure radial coordinates in the forward region. The hit resolution is around 15 μm for the 61 μm pitch, and approaches the digital limit (pitch/ $\sqrt{12}$) for the larger pitches, where most of the charge is deposited on a single strip. A three-dimensional representation of the silicon tracker system (pixel and strips) is shown in Figure 2.3.

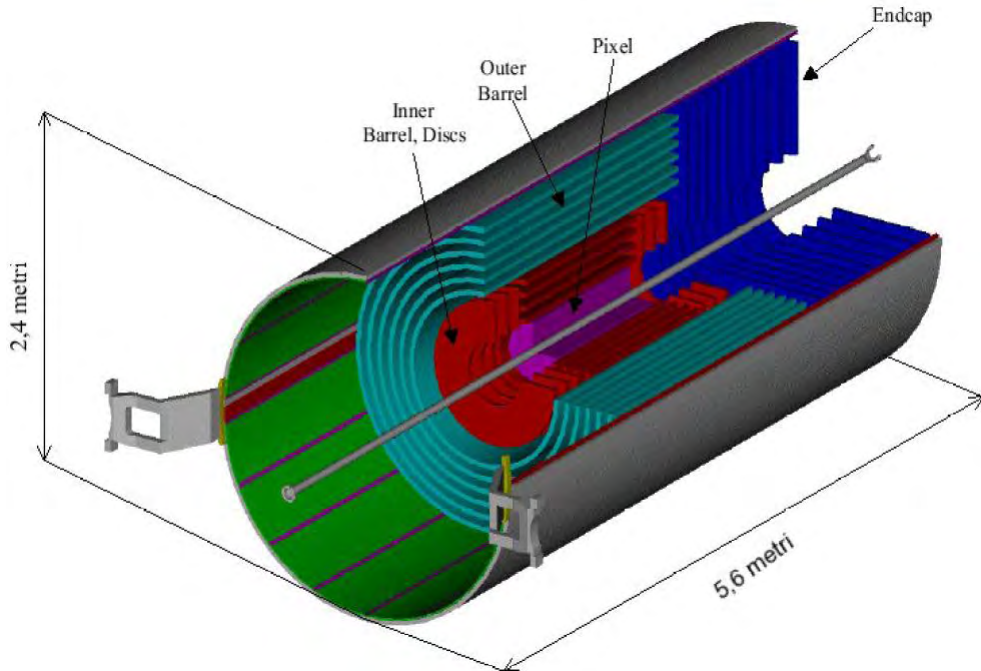


Figure 2.3: Overall layout of the CMS tracker

2.3 The Electromagnetic Calorimeter

The Higgs decay mode $H \rightarrow \gamma\gamma$, with its distinct signature was chosen as the benchmark for the CMS electromagnetic calorimeter (ECAL) [28]. A high-resolution, high-granularity lead tungstate ($PbWO_4$) crystal calorimeter has been chosen. The ECAL will count approximately 8000 $PbWO_4$ crystals with a radiation length¹, X_0 , of 0.9 cm and a Molière radius² of 21.9 mm. These values make it possible to construct a very compact calorimeter

¹The radiation length, X_0 , of a material is the thickness of that material where pair production happens with a probability of $P_{pair} = 1 - e^{-7/9} \approx 54\%$ for high energy photons.

²A characteristic constant of a material describing its electromagnetic interaction properties, and related to the radiation length by

$$R_M = 21\text{MeV} \times X_0/E_c$$

with fast signal formation and propagation and high radiation tolerance. In addition, the small Molière radius reduces the effect of pileup contributions to the energy measurement by reducing the area over which the energy is summed. The length of the crystals is 230 mm in the barrel and 220 mm in the endcaps, corresponding to 25.8 and 24.7 radiation lengths respectively. The crystals are all trapezoidal, with a square front face of $22 \times 22\text{mm}^2$ in the barrel and $30 \times 30\text{mm}^2$ in the endcaps, matching the Molière radius. Scintillator light is collected by silicon avalanche photo-diodes (APDs) in the case of barrel crystals, and vacuum photo-triodes (VPTs) for endcap crystals.

The energy resolution for the barrel and endcap calorimeter is:

$$\begin{aligned}\frac{\sigma}{E} &= \frac{2.7\%}{\sqrt{E}} \oplus \frac{0.210}{E} \oplus 0.55\% \\ \frac{\sigma}{E} &= \frac{5.7\%}{\sqrt{E}} \oplus \frac{0.245}{E} \oplus 0.55\%. \end{aligned}\quad (2.1)$$

The sum must be conducted in quadrature. The different terms depend respectively on the number of elementary processes and photo-statistic fluctuations, on the noise from the electronics and pile-up, and on to the calibration of the calorimeter. An internal view of the CMS ECAL is given in Figure 2.4.

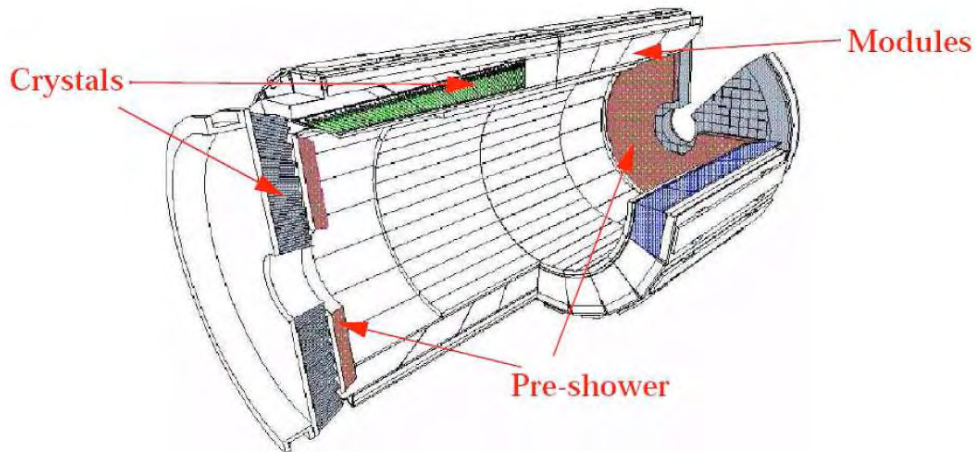


Figure 2.4: Internal view of the CMS electromagnetic calorimeter.

with X_0 the radiation length and E_c the critical energy. R_M is a good scaling variable in describing the transverse dimension of electromagnetic showers which is of the order of 2 - 3 R_M .

2.4 The Hadronic Calorimeter

The hadron calorimeter (HCAL) [29] is used to measure the direction and energy of jets, the total transverse energy and the transverse missing energy. High hermeticity is insured by a very forward calorimeter outside the magnet return yoke, with a total coverage of $|\eta| < 5.3$. The barrel and endcap HCAL, installed inside the magnet, cover the region $|\eta| < 3.0$.

The barrel and endcap calorimeters are sampling hadron calorimeters, with plastic scintillators as active elements interleaved with brass absorber plates and read out by wavelength-shifting fibres. Brass has been chosen since it has a reasonably short interaction length (~ 15 cm), it is easy to machine and it is non-magnetic. In both regions the read-out is done in towers with a size of $\Delta\eta \times \Delta\phi = 0.087 \times 0.087$. In the barrel the width is equal to 6.5 hadron interaction lengths (λ_I). Thus full shower containment is not possible within the magnet volume, and an additional “tail catcher” is needed. This addendum, placed outside the magnet, increases the width to $10\lambda_I$ in the $\eta < 1.74$ region. The very forward calorimeter, instead, is placed 11 m from the interaction point. The active elements are quartz fibres parallel to the beam, inserted in steel absorber plates. The different choice of material is justified by the different average radiation dose in this region.

The energy resolution is $\sigma/E \sim 65\%\sqrt{E} \oplus 5\%$ in the barrel; $\sigma/E \sim 85\%\sqrt{E} \oplus 5\%$ in the endcaps and $\sigma/E \sim 100\%\sqrt{E} \oplus 5\%$ (E in GeV) in the very forward calorimeter.

2.5 The Muon System

A “gold plated” signal for Higgs detection is its decay in $Z - Z^{(*)} \rightarrow 4$ charged leptons. If the leptons are muons, the best 4-particle mass resolution can be achieved without adding that muons suffer less radiative energy losses in tracker material. The four-lepton channel is essential in the search of both the SM and MSSM Higgs bosons. In addition, top events will be triggered through muon ($t \rightarrow W \rightarrow \mu$) and selected with b -jets tagged again with muons in jets. Furthermore, B-physics depends crucially on μ tagging. For all said, the effort put in construction of the CMS muon system [30] should not surprise.

The muon system must fulfill the job of: muon identification, muon trigger (see Section 2.8), and muon momentum measurement. The standalone momentum resolution is from 8 to 15% $\delta p_t/p_t$ at 10 GeV and 20 to 40% at 1 TeV. But, once the information from the central tracker is added the global momentum resolution is as good as 1.0 to 1.5% at 10 GeV and from 6 to 7% at 1 TeV.

The muon system, shown schematically in Figure 2.5, is located in the

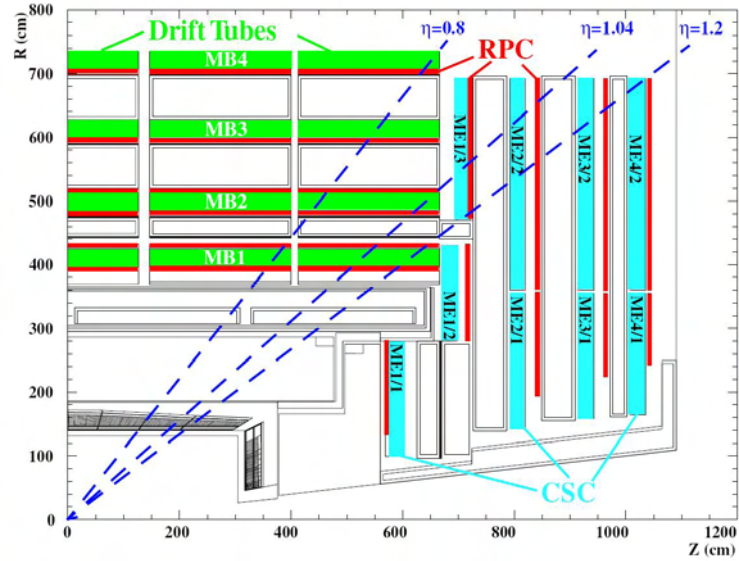


Figure 2.5: Longitudinal view of one quarter of the muon system.

iron return yoke of the magnet, which shields the detectors from charged particles other than muons. The magnetic field inside (1.8 T) the yoke plates bends the tracks and allows the measurement of their transverse momentum. The muon system is made up of three independent subsystems. In the barrel, where the track occupancy and the residual magnetic field are low, drift tube detectors (DT) are installed. In the endcaps, cathode strip chambers (CSC) are used, since detectors in this region have to cope with high particle rates and large residual magnetic field between the plates of the yoke. DTs and CSC cover the region $\eta < 2.4$. Trigger redundancy is assured by resistive plate chamber (RPC) in both sections of the detector. RPCs cover the region $\eta < 2.1$.

2.5.1 The Drift Tubes

Since in the barrel the occupancy is low and the magnetic field is well contained in the iron plates of the yoke, the detector working conditions are not so demanding. For this reason, drift tubes were chosen. The chamber segmentation follows that of the iron plates of the barrel yoke; five wheels along the z -axis, each one divided in 12 sectors in ϕ . Chambers are arranged in four stations with cylindrical geometry. The four layers are named MB1 through MB4, as shown in Figure 2.5. Each station consists of 12 chambers, except for MB4 where 14 chambers are present. Each chamber is made two times four staggered layers (a super-layer) of chambers measuring the $r - \phi$ coordinates, with the wires parallel to the beam line, and an orthogonal

super-layer measuring the $r - z$ coordinates. The latter is not present in the outermost station. The drift tube cells, whose section is shown in Figure 2.6, have a size of 42×13 mm. Each layer is obtained by two parallel aluminum

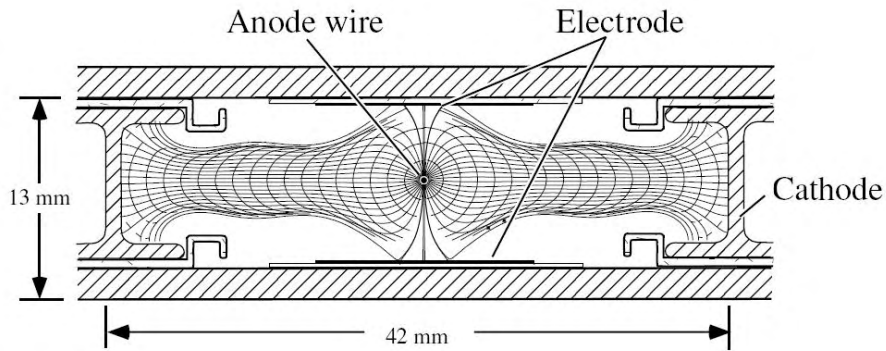


Figure 2.6: Schematic illustration of the section of a drift tube cell.

planes and by “I” shaped aluminum beams which define the boundary of the cells and serve as cathodes. I-beams are insulated from the planes by a 0.5 mm thick plastic profile. The anode is a $50 \mu\text{m}$ stainless steel wire placed in the center of the cell. The distance of the track from the wire is measured by the drift time of electrons; to improve the distance-time linearity, additional field shaping is obtained with two positively-biased insulated strips, glued on the the planes in correspondence to the wire. Typical voltages are +3600 V, +1800 V and -1200 V for wires, strips and cathodes, respectively. The gas is a 85/15% mixture of Ar/CO₂, which provides good quenching properties and a saturated drift velocity, of about $5.6 \text{ cm}/\mu\text{s}$. The maximum drift time is therefore $\sim 375 \text{ ns}$, i.e. 15 bunch crossings. A single cell has an efficiency of about 99.8% and a resolution of $\sim 180 \mu\text{m}$.

2.5.2 The Cathode Strip Chambers

Cathode strip chambers are multi-wire proportional chambers with good spatial and time resolution. They can operate at high occupancy levels and in the presence of a large inhomogeneous magnetic field. There are 468 CSCs in the 2 endcaps, organized in 4 disks divided in concentrical rings: three on the inner disks (ME1, closest to interaction point) and two on the outer, ME2...ME4. Each CSC is trapezoidal in shape and consists of 6 gas gaps, having a plane of radial cathode strips, which measure the coordinate ϕ , and a plane of anode wires running almost perpendicularly to the strips, which measure r . The spatial resolution is respectively $\sim 50 \mu\text{m}$ and $\sim 0.5 \text{ cm}$. The rings are formed by 18 or 36 trapezoidal chambers, which overlap in ϕ , with the exception of the outermost ring. The gap is 9.5 mm

thick and the gas used is a 30/50/20% volume mixture of Ar/CO₂/CF₄. The electron avalanche produced in the gap by a crossing charged particle induces a charge in a group of adjacent strips. The signal is interpolated to determine the center of mass of the charge distribution. The first disk, ME1, has to operate in difficult conditions, as it is exposed to a high magnetic field and particle rate. A slightly different design is adopted for chambers in this disk, with wires tilted by 25° to compensate for the Lorentz drift in the magnetic field. The gap is reduced to 6 mm and the number of strips is doubled above $\eta = 2.0$.

2.5.3 Resistive Plate Chambers

The RPC system is complementary to the DT and CSC systems, and adds robustness and redundancy to the muon trigger. Resistive plate chambers provide limited spatial resolution, but excellent time resolution, of the order of few nanoseconds or less. In the barrel, RPC chambers follow the segmentation of DT chambers. A total of six layers of RPCs are present; the first four are attached to each side of the MB1 and MB2 DT chambers. The other two are attached to MB3 and MB4. In the endcaps, chambers are trapezoidal; four layers are present for each forward region. The resistive plate chambers used in CMS are composed of four bakelite planes (treated with linseed oil) forming two coupled gaps, as shown in Fig. 2.7. The gaps are filled with a mixture of C₂H₂F₄ (freon), *i*-C₄H₁₀ (isobutane), and SF₆. The planes are externally coated by graphite electrodes, the two innermost ones set to +9.5 kV. Insulated aluminium strips are placed in the middle, to collect the signal induced by crossing particles. This two-gap design is adopted to add redundancy and increase the charge induced on the strips. In the barrel, the strips are parallel to the beam line, with a length of 80 or 120 cm. In the endcap, strips are radial with a length of 25 to 80 cm. The coordinate orthogonal to the strips is estimated as the center of a cluster of fired adjacent strips. No measurement is available in the second coordinate, apart from the constraint coming from the strip length. To increase rate capability, RPCs will operate in avalanche mode rather than in the more common streamer mode. However, the gas multiplication is reduced, and improved electronic amplification is required.

All this information is repeated and more is added in the following two sections, dedicated entirely to RPCs.

2.6 The RPC Detectors: a closer look

Resistive Plate Chambers are relatively young gas detectors. They were first developed in the early 80's [32] and, since then, have been used in many major experiments. Their low cost makes them the natural substitute

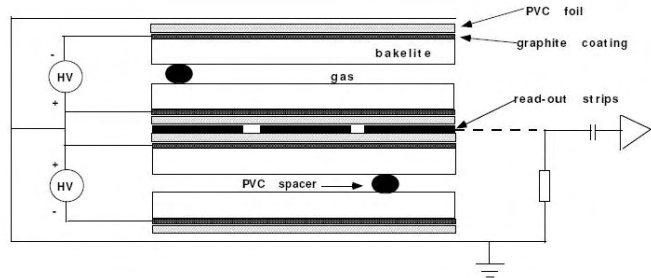


Figure 2.7: Schematic illustration of the section of a resistive plate chamber.

for scintillators in all those experiments in which large detection areas are needed. The detection rate capability strongly depends on their mode of operation as will be explained later. Schematically (figure 2.8), RPCs are made by two plastic resistive electrodes with a conductive coating, like graphite. The gap between the electrodes is kept constant by small plastic separators. The gap is filled by a gas mixture, that usually contains an organic gas with high UV absorption capability. A voltage difference is placed across the electrode. When an ionizing particle crosses the active volume, the free charges are accelerated by the external field and start an avalanche. The signal pick-up is realized by aluminum or copper strips laying on top of the graphite coating and insulated with a mylar foil.

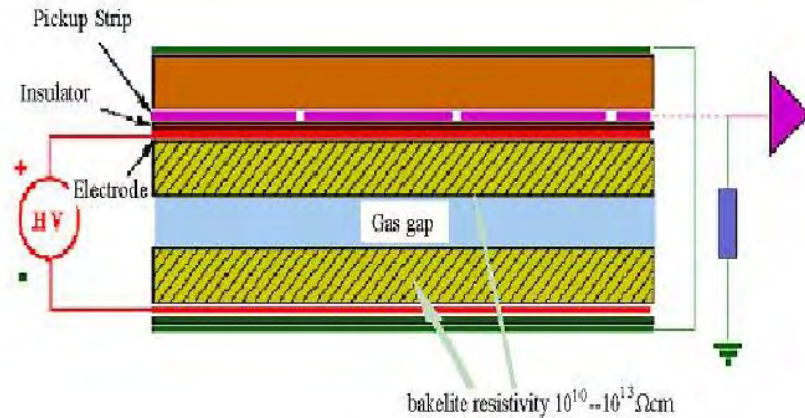


Figure 2.8: Schema of a resistive plate chamber.

The use of plane electrodes versus wire-like ones improves chamber time resolution on the chamber. The amplification region is extended to the whole gas gap. Thus the uncertainty due to the electron drift is significantly reduced. It has to be stress that RPCs use resistive electrodes. The main advantage is that the voltage drop across the bakelite electrodes is limited to a small region, so increasing the detector rate capability.

The operational principles of RPCs are reviewed in the following paragraphs.

2.6.1 Avalanche Formation in Gaseous Detectors

When a relativistic particle goes through matter, in particular a gas, it loses energy by interacting with the medium's molecules. This energy loss is regulated by the well known Bethe-Bloch [33] formula:

$$-\frac{dE}{dx} = \frac{4\pi N_A}{m_e c^2} \rho \frac{Z z^2}{A \beta^2} \left[\ln\left(\frac{2m_e \gamma^2 c^2 \beta^2}{\bar{I}}\right) - \beta^2 - \frac{\delta}{2} - \frac{C}{Z} \right], \quad (2.2)$$

where

- N_A is the number of Avogadro and m_e is the electron's mass;
- ρ, Z, A are the density, the atomic number and mass of the medium respectively;
- z is the charge and βc is the velocity of the incident particle;
- \bar{I} is the ionization potential of the medium. Its value is determined experimentally;
- the term $-\delta/2$ takes in account polarization effects in the medium;
- while $-C/Z$ accounts for the inner electrons screening effect.

The energy lost by the incident particle produces excitation and ionization of the medium. A relativistic particle produces an average of 100 electron-ion pairs in 1 cm of gas at normal conditions, too few for an useful electrical signal [34]. Instead, if an external electrical field is applied, the liberated charges are accelerated and may produce secondary ionization, hence multiplying the free charge. The presence of the electric field \mathbf{E} transmits an overall motion to the free charges, that move along the field's direction with a drift velocity $v_d = \mu \mathbf{E}/p$. p is the gas pressure and μ is a coefficient called *mobility*. Electrons have ~ 100 times higher mobility than ions.

When the external field is large enough ($\sim \text{kV/cm}$) a significant number of primary electrons³, accelerated towards the anode, gains enough energy to produce secondary ionization, so starting an avalanche. The velocity of positive ions is about 100 time smaller than that of electrons. This gives a drop-like shape to the charge distribution. Figure 2.9 is a schematic illustration of an avalanche profile. The avalanche continues to grow until the field due to the spacial charge, \mathbf{E}_s , is comparable with the external field. At this point, ion-electron recombination probability increases, with subsequent photon production. These photons start secondary avalanches, mainly along the axis of the primary one where the field is stronger ($\mathbf{E}_{total} = \mathbf{E} + \mathbf{E}_s$). The avalanche degenerates into a streamer, a plasma of ions and electrons, that eventually connects the electrodes producing a visible spark.

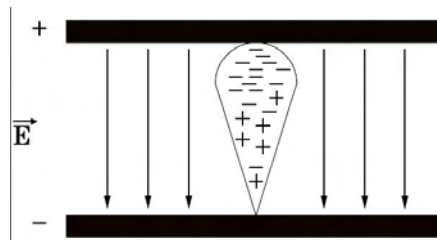


Figure 2.9: Schematic illustration of an avalanche formation in a gaseous detector.

The functioning of the detector is characterized by the amount of produced charged. Figure 2.10 shows the amplification factor⁴ as a function of the applied voltage. Five regions can be isolated:

- I- The primary electron-ion pair recombine before having the time to produce secondary ionization.
- II- The entire ionization charge is collected on the electrodes. The amplification factor remains constant even if the voltage is increased.
- III- The charge produced in the avalanche is proportional to the primary ionization and the collected charge increases strongly with applied voltage.
- IV- This is a region at limited proportionality.
- V- Once the amplification factor exceeds 10^8 the avalanche degenerates in a streamer. This is the functioning zone of Geiger-Muller counters.

³The primary charge is the charge liberated by the ionizing particle.

⁴The amplification factor is the ratio between the total charge produced in the avalanche and the primary ionization charge.

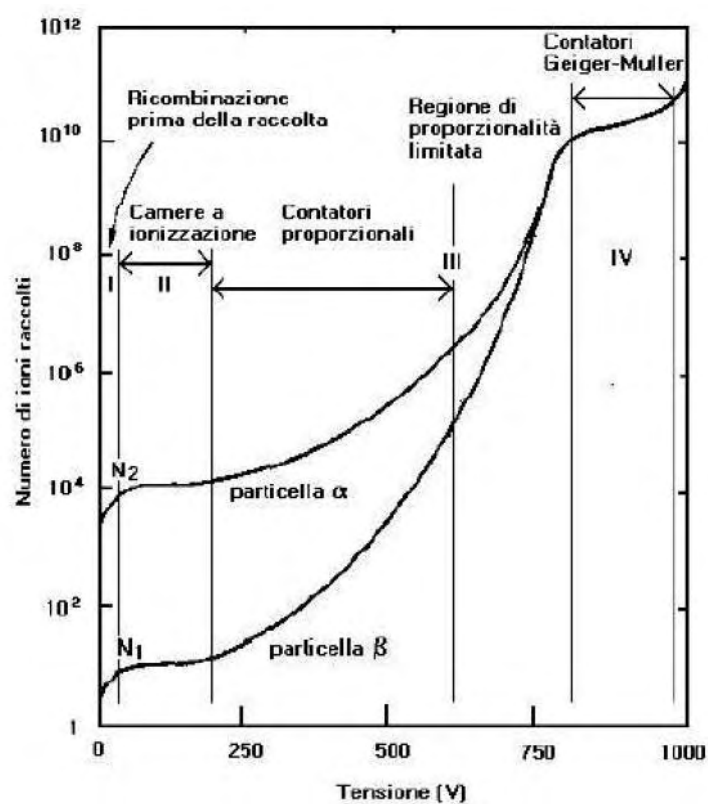


Figure 2.10: Amplification factor versus high voltage [35].

At higher voltages, discharges appear even in absence of ionizing particles. This may damage the detector and must be avoided.

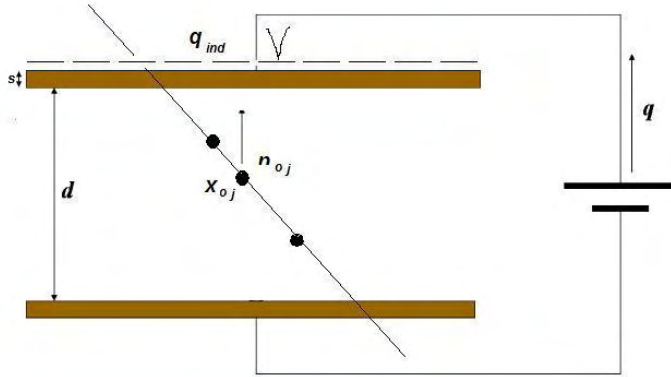


Figure 2.11: Schema of charge formation in a planar resistive gas detector.

Let us consider the passage of an ionizing particle in a gas detector with planar geometry (sketched in figure 2.11) and let us suppose it produces n_{0j} ion-electron pairs, i.e. a cluster, in the position x_{0j} . The average behavior of the avalanche growth in the gas mixture is ruled by the first Townsend coefficient α defined by the average number of ionizations per unit length, i.e the inverse of the free mean path, and by the attachment coefficient β , i.e. the average number of electrons captured per unit length, if an electronegative gas is used. α has many approximated analytic expressions, one of which is due to Korff [36]:

$$\alpha = pAe^{\left(\frac{Bp}{E}\right)} \quad (2.3)$$

where A and B are two constants and p is the pressure. Denoting $\eta = \alpha - \beta$ as the effective ionizing coefficient, the average electronic, negative and positive ion charges developed in the interval dx can be written respectively as [37]:

$$dn_{ej} = n_{ej}\eta dx \quad (2.4)$$

Integrating these equations in the interval $[x, x_{0j}]$, one obtains the total number of electrons produced and the total developed charge:

$$n_{ej} = n_{0j}e^{\eta(x-x_{0j})} \Rightarrow q_{ej} = q_{ele}n_{0j}e^{\eta(x-x_{0j})}, \quad (2.5)$$

where q_{ele} stands for the electrons charge. η is regarded constant for a uniform electric field. The factor $M = e^{\eta(x-x_{0j})}$ is the gas gain. When M exceeds the phenomenological limit of $\sim 5 \times 10^8$ ($\eta x \sim 20$), known as the Raether condition, the streamer is set on. For an RPC operated in avalanche mode and with gap width d the average charge for a single avalanche can be evaluated as:

$$\langle q_{ej} \rangle = q_{ele} n_{0j} \frac{\lambda}{\eta - \lambda} e^{\eta d} \quad \text{with } \eta d < 20, \quad (2.6)$$

where λ is the primary cluster density of the gas mixture.

Equations 2.5 can be easily extended to the total number N of clusters formed, but we must also consider possible fluctuation in the number of electrons in each cluster, in the number of initial clusters, and in the number of electrons produced in the multiplication process. Taking all this in account, one can write the total charge due to the electrons as [38]:

$$q_e(x) = \sum_{j=0}^N q_{ele} n_{0j} F_j e^{\eta(x-x_{0j})}. \quad (2.7)$$

The factors F_j hold the information on the gas gain fluctuations.

2.6.2 Signal Formation in RPCs

In RPC detectors, the drift of the produced charge towards the electrodes induces on the pick-up strips the fast charge q_{ind} , which is the useful detector signal. It must be noted that, while in wire gas detectors the signal is due to the ions, in RPCs it is due to the electrons, or at least its fast component is. Since the electrodes are resistive the charge is not dispersed or the whole plate. Only a limited section of the detector is interested by the discharge and temporarily inactive. It is, therefore, convenient to describe the chamber as an array of independent cells whose electrical equivalent is shown in Figure 2.12 a. The capacitors C and the resistance R are those of the bakelite electrodes, while C_g e R_g refer to the portion of gap interested by the discharge. After the passage of a ionizing particle the current I_g discharges the capacitor C_g and all the voltage difference is moved on the electrode equivalent capacitance. The external field is momentarily switched off. The time needed for the cell to return active and ready for the passage of another particle is:

$$\tau = R(C + C_g) = \rho \varepsilon_0 \left(\varepsilon_r + 2 \frac{s}{d} \right), \quad (2.8)$$

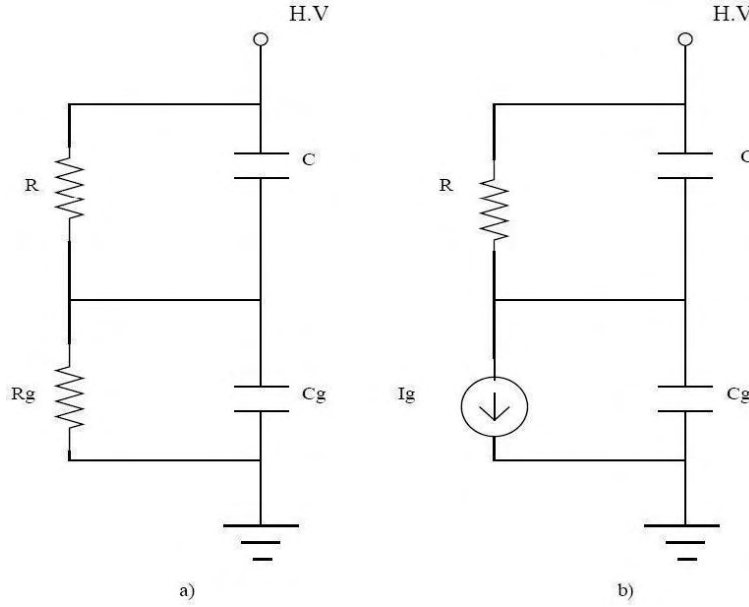


Figure 2.12: Electronic equivalent of an RPC cell.

where s is the gap width and ε_r , s and ρ are respectively the dielectric constant, the width, and the resistivity of the bakelite plates.

If we assume $\varepsilon_r = 5$ and a resistivity of $5 \times 10^{10} \Omega\text{cm}$, τ is ~ 31 ms. This is a much bigger value compared to the duration of the discharge (few nanoseconds). So the electrodes act as isolators and the avalanche growth is interrupted.

We can safely outline a RPC as an array of independent cells, placed parallel to each other. The area, S , of this elementary unit can be estimated by the formula:

$$S = Qs/\varepsilon_0 V = Cs/\varepsilon_0. \quad (2.9)$$

where Q is the collected charge and V is the operating voltage. The avalanche mode, as already stated is best indicated in high flux experiments. The streamer mode, instead, does not require powerful amplification electronics.

The current produced in the gap induces a proportional current on the pick-up electrodes. This induced charge in an RPC with gap width d is given by:

$$i_{ind}(d) = -v_d q_{ele} \frac{k}{d} \sum_{j=0}^N n_{0j} F_j \left[e^{\eta(d-x_{0j})} - 1 \right]. \quad (2.10)$$

The factor k takes in account material composition and geometrical factors.

2.6.3 Specific conditions and requirements for CMS RPCs

The RPC detectors in the CMS experiment are asked a time resolution of a few nanoseconds, to identify muons within a 25ns window [39]. The cluster size should be at most 2 in order to reach the required momentum resolution and minimize the number of possible ghost-hits. Finally, the efficiency should be $\geq 95\%$ up to hit rates of 1 kHz/cm^2 . The hit rate associated with the neutron and gamma background is 20 Hz/cm^2 in the barrel region and 250 Hz/cm^2 in the forward region at $\eta = 2.1$. To assure this rate capability the streamer contamination must as low as possible.

In the following, some simulated and experimental results will be given to justify the structural choices in the detector construction. The charge and signal formation model, illustrated in the preceding chapter, is in good agreement with real data [40].

RPC performances as a function of environmental parameters

The electrode resistivity mainly determines the rate capability. The electrodes are made of bakelite covered by a thin layer of melamine. The electrodes' bulk resistivity ρ [41] influences the RPC recovery time $\tau \propto \rho$ and the voltage drop V_d across them. At high rates, the flow of total current through the plates becomes important. The voltage drop can be estimated as:

$$V_d = 2 \langle q_e \rangle r s \rho, \quad (2.11)$$

where r is the rate/ cm^2 and s is the electrode thickness. Assuming $\langle q_e \rangle = 25 \text{ pC}$ and $r = 10^3/\text{cm}^2$, a value of $\rho \sim 10^{10} \Omega \text{cm}$ should be used to limit V_d to few tens of volts. A larger voltage drop would reduce the rate capability and influence the pulse delay due to the change of drift velocity.

The effective voltage is dependent on the total current flowing through the RPC. Moreover, it depends also on environmental parameters as temperature and pressure. This effect can be attributed to the variation of the gas density with temperature [42]. At lower temperatures (or higher pressures) the gas has higher density so reducing the mean free path of the accelerated electrons in the avalanche. The Townsend coefficient results reduced. The working voltage of the RPC is so dependent on the temperature and pressure. To compare measurements taken in different conditions, the nominal voltage must be scaled according to the formula:

$$V_{gap} = V_{nominal} \frac{T}{P} \frac{P_0}{T_0}, \quad (2.12)$$

where P_0 and T_0 are the reference pressure and temperatures.

A systematic and precise monitoring of the environmental parameters is fundamental in order to follow the effective working voltage of the detector. The efficiency and the performances of the RPC are strongly dependent on the temperature and pressure. As an example a variation of 3 °C (or 10 mbar) shifts the working voltage of the RPC of about 100 V.

The effect of the temperature is also to change the electrode resistivity according to the following empirical law:

$$\rho(T) = \rho_{20} e^{(20-T)/7.8}, \quad (2.13)$$

where T is measured in °C, ρ_{20} is the resistivity at 20 °C, and 7.8 is a factor obtained experimentally [43]. When the temperature increases of 3 °C, the resistivity is reduced by 30% and the dark currents of the detector could increase in a dangerous way.

The operating temperature for the CMS RPCs is kept constant in the range 21 ÷ 24 °C by a cooling circuit on the chamber and on the iron yoke.

Monitoring of chamber temperature is fundamental in order to hold under control the correct performance of the detector.

Gas Mixture

In principle, for a given ηd , the gas cluster density λ should be as large as possible, to maximize the useful signal as it can be seen in equation 2.6. For small values of λ the chamber inefficiency increases. Figure 2.13 shows the simulated charge distribution for gaps of 3 mm and $\eta = 6 \text{ mm}^{-1}$ for different values λ . On the other hand, λ should not be chosen too big because this increases the streamer probability, therefore reducing the operating plateau⁵. The efficiency and streamer probability for a 2mm gap and $\eta = 6 \text{ mm}^{-1}$ are shown in Figure 2.14.

The gas mixture chosen for CMS RPCs is 96.2% $C_2H_2F_4$ (freon), 3.5% $i - C_4H_{10}$, and 0.3% SF_6 . For this variety of freon [46] $\lambda \sim 5$. It acts as a strong quencher on the discharge keeping the detector in avalanche mode. Isobutane is instead used the absorb photons and reduce the region interested by the discharge. Finally it can be proved that 0.3% of SF_6 increase the operating plateau of almost 200V [47].

Gap Width

The gap width influences the time resolution σ_t of the detector. The performance becomes poorer at wider gaps, as reported in Figure 2.15. The full width at base (FWAB), that is the time interval containing 95% of the events, is also given. A 2mm gap width seems the right choice. This places

⁵The operating plateau is defined as the range in the operating voltage where the chamber efficiency is > 90% and the streamer probability < 10%).

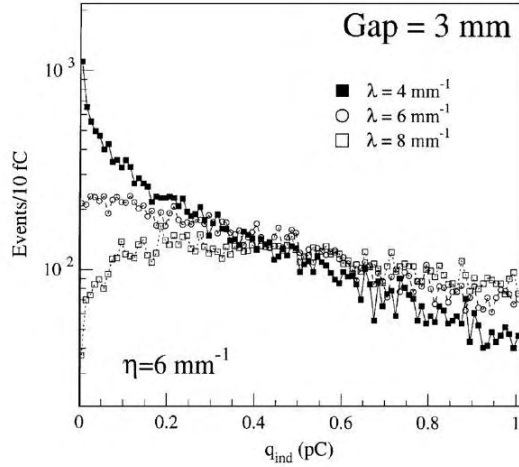


Figure 2.13: Induced charge spectrum with a gap of 3 mm and $\eta = 6 \text{ mm}^{-1}$ ad a function of λ [44].

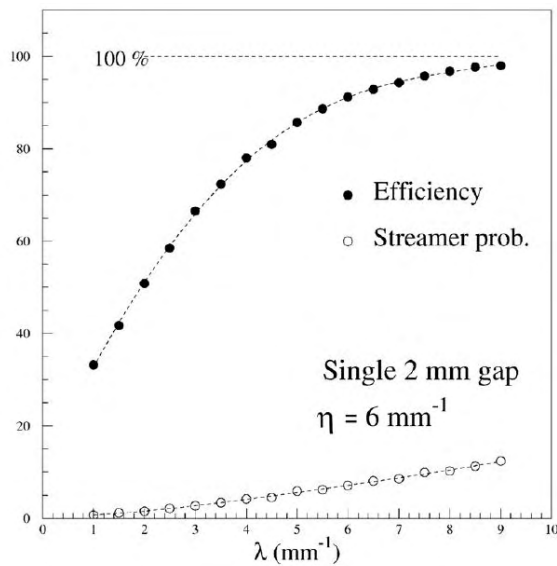


Figure 2.14: Efficiency and streamer probability for a 2mm gap and $\eta = 6 \text{ mm}^{-1}$ for different values of λ [45].

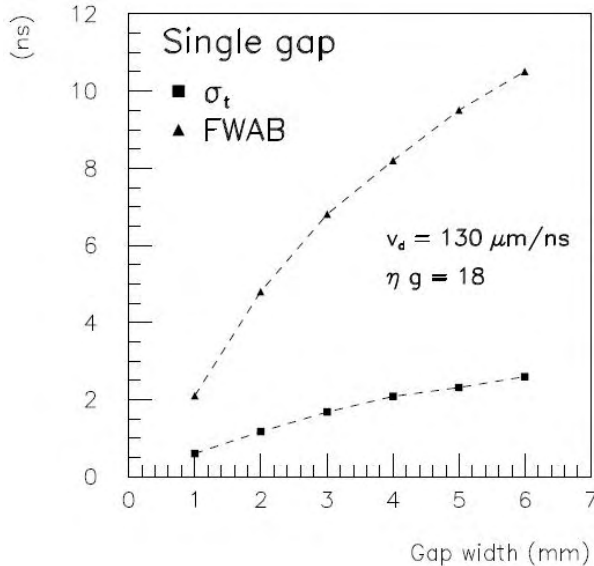


Figure 2.15: Simulated time resolution as a function of the gap width [30].

the operation voltage in the range 8.5-9.0 V or more (Figure 2.16). The gap thickness is maintained constant by a rigid external support structure and a network of isolating spacer. Better efficiencies at lower voltages could be obtained using wider gaps.

Double Gap

If more gaps are put together the signal on the read out strips increases; it is the sum of the single gap signals. This allows to operate each single gap at lower gas gain with an effective efficiency that is the OR of the single gap efficiencies.

The RPC proposed for CMS is made of two 2mm gaps with common pick-up strips in the middle (Figure 2.17a). When the signal extraction is difficult, two independent read out planes are located externally (Figure 2.17b). The signal are ORed before entering the font end boards. In both cases, the charge spectrum improves compared to the single gap detector. Figure 2.18 shows that higher thresholds can be used without loss of efficiency.

Also the time resolution is believed to improve, as it can be seen in Figure 2.19. A lower limit of 1.4 ns can be achieved; electronic noise and local field variation must be considered for the real experimental time resolution.

Noise Rate

In order to not generate fake triggers, the RPC should produce an electronic signal only when a particle crosses the detector. Unfortunately, as

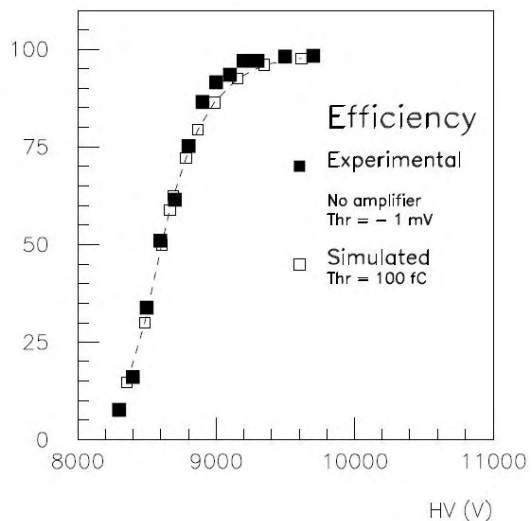


Figure 2.16: Simulated and experimental results for the efficiency of a 2mm gap RPC [30].

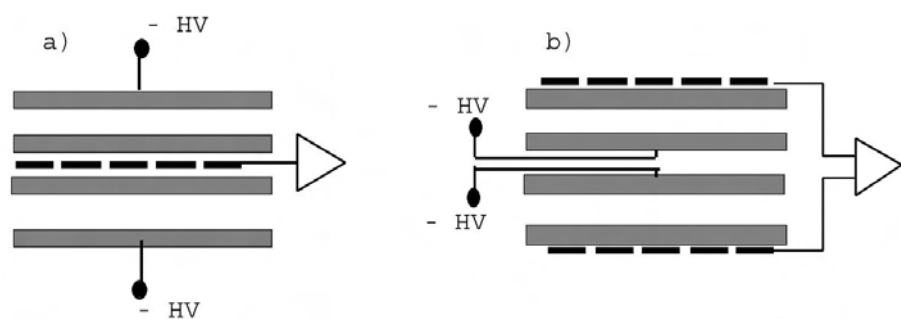


Figure 2.17: Simplified layout of the double gap RPCs.

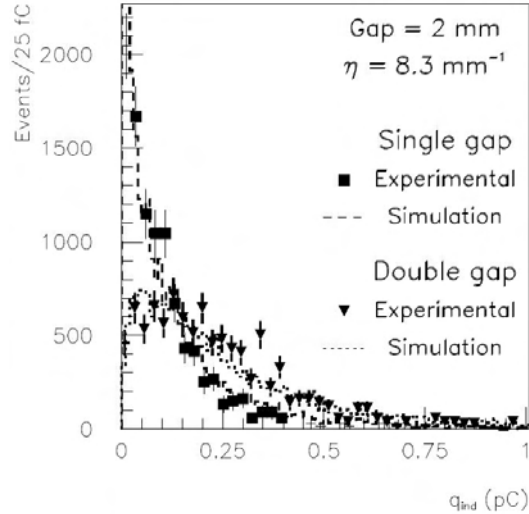


Figure 2.18: Simulated and experimental charge spectra for single and double gap RPCs [30].

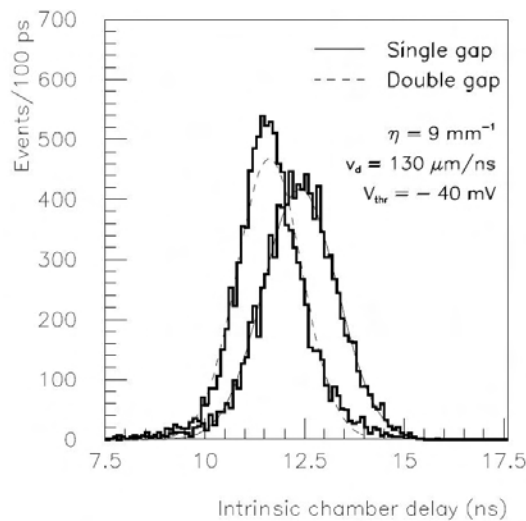


Figure 2.19: Simulated time distributions for single and double gap RPCs [30].

already discussed in previous section, the signal induced by an avalanche on a strip is only a fraction of pC. So in order to mention high detection efficiency, a very low threshold has to be set on the electronic boards. Thus, it is possible that induced noise and avalanche generated by thermal effects or electrode defects generate signals not related to real particles. The RPC trigger architecture in CMS allows a max signal rate of about 50 Hz/cm^2 . If this noise is bigger than this value, the fake trigger rate is too big.

As already described the background rate due to gammas and neutrons is expected to be about 20 Hz/cm^2 in the barrel region and is related to the machine. In order to not increase this rate, the RPC electrode surface has been treated with a film of linseed oil, to smoothen any possible imperfection. It has been proven that such treatment allows a noise rate below 2 Hz/cm^2 [50]. Moreover, careful studies on the ripple of high and low voltage systems ave been carried on in order to reduce the electronic noise induced on the strips. The results obtained during the MTCC, that will be described later, show that the noise rate is at the moment even lower than expected.

One of the main tasks of the detector control system (see section 3.6), is to monitor and store on database, for future analysis, this important parameter.

2.7 The RPC Detectors: preliminary results on chamber production

Each RPC chamber is extensively tested to ensure that it meets the requirements previously discussed. The gaps are tested for gas leaks and high voltage tolerance before assembly. The accepted double gaps are then sent to the assembling site where the chambers are built and pretested. Gas, cooling, high voltage and noise tests are performed. The chambers are also inspected for eventual popped spacers. The RPC collaboration has decided to characterize the chambers by chamber efficiency, noise rate, cluster size⁶ and dark current as a function of the high voltage working point. Tests have been conducted with cosmic rays telescopes and irradiation facilities in Italy, at different beam areas at CERN and at Gamma Irradiation Facility, always at CERN. In the following section, some results on RPC chamber performances are presented.

All 480 chamber foreseen for the barrel region have been assembled and tested with cosmic rays. One fourth of the chambers have been assembled at the *Hitech* industry in Caserta (Italy), under the supervision and responsibility of the Naples group. Test stations are present in Bari (Italy), Pavia (Italy), and Sofia (Bulgaria). Figures 2.20, 2.21, and 2.22 show the mean

⁶The cluster size is the number of contiguous fired strips in a same chamber.

cluster size, the current, and the max efficiency respectively for all tested chamber. These results have been presented at the IEEE conference in San Diego in November 2006.

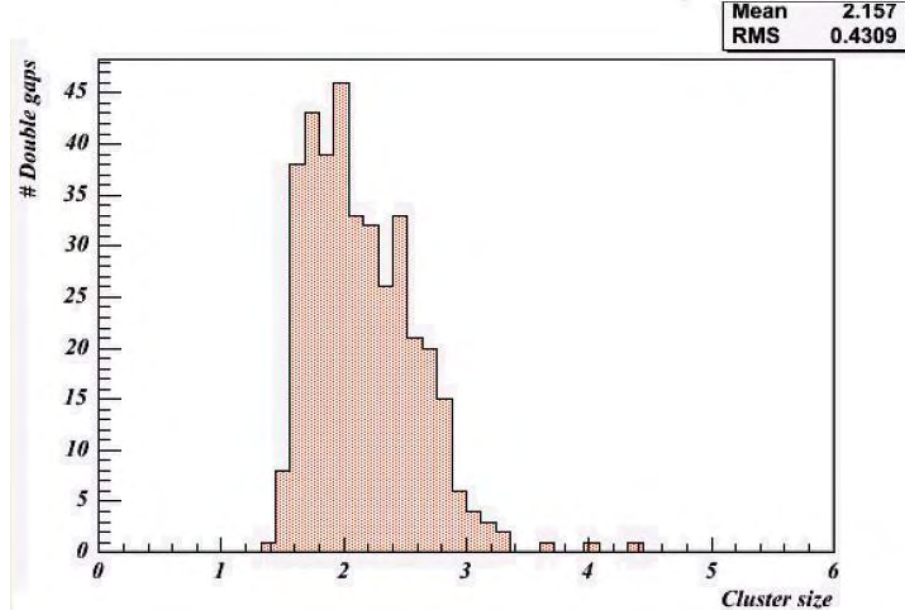


Figure 2.20: Mean cluster size distribution for the barrel RPC chambers [48].

The barrel production is on schedule and the results of the cosmic ray tests are very encouraging. The average efficiency is 97.3%, with an average current of $1.5 \mu\text{A}$. The obtained average cluster size of 2.2 strips ensures the required muon momentum resolution. The gas mixture fluxed in the chambers during the tests is composed by 96.2% $\text{C}_2\text{H}_2\text{F}_4$, 3.5% $i - \text{C}_4\text{H}_{10}$, and 0.3% SF_6 .

The CMS forward region counts 756 Resistive Plate Chambers in its complete configuration. Of these, only 432 will be present for the start of the experiment in 2007, the rest will be staged. The staged chambers are those on the discs $YE +/- 4$, that is the farthest from interaction point, and all chambers at $1.61 < |\eta| < 2.10$. Up to November 2006, 288 endcap RPCs have been assembled and tested and 46% have been installed. Figure 2.23 shows the efficiency of a RE1/2 type chamber. This kind of chamber will be installed on the first disc (closest to interaction point) in the $< \eta <$ region. The chamber was fluxed with a 96/3.7/0.3% $\text{C}_2\text{H}_2\text{F}_4/i - \text{C}_4\text{H}_{10}/SF_6$ gas mixture and exposed to muons at the X5A beam area at CERN.

Returning to figure 2.23, the upper curve (in green) corresponds to the double gap configuration, the lower curves are the efficiency curves for single

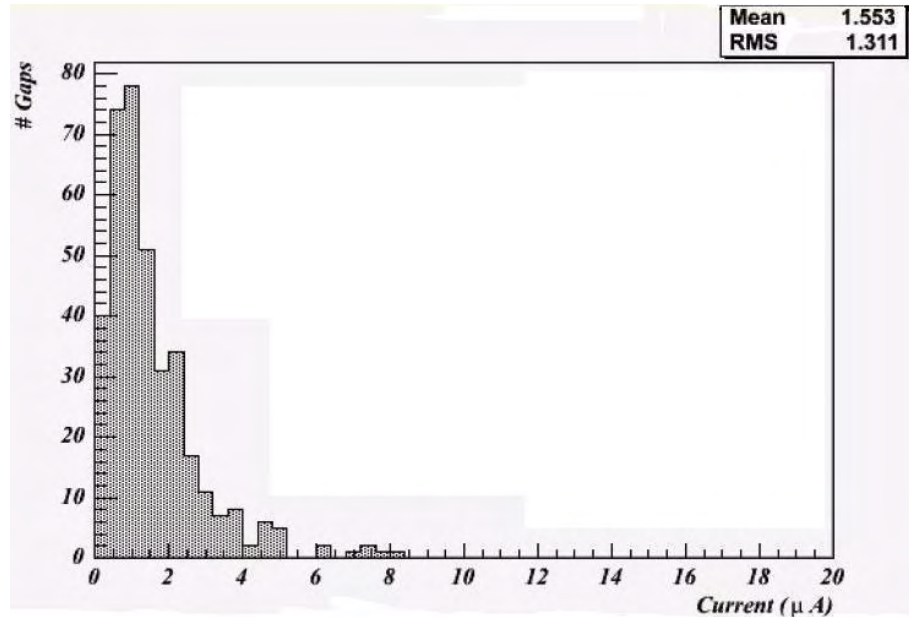


Figure 2.21: Current distribution for the barrel RPC chambers. The measurements were taken with a max efficiency of 95% [48].

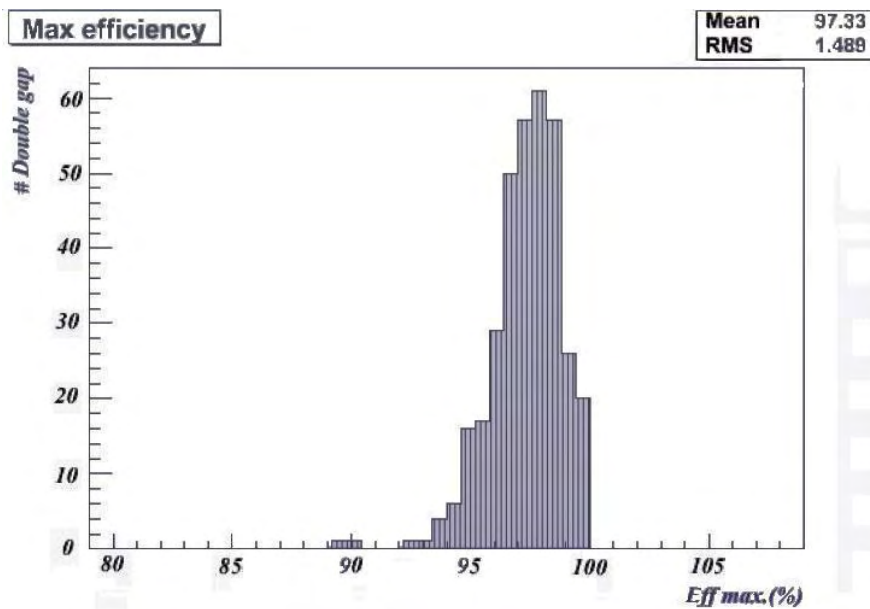


Figure 2.22: Mean cluster size distribution for the barrel RPC chambers [48].

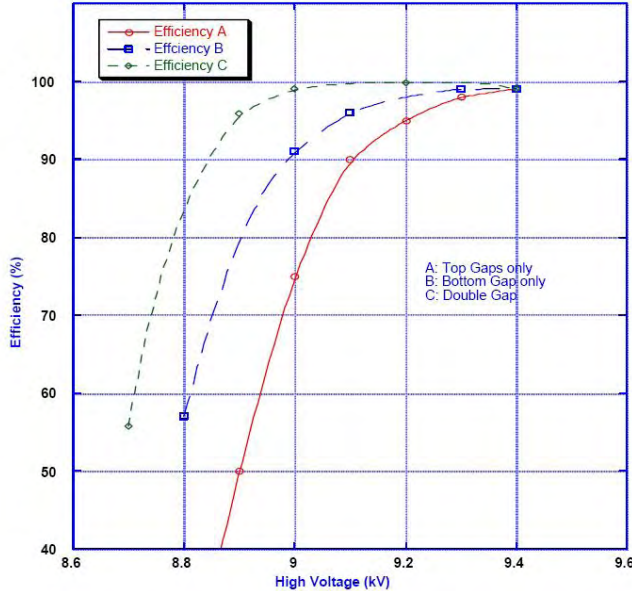


Figure 2.23: Efficiency curves for single (A, B) and double gap configuration [49].

gaps. It is seen that the double gap reaches the start of the plateau at a 9 kV setting. At this voltage, for the double gap configuration, the average cluster size is well below the value 2, as shown in figure 2.24 . Clearly, increasing the applied voltage, the cluster size becomes larger indicating the onset of an increasing streamer fraction. Figure 2.25, instead, shows the measured noise rate for nominal operating voltages of 9.0 kV. The dark current has been measured on a test beam in between spills, and it appeared to range from a fraction of micro amp to $3 \mu\text{A}$, depending on the high voltage setting [49]. Concluding, in terms of muon detection efficiency, noise rates, dark currents and cluster sizes, this first production RE1/2 follows all the requirements quite well.

2.8 The CMS Trigger

Event selection is a very complicate task for all LHC experiments. The bunch crossing frequency is 40 MHz and, at design luminosity of $10^{34} \text{cm}^{-2}\text{s}^{-2}$, the average number of events per beam collision is 17. This means an input rate of 10^9 interactions per second that produce approximately 1 MB of data. This must be reduced by a factor 10^5 since the maximum rate capability of the on-line computer farms is 100 Hz at a data flow of ~ 100 MB/s. CMS has chosen to accomplish this in two steps. Figure 2.26 shows the schema

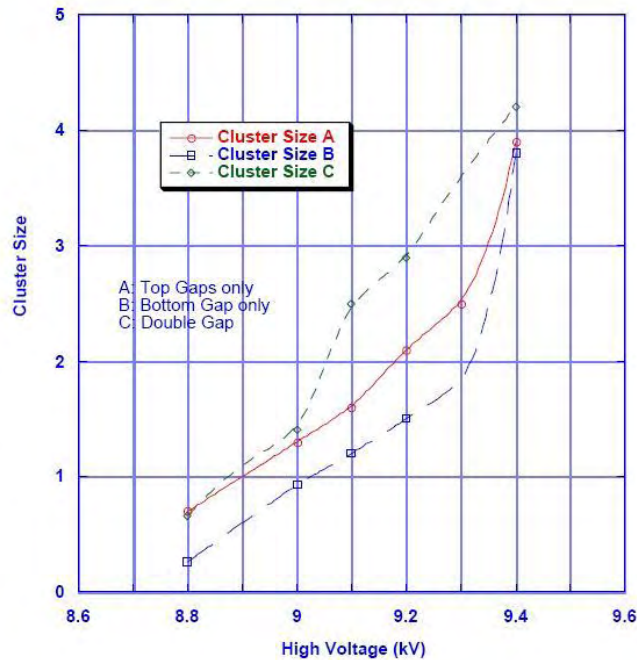


Figure 2.24: Cluster size for an RE1/2 chamber as a function of the operating high voltage [49].

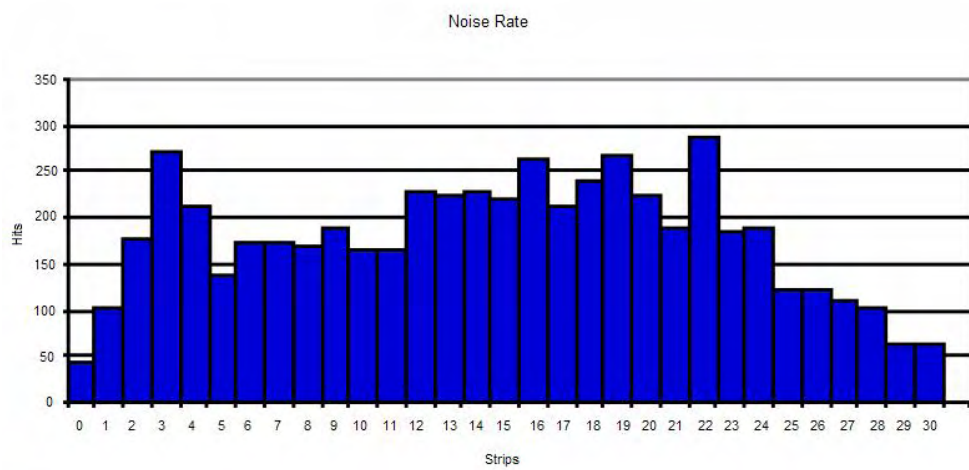


Figure 2.25: Noise rates for an RE1/2 chamber. The nominal voltage is 9.0 kV [49].

of the trigger data flow. At first, the level-1 trigger [51], based on custom electronics, reduces the rate to 75 kHz. Since no decision can be made in 25 ns, all the data is kept in pipelines before processing. While a decision is taken, all the detector information must be kept. The most stringent requirements come from the buffers used to store data from the tracker. The

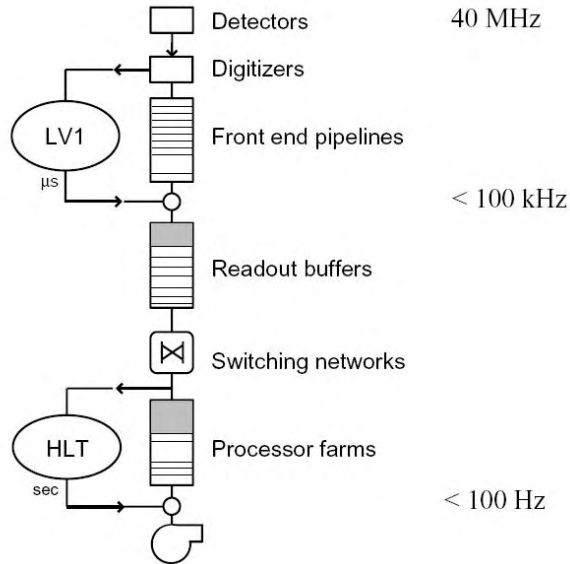


Figure 2.26: Data flow in the CMS Trigger system. Two consecutive processing stages are implemented: level-1 and High Level Triggers.

maximum time latency time is $3.2 \mu s$, corresponding to 128 bunch crossings. Level-1 trigger uses fast and low resolution data coming from calorimeters and muon system. The information coming from the level-1 Muon trigger is synchronized with that of the level-1 Calorimetric trigger by level-1 Global trigger. It performs a fast reconstruction of single-objects like muon tracks and hadronic and electromagnetic calorimeter clusters and measures their physical properties (P_t , E_t , etc.). Moreover, it performs reconstruction of global variables, like total transverse energy stored in the calorimeters, total missing energy E_{miss} and total number of electrons and muons. The level-1 output objects are called trigger primitives. The events are selected by applying thresholds on the trigger primitives. Trigger conditions based on event topology can also be applied, for example by searching only for particles back-to-back or jets opposite to a missing energy. It is the Global trigger which applies the threshold and checks the topological requirements.

In the second step, the selected events are forwarded to the High Level Trigger (HLT) [51]. The HLT uses commercial computer to run selection algorithms on the read-out data of the accepted events. The total processing

time is $\sim 1\text{s}$ per event, after which the accepted rate reaches the desired 100 Hz. In order to optimize data flow, event selections are made in progressive stages by applying a series of filters. The initial decision is made on a subset of data, from detector components such as calorimeter and muon systems (level-2). This avoids saturating system bandwidth by reading out the large volume of data from the Tracker detector. Final High Level Trigger algorithms are then applied to the complete event (level-3). Finally, selected events are sent to the CMS Data Acquisition System (DAQ) for mass storage.

Even if the system is optimized for $p - p$ running conditions, its performance will also be adequate for heavy ion collisions. Heavy ion collisions will occur every 125 ns, but will have a much higher multiplicity than pp interactions. Due to the high resulting data volume, the level-1 rate will be limited to about 5 kHz for central Pb-Pb collisions.

2.8.1 The Calorimetric Trigger

The calorimeter trigger identifies five types of objects: isolated electrons/photons, non-isolated electrons/photons, central jets, forward jets and τ -jets. The measurement of transverse energy and position of the four most energetic objects of each type is sent to the Global Trigger, together with a measurement of the total and missing transverse energy. In addition, the calorimeter trigger provides the Muon Trigger with information about the activity in all calorimeter regions, to determine if the energy deposit is compatible with the passage of a muon (Minimum Ionizing Particle bit) and if it is below a programmable threshold (Quiet bit). For trigger purposes, all calorimeter detectors (ECAL, HCAL) are topologically segmented in trigger towers with a size of $\Delta\phi \times \Delta\eta = 0.087 \times 0.087$ up to $\eta \sim 2$. At higher pseudorapidity values $\Delta\eta$ increases up to 0.35. Trigger towers match the granularity of HCAL up to $\eta > 1.74$; below that value, HCAL towers have twice the ϕ dimension of the trigger tower. In the barrel ECAL, each tower corresponds to 5×5 crystals, while the ECAL endcap crystals are arranged in a $x - y$ geometry, and a variable number of crystals is grouped, matching as much as possible the HCAL trigger tower boundaries. Towers are defined also in the very forward calorimeter, with a size of $\Delta\phi \times \Delta\eta = 0.348 \times 0.5$.

2.8.2 The Muon Trigger

The level-1 Muon Trigger of CMS [30] [51] uses three kinds of muon detectors: DT, CSC and RPC. DT and CSC have good spatial resolution for muon track position and momentum measurements. The RPCs, instead, have superior time resolution and are mainly dedicated to the trigger for providing unambiguous identification of the bunch crossing in which the muon originated. Six layers of RPCs are present in the barrel and four in each

endcap. RPCs will also give additional information for track reconstruction. In CMS both precise muon chambers and dedicated trigger detectors are used for triggering. Two independent muon trigger systems cover the CMS barrel region: one using DT chambers, the other using RPC chambers. Similarly in the endcaps, one trigger system uses CSC chambers, the other RPCs. At the first level the two muon triggers are completely independent. Thus they allow cross calibration. In particular during the first phases of the experiment, the RPC trigger, with its relative simplicity, will be used to calibrate the DT and CSC triggers.

The DT/CSC and RPC system have complementary characteristics. Therefore they respond differently to the same background. DTs and CSCs are vulnerable, much more than RPCs, to the radiation associated with muon at high p_t ($> 100\text{GeV}/c$). This radiation is made of electromagnetic showers produced by $e^+ - e^-$ pairs, bremsstrahlung or nuclear interactions. The effect is a poor local reconstruction, hence low efficiency. On the other hand, RPCs suffer from low energy backgrounds and intrinsic noise. Accidental multiple noise hits can be confused with a signal. This is much more rare in DTs and CSCs where the reconstruction are done through the coincidence of many layers in each station.

The basic tasks of the level-1 Muon Trigger are muon identification, P_t measurement and bunch crossing identification. The possible muon production channels in $p - p$ scattering are: decay of heavy object (W , Z , top, Higgs, etc.), decay of b quarks, decay of hadrons with u , d , and s quarks (primarily τ and K), and punch-through of hadronic jets. The muons from the first two channels, called prompt, are produced very close to the interaction vertex. Only the high transverse momentum muons can be detected and of signatures are interesting physics. The remaining low p_t muons, with cosmic muons and beam halo muons (machine background) represent background. The expected production frequencies of one and two-muon events are reported in Figure 2.27. Cuts on the muon p_t are a compromise between efficiency and level-1 trigger maximum rate.

The logical structure of the Muon Trigger is shown in Figure 2.28. DT and CSC electronics first process the information from each chamber in local trigger processors. As a result one vector, containing information on position and angle, per muon per chamber is delivered. Vectors from different chambers are collected by a “regional trigger”, the Track Finder (TF), which combines them to form a muon track and assigns a transverse momentum value. The four best (with the highest p_t and quality) muon candidates from each system are selected and sent to the Global Muon Trigger. For RPC there is no local processing. Hits from all stations are collected and analyzed by the PACT (Pattern Comparator Trigger) processors. The PACT looks for correlation in space and time between hits in the RPC stations. Hits are compared with pre-defined patterns. The comparing algorithm looks for spatial and time correlation between hits in 4 stations. The event is selected

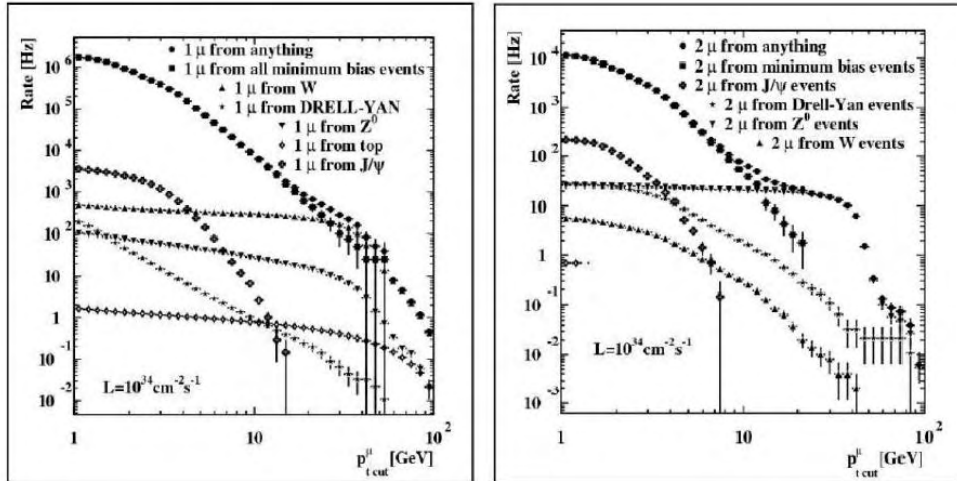


Figure 2.27: The expected production frequencies events with one and two-muon in the final state at design luminosity.

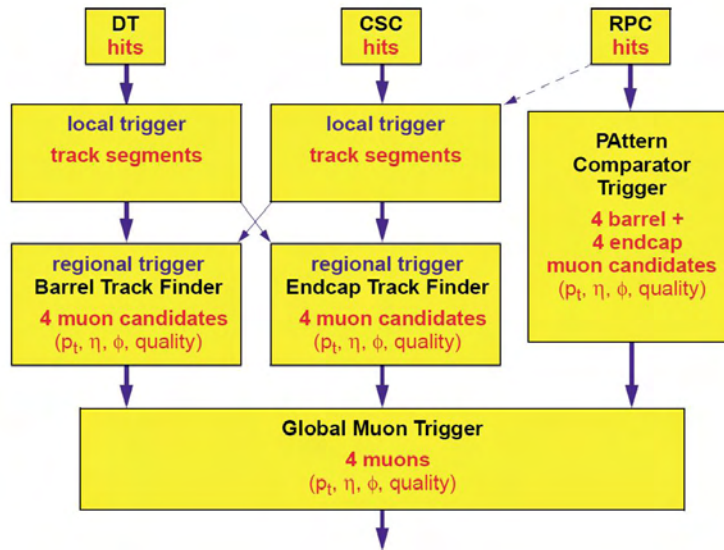


Figure 2.28: The Muon trigger data flow.

with at least three concurrences. A quality factor, along with p_t , η and ϕ values, is assigned to the muon and the information is sent to the Muon Sorter. The Muon Sorter selects the four highest p_t muons from the barrel and four from the endcaps and sends them to the Global Muon Trigger. The Global Muon Trigger compares the information from TF (DT/CSC) and PACT (RPC). Information delivered by the Calorimeter Trigger is used to form an isolated muon trigger. The overall four highest p_t muons are then transmitted to the Global Trigger. Finally transverse momentum thresholds are applied.

A few preliminary results for the RPC trigger will be presented in Chapter 4.

Chapter 3

Development of the RPC Control and Monitoring System in CMS

Only thirty years ago a single detection device, such as a bubble chamber, was sufficient to reconstruct the full event information. Nowadays, particle physics experimental apparatuses are always more complex and have reached massive dimensions. The increase in complexity of the experiments goes along side with the raise of the number of electronic channels and the sophistication of the external services necessary to run the detector. Given the description in chapter 2, we can state that this is also the case of the CMS detector.

CMS will produce an incredible amount of information at an unprecedent speed. An online system capable of managing the data flow, archive, and ensure the high data quality is fundamental. In CMS, this task is fulfilled by the Data Acquisition System (DAQ) and High Level Trigger. The later has been already discussed in section 2.8. All the functionalities of the DAQ are controlled by the Run Control and Monitoring System (RCMS). The RCMS is composed by both software and hardware components. It offers the user an interface to facilitate access, control and configuration of all subsystem during data taking.

The complexity of the CMS detector, the high number of subcomponents, and the peculiar working environment make it necessary to develop a control system parallel to the data acquisition system. The Detector Control System (DCS) is responsible for the correct operation of the CMS experiment. It includes all subsystems and other individual elements involved in the control and monitor of the detector, its active elements, the electronics on and off the detector, the experimental hall as well as communications with the accelerator. The DCS interoperates with the RCMS and DAQ through a distributed processing environment, called XDAQ, developed with the a

middleware approach (see section 3.1).

The main aspects of the DAQ system are discussed in section 3.1. Section 3.2 presents the RCMS and its principle functions. The remaining of the chapter is dedicated to the DCS; in particular to the DCS for the RPCs. In fact, this thesis is centered on the development of the RPC control and monitoring system in CMS and its integration in the general CMS DCS. A detailed description of the project and its functionalities are given in section 3.6.

3.1 Data Acquisition System in CMS

The CMS Trigger and Data Acquisition System (TriDAS) is designed to readout the detector information at bunch crossing frequency (40 MHz). How the total amount of data in CMS is reduced, by a factor of $\sim 10^5$ to the required storage capability of $\sim 10^2$ Hz at data rates of $\sim 10^2$ MB/s, has been already discussed in section 2.8. In the present section, instead, the main features of the data acquisition system (DAQ) [52] are documented .

The DAQ system is the first place where the entire information from each collision will be inspected. It will allow the fast transfer of large amounts of data, provide the resources for filtering such data, record the selected events, monitor the information, and last but not least, provide a functional user interface. Considering the number of detector elements to be readout, the amount of data, the event acceptance frequency of the level-1 trigger and computing power needed for event selection, the CMS DAQ yields unprecedented system requirements.

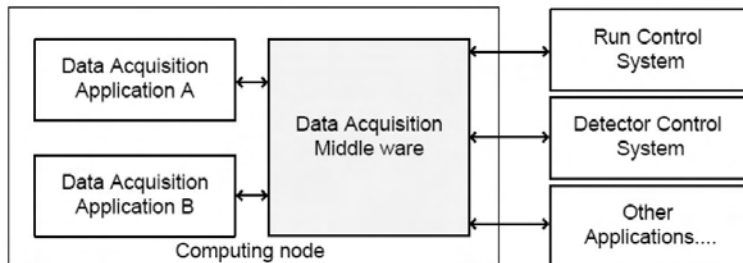


Figure 3.1: Online software schema on a computing node [52].

The complexity of the system developed imposes a distributed approach to the realization of the computing system and software infrastructure. This requires a set of services and application programming interfaces, called middleware. A middleware is a software layer that provides the different applications with an uniform mechanism to access hardware and system services. It permits all applications to communicate across networks, system and lan-

guage boundaries and perform the data acquisition tasks. The middleware also interacts with the services responsible for the configuration and control of the different detector parts. Figure 3.1 shows the online software schema on a computing node and its connections with external systems.

The DAQ architecture is shown in Figure 3.2. The *Detector Front-ends* are the modules which store the data from the front-end electronics after the level-1 trigger decision. These modules, approximately 700, are read in parallel and the data are stored in deep buffers. The *Readout System*, that performs this task, is composed of ~ 500 units referred to as Readout Columns. All data corresponding to a single event is collected from the buffers via a switch and assembled in a single data structure, a “physics event”. Subsequently, it is sent to the HLT farm by a large switching network, the *Builder Network*. The processors where the HLT algorithms are executed constitute the *Filter System*. The selected data are forwarded for mass storage and further analysis. The entire data flow is controlled by the *Event Manager*. Finally, the *Computing Service* includes the processors and networks necessary for the acquisition of the events accepted by the HLT and the interface to the offline environment.

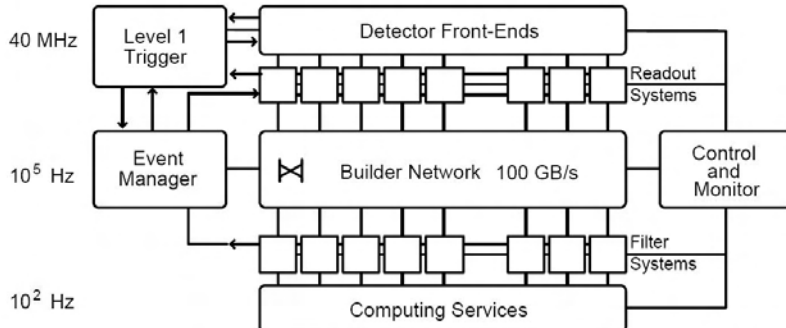


Figure 3.2: Architecture of the CMS DAQ system [52].

In addition, the DAQ operates the detector control and monitoring system. The quality of the physics data and the safe operation of the detector are guaranteed by a three level approach. First, monitoring and control of all the aspects of the front-end electronics is provided by the Front-end Controllers, FEC. The second level is constituted by the Detector Control System (DCS). The DCS is responsible for controlling and monitoring all the detector services and environmental variables. During data taking the DCS will operate under the supervision of the Run Control and Monitoring System (RCMS). The RCMS is the third piece of the puzzle. It provides the means to control and monitor the DAQ system itself. The RCMS and DCS are described in sections 3.2 and 3.3 respectively. These two systems

interoperate with the data acquisition components through a distributed processing environment called XDAQ [53], as shown in Figure 3.3. XDAQ, or cross-platform DAQ framework, is composed by industrial standards, open protocols and custom libraries. This framework offers the following functionalities:

- communication within the same processing unit and among tasks distributed on distinct computers;
- interoperability among application using different communication protocols;
- access of custom devices connected directly to the computers or through bus adapters;
- configuration, control, and monitoring of the application components;
- scalability, portability across operating systems and hardware platforms, robustness, and flexibility over different networks and protocols.

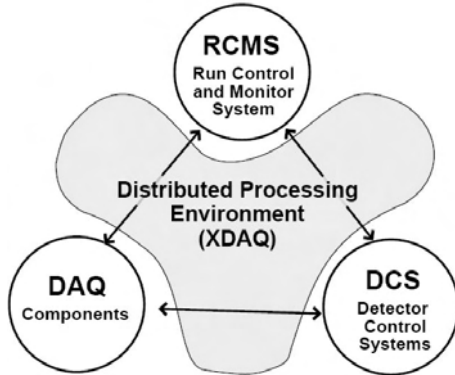


Figure 3.3: Subsystem connected via the XDAQ [52].

3.2 Run Control in CMS

The Run Control and Monitor System (RCMS) [54] is the collection of hardware and software components responsible for controlling and monitoring the CMS experiment during data taking. Its main functions are: to ensure the correct operation of the experiment, to control and monitor the data acquisition and trigger system, and to provide an user interface for

accessing the system and simplifying any operation need during data taking. The monitoring information refers to performance parameters, error or warning messages, and raw data events. The system will also provide the tools to define and store the configuration of any subsystem for late retrieval. To achieve its goals, the RCMS must interface to the DCS, the data acquisition components and the trigger system. This is accomplished by the XDAQ environment discussed above.

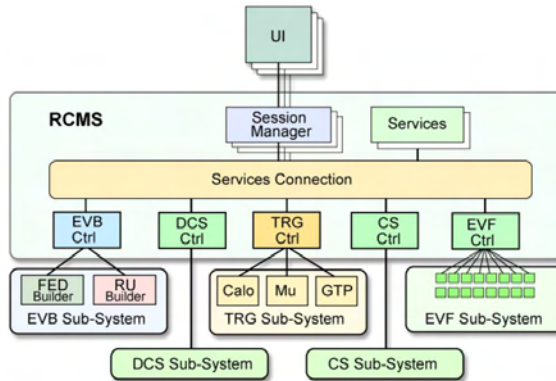


Figure 3.4: Session Managers and subsystems defined in the RCMS.

The DAQ architecture, overviewed in the preceding section, counts roughly 10^4 objects that need to be controlled. A system of this magnitude imposes a hierarchical, scalable and distributed approach in the planning of its control network. For this reason, the RCMS treats the experiment as a set of partitions, as shown in Figure 3.4. A partition is the smallest group of entities that can be configured and operated standalone. The execution of a partition is called a session. More than one partition can run independently at the same time and share resources. The actions of each session are coordinated by a Session Manager (SMR). The SMRs receive the incoming commands and propagate them to the Sub-System Controllers (SSCs). The SSCs consist of a number of Function Managers (FMs) and local database services to facilitate software and configuration download, monitoring, and logging operations. The FM of a given partition receives the commands from the SMR and sends them to the interested sub-system. All the information, as the actions performed, the status, monitor data, and error messages, is logged and analyzed by the RCMS.

Of particular relevance is the interconnection between RCMS and DCS. Two alternative solution have been developed [55]. In the first case (Figure 3.5 a), each element is managed by the central system. The top node therefore, is the only communication route with the RCMS. In the second solution, the subdetectors elements are integrated in the subdetector itself.

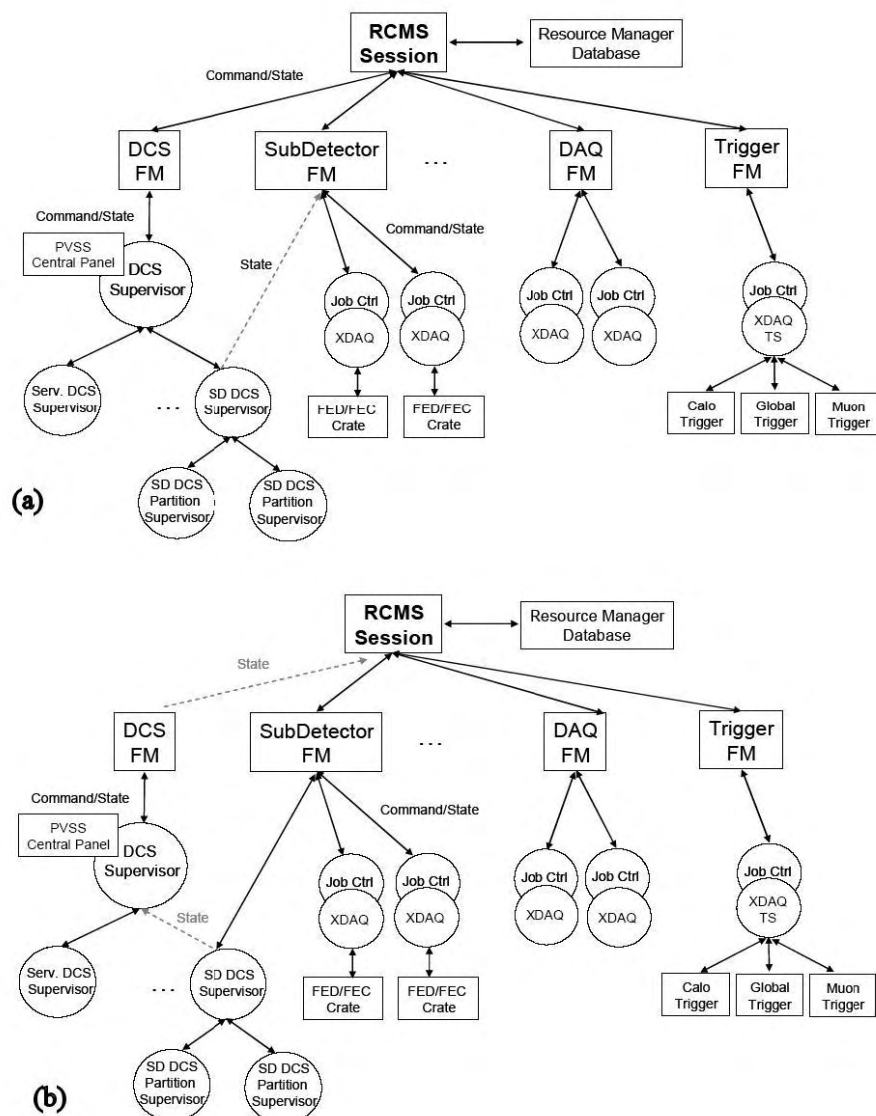


Figure 3.5: Integration of the DCS in the online system.

The central DCS receives only the information of the state of each element. The control and monitoring is assigned to the Subdetector Function Managers. This solution allows a better integration of the readout components of the subdetectors with the DCS activities.

The RCMS provides other services to support interaction with users and manage system resources. These services, shown in the block diagram in Figure 3.6, are:

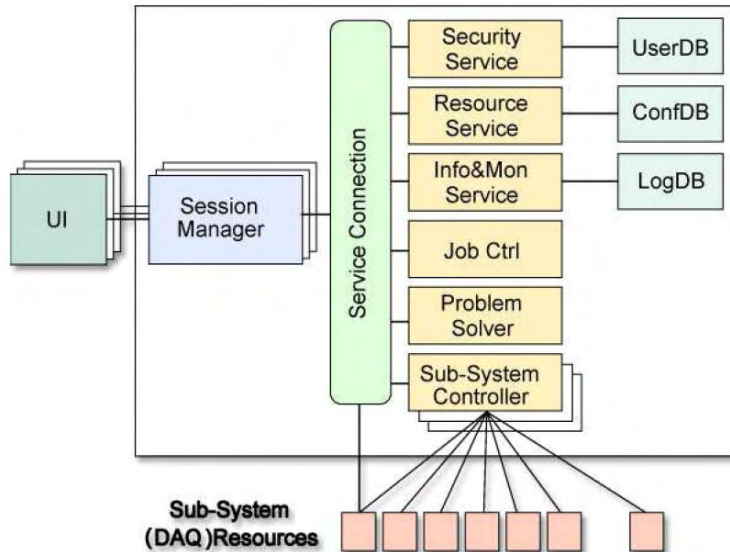


Figure 3.6: Block diagram of the RCMS.

- the Security Service, which provides login and user account management functions;
- the Resource Service, for accessing the configuration database (ConfDB) that stores all the information about partitions and DAQ resources;
- the Information and Monitor Service, that collects messages and monitor data coming from DAQ resources or internal RCMS components and stores them in a database (LogDB) adding auxiliary information (error priority, data and time, etc.);
- the Job Control, which controls and monitors the evolution of all processes during data taking;
- the Problem Solver, whose role is to identify possible malfunctions and react with automatic procedures.

3.3 The Detector Control System

The primary function of the DCS [52] is the overall control of the detector status. It takes appropriate corrective actions to maintain the detector stability and ensure high quality data. It provides an adequate user interfaces for experts or simple shifters. In addition, it communicates with external system as the RCMS, databases, and the control systems of the accelerator. The DCS system is fully integrated in the overall online system as illustrated in Figure 3.7 Another main task of the DCS is control and

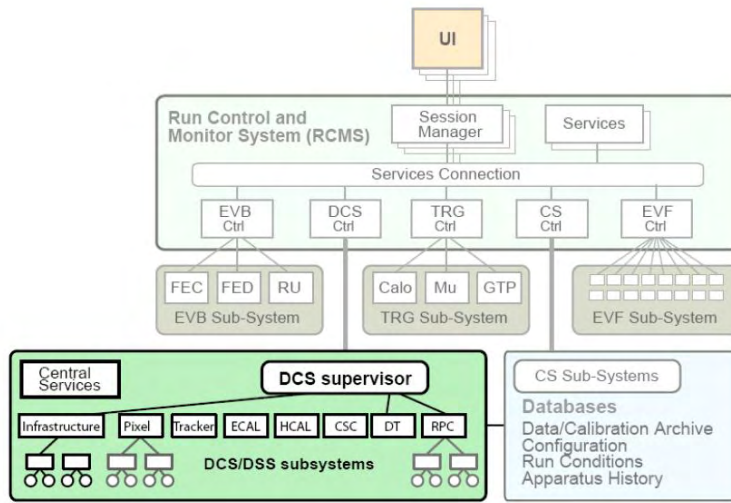


Figure 3.7: Integration of the DCS in the online system.

monitoring of the systems environment at and in proximity of the experiment. These tasks are historically referred to as “slow controls” and include: handling the power supply to the detector, control of the cooling facilities, environmental parameters, gas system, crates and racks. Also safety related functions, as smoke and gas leakage detection, will be foreseen by the DCS in collaboration with the Detector Safety System (DSS)[56] and CERN Safety Alarm Monitoring (CSAM) [57]. This last system addresses critical security issues, where human lives are at threat.

Many functions of the DCS are needed at all time. Thus the technologies and solutions adopted must ensure a 24-hour functioning for the entire life of the experiment.

3.3.1 General Requirements

The general system requirements on the CMS DCS are:

- **Partitionability.** The ability to partition the DCS system is essential for a detector like CMS, which has a large number of subdetector elements. Partitioning implies that a specific sub element can be cut off from the rest of the system and operated independently. This operation mode is useful for maintenance and calibration.
- **Modularity.** Modularity is achieved through a hierarchical structure of the DCS.
- **Homogeneity.** This characteristic will facilitate integration, maintenance, and upgrading. The usage of commercial hardware and software follows this guideline.
- **Scalability.** An important uncertainty for the DCS is the exact size of the system to be installed for the first physics run, as well as the evolution of the accelerator and experiment performance. Scalability makes the system flexible enough to facilitate the introduction of select new technologies in its various parts.
- **Automation.** Automation features speed the execution of commonly performed actions and avoid human mistakes typical in repetitive routines.
- **Radiation tolerance.** The DCS hardware components placed in proximity of the detector will suffer high radiation levels (from 1 to 100 kGy/year). Therefore, radiation tolerant components are mandatory and sensitive equipment should be placed as far as possible from the interaction point.

Besides these general requirements, each subdetector has some specific ones resulting from its unique design and implementation. The specific characteristics of the RPC DCS will be discussed in section 3.5.

3.3.2 DCS Architecture

The CMS control system is geographically organized on three levels, as shown in Figure 3.8. The high radiation levels, the intense magnetic field, the dimensions of the detector, and the expected lifetime of the experiment have imposed this choice. The surface control room and the underground electronics room will be accessible during run times; the cavern will be obviously interdicted. Upgrading and maintenance at this level will be possible only occasionally.

Logically, the control system is organized in two main layers: the front-end layer and the supervision layer. The front-end layer is responsible for giving access to the equipment, while the supervision layer offers an interface to the different human users and high-level operations of the experiment.

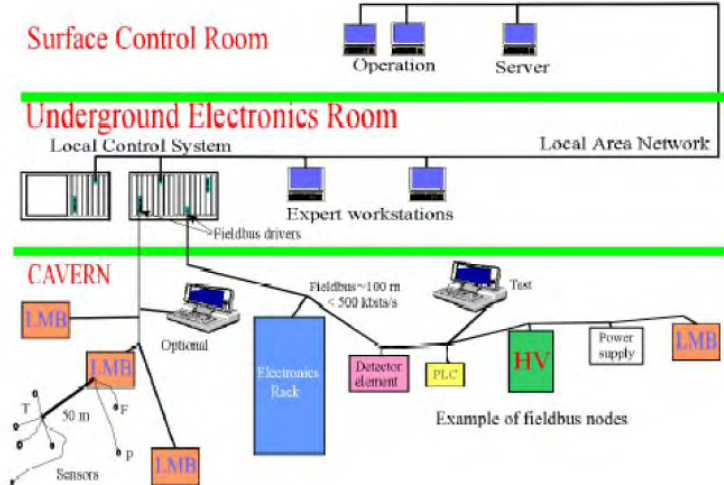


Figure 3.8: General architecture of the DCS.

The front-end elements [58] vary from simple sensors to more complicated objects, as front-end computers. The supervision layer, instead, is based on a commercial tool, a Supervisory Control And Data Acquisition System, commonly known as a SCADA [59].

SCADAs are commercial softwares used extensively in industry for the supervision and control of industrial processes. It must be pointed out that SCADAs are not full control systems. Rather, they are software packages positioned on top of the hardware to which they interface. They are now penetrating in the experimental physics laboratories for the control of ancillary systems such as cooling, ventilation, power distribution etc. In high energy physics, requirements are more stringent. The dimensions of modern detectors and the hostile operating environment ask for robust and reliable online control systems for remote access to the experiment. The use of commercial software over custom development, has many benefits, also for very demanding and complex control system as those of physics experiments. First, they offer all the standard functionalities of an acquisition system, such as user interfaces, alarm handling, access control, connection to external databases for data archiving and a flexible distributed architecture. Secondly, the amount of effort invested in a SCADA product is roughly 50 to 100 p-years. SCADA systems have made substantial progress over the recent years in terms of scalability, performance, and openness. In addition, the engineering development that needs to be performed by the end-user is limited. Finally, technical support and maintenance are often guaranteed by the vendor.

For the LHC, a CERN Controls Board was set up, grouping representa-

tives from the 4 big LHC experiments. The result was the formation of the *Joint Controls Project* (JCOP). The JCOP aims to reduce the overall man-power cost required to produce and run the experiment control systems. Its first decision was to recommend the use of PVSS II [60], the SCADA software of the Austrian company ETM. The use of the same SCADA for all four the major experiments offers a common framework background and homogeneous and coherent DCS systems. All operators will have the same “look and feel” whatever part of the experiment they control. In addition, a consistent number of components will be used by many, if not all subdetectors of all LHC experiments. This is particularly true for auxiliary systems. It is the aim of JCOP to provide standard solutions and support for these common components. For example, the rack and crate control is developed in a single project for all four detectors. This system must manage the power distribution, the cooling system (both air and fluids), and fire detection. The role of JCOP and the architecture of PVSS will be discussed in section 3.4

3.4 DCS software tools

PVSS II [60] is the German abbreviation for “Process visualization and control system II”. It is a SCADA system designed specifically for the operation and supervision of technical installations and industrial processes. Nevertheless some of its features make it interesting for high energy physics applications. Among its strengths it has multiple platform support (Windows and Linux), advanced script capabilities, and it can run in a distributed manner. PVSS will be used at LHC to operate, configure, initialize and monitor the behavior of hardware and software applications by connecting to them and acquiring the data they produce. In addition to all main features of a typical SCADA system, PVSS II offers the following components and tools:

- A run time database where the data coming from the devices is stored, and can be accessed for processing and visualization purposes.
- An internal database for archiving data for long term storage. The information can be retrieved later by any user interfaces or other processes.
- A powerful alarm generation and handling tool. With this tool it is possible to define alarm conditions to data arriving in PVSS. The alarms are stored in an alarm database and can be selectively displayed, filtered, and summarized.
- A graphical editor (GEDI/NG) which allows to design and implement personal user interfaces, called panels.

- A scripting language to interact with the data stored in the database, either from a user interface or from a process that runs in background, i.e. hidden to the user. The scripts are called CTRL scripts and follow the C syntax, but with many extensions.
- A graphical parameterization tool (PARA) offers the users the possibility to define the structure of the database, what data should be archived, what data coming from devices should generate alarms, etc.
- Drivers providing the connection between PVSS and common hardware and software components. PVSS accepts also user made drivers.

3.4.1 PVSS

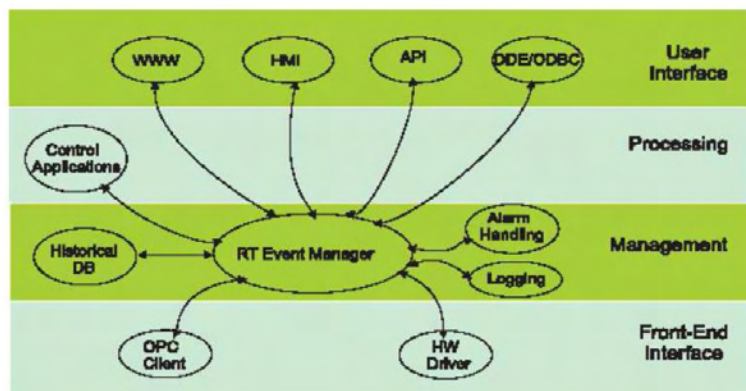


Figure 3.9: Architecture layout of a PVSS project.

PVSS has a highly distributed architecture. All PVSS applications are composed of several processes, called *Managers* (figure 3.9). The Event Manager is responsible for all communications. It receives the data from the Drivers and sends it to the Database Manager and any other Manager which has subscribed to it. The processing level contains the Control Manager, which runs background scripts. The language is extended C. The User Interface Manager administrates all interaction with the user. In particular, the Graphical Editor, allows users to design their own user interface, called *panels*. Also, remote access to the applications is guaranteed through a dedicated server with many World Wide Web characteristics. And, to complete the user interface level, the Application Programming Interface (API) Manager allows the user to access data with custom scripts in C++.

In many SCADA systems, all data associated with a particular device is held in separate variable. PVSS, instead, the data administration is device-

oriented and benefits by an Object-Oriented approach¹. The device data in PVSS II is organized in Data Point Types (DPTs) and Data Points (DPs) allowing an abstract modeling . A DPT defines the data structure of the device (the class), while the DP contains the information related to one of its particular instances (the object). For each DPT, the user can defined as many properties and attributes, i.e. Data Point Elements, as needed. The Data Point Elements (DPEs) may be of type read and/or write.

3.4.2 JCOP Framework

An important quality of PVSS II is the possibility to easily integrate custom instrumentations and applications. The JCOP group has used this characteristic to produce an experiment independent framework supporting common needs of all four LHC experiments [61]. This framework, in addition to PVSS, uses another standard selected tool, SMI++ (State Management Interface). SMI++ is the Finite State Machine (FSM) tool developed for the DELPHI experiment. In fact, one of the first tasks of the JCOP framework group was the integration of SMI++ in PVSS with the use of a dedicated API manager.

An overview of the framework components is given in figure 3.10 and briefly described in the following:

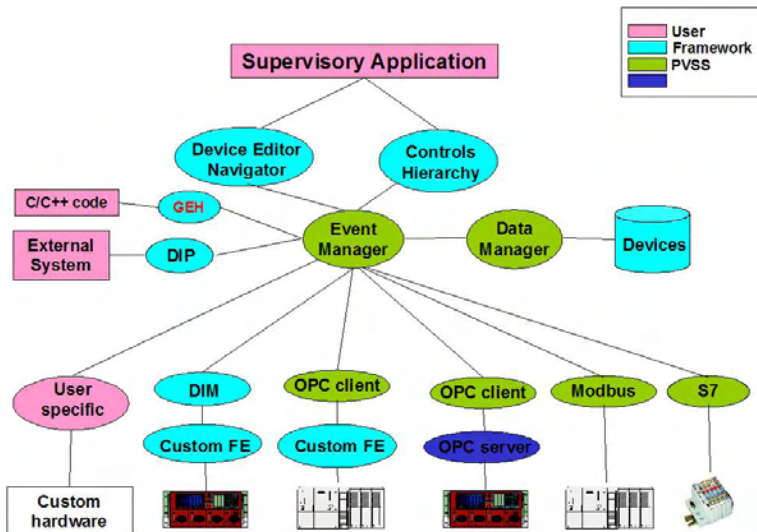


Figure 3.10: Overview of the framework provided components.

¹Object-Oriented programming is a computer programming techniques in which the data structure and the procedures that act on it are grouped in a single entity, a class. Thus, a software “object”, i.e. a particular instance of a class, is created containing both proprieties and methods.

Device Editor/Navigator is the main interface of the framework. It provides three distinct system views; hardware, logical and the FSM view. It also allows the configuration and the operation of devices². Moreover, it is the tool used to navigate throughout the control system.

Controls Hierarchy Simplifies the definition of the hierarchical structure of the system and of its behavior by including the FSMs.

Trending Tool extends the PVSS trending function introducing new templates. The data displayed in the plots is stored in an user specified Oracle database or in the internal PVSS database. The data is retrieved when the plot is reopened.

Mass Configuration allows to easily configuration multiple devices subsets.

Installation Component is the tool through which all framework provided and custom components can be imported in a PVSS application.

Configuration Database allows to store the system configuration, the physical and logical device addresses. The data can be accessed to restore the system or simply to configure the hardware.

Generic External Handler offers a simple way (compared to the standard PVSS C++ interface) to incorporate C++ code in the panels and control managers.

The framework provides complete components for commonly used equipment as CAEN high voltage supplies. Complete means any necessary servers or driver, the PVSS definitions in terms of Data Points Types and Data Points, any control scripts and script libraries and all panels necessary to configure and operate the device.

The JCOP framework also offers tools, reference panel and script libraries for the developers to integrate their own devices or build new ones. These tools have been used during this thesis to integrated the A3801A CAEN board for RPC temperature monitoring. Details will be given in section 3.6.5.

Concluding, each experiment clearly has additional requirements, common to all subdetectors. The realization of an “experiment framework” is an intelligent solution to minimize development efforts. Hence, constraints on the design of the control system and interfaces imposed by the central DCS team of each experiment will ensure a coherent and uniform control application across the detector. The CMS DCS general requirements are illustrated in section 3.6.6. In the same section, we present the specific solution adopted to meet these requirements during the design of the Endcap RPC control application, main objective of this thesis work.

²A device represents a portion of the hardware or a logical group of hardware elements.

3.5 The RPC DCS: hardware system

The RPC Detector Control System has been designed and built by the INFN group of Naples and myself in collaboration with the DCS CMS group and with the JCOP CERN group.

The main aim of the RPC DCS is to monitor the detector conditions and their performance and to control and monitoring all the subsystems related to the RPC and to their electronics. The high and low voltage systems, the gas and cooling systems, the front-end and trigger electronics and the environmental parameters are the subsystems to control and monitor during any type of data taking, in order to assure a correct and stable operation and the whole RPC system. All parameters have to be monitored in real time and stored in a permanent database in order to give the possibility to all the people to analyze the data and study the detector and trigger performance as it will be described in the chapter 4. In the section 2.6 we described how RPC operation and performances are related to the environmental conditions as pressure and temperature. In addition we pointed out the importations of having a stable and robust high voltage system in order to assure stable conditions of the detector and of the muon trigger, strictly correlated to the detector efficiency. In this paragraph we will described the main hardware components of the RPC detector related to the DCS and how this have been designed to fulfilled the requirements of the RPC system.

3.5.1 Power system: the High and Low Voltage systems

General requirements

The main requirement of the LHC power system is to work in a very “unusual” hostile environment due to the high magnetic field and high radiation flux. For the muon system the idea is to have a large part of the power system close to the detector: in racks on balconies placed around the barrel wheels and the endcap discs. In this area the magnetic field can reach up to 1 Tesla while the radiation is around 5×10^{10} protons/cm² and 5×10^{11} neutrons/cm². Starting from the experience of the past experiments (L3 and BaBar), where the condition were much more safe than in CMS, and after a very deep market surveys, the group of Naples decided to start a new design of a RPC power system able to work at LHC. This was done in cooperation with the ATLAS, ALICE and LHCb Italian colleagues working on RPCs. The design phase and study began in 2001. After some very preliminary tests a first prototype was produced in order to carefully test it in laboratory and at the radiation facilities at CERN. The specific requirements for the RPC HV and LV power supply are reported in table 3.1.

Power supply	High voltage	Low voltage
Hostile Environment	Yes	Yes
Voltage	12 kV	7 V
Current	1 mA	3 A
Ripple	<100 mV pp at load (freq < 20MHz)	<10 mV pp at load (freq < 20MHz)
Programmable Voltage	0-12 kV	0-7 kV
Monitored Current precision	0.1 μ A	100mA
Monitored Voltage precision	< 10 V	100 mV
Trip settings	0-100 s	0-100 s

Table 3.1: The high voltage and low voltage power supply requirements are reported here.

One of the most important requirements concerns the “noise” of the LV and HV boards. This parameter is strictly correlated to the detector noise and, therefore, to the trigger rate (see section 2.6). Attention is also payed to the voltage and current monitored precision, to allow the DCS system to follow the possible dark current excursions in a very accurate way.

The RPC power system architecture

The high voltage power systems for RPC detectors have been, in the past, always designed with a central unit, called mainframe, containing both power supplies and control and monitoring system. The mainframes were placed in the electronic room and the high voltage channels were connected to the detectors through very long cables (up to 100 m). Patch panels or high voltage distributors were used to reduce the number of channels. Viceversa, the low voltage power supply was always placed in the detector area, in order to minimize the noise pickup and the voltage drop due to long cables. The LV were controlled and monitored using serial communication protocol and remote hardware switches.

At the LHC, taking into account the hostile environment and the requirements described before, the RPC community decided to design a system based on a master/slave architecture for both the high and low voltage systems. This new system was called EASY and it will be described in the next paragraphs. The master, always called mainframe, is supposed to control and monitoring one or more slaves. It is placed in a safe and accessible area as an electronic room. The slave is where the power is generated and is designed to be modular and multifunctional. It is based on a crate with a dedicated backplane housing a certain number of boards of different nature (HV power supplies, LV power supplies, etc.). The slave system can be placed around the detectors, in a hostile and not accessible area and for

this reason has to be modular, redundant and based on a radiation tolerant electronics. In a second moment the RPC collaboration decided to keep the master/slave architecture for both the high and low voltage systems but to move all the high voltage slaves in control room for safety reasons. The HV system, in fact is crucial for RPCs. This choice and also to reduce the cost of the project. Furthermore, keeping all the HV system in a safe and accessible area gives us the possibility to reduce the number of HV channels of a factor two (using HV passive distributors) and to improve the system when it will be necessary.

Low Voltage Architecture for RPC detectors

In order to minimize the noise pickup and the high voltage drop and to reduce the cost of the Low Voltage project, the CMS collaboration decided to design and develop a common LV project based on the master/slave architecture, as described before. The Muon collaboration, after having analyzed the general requirement decided to have a LV slave system placed on the balconies around the detector, in a hostile region but at a maximum distance of about 15 m from the detectors (instead of the 120 m that separate the electronic room from the detectors).

High Voltage Architecture for RPC detectors

Since the year 2000, the CMS RPC collaboration decided to use the master/slave architecture for the High Voltage system but without a very clear idea regarding the geographical distribution of the system itself. For this reason the collaboration began to carefully test the first prototypes produced (EASY 2000) and to work on two different solutions; the first very similar to the LV, where the power supplies were on the detector and the master in the electronic room and a second one, with the full HV system is in electronic room. The experience, made in the past experiments with the RPC detectors, suggested us that it is very important to have constant access to the power supplies in order to easily fix any problem regarding the connection and the distribution of the HV. Sparks, generated in HV connections or in a chamber, can create a fail of one or more power supply and, in some special case, of the whole HV mainframe. In these cases, it is very important to access as soon as possible the incriminated HV channel, disconnect it and repair the problem. Another situation in which it is important to have a comfortable access to the power supplies is when one or more chambers begin to draw too much current. The faulty chamber needs to be moved to a different HV channel where it is possible to study and fix the problem without disturbing the operation of the whole RPC sub-detector. Concluding, taking into account the arguments discussed before and the cost reduction due to the possibility to have the same number of HV channels in a reduced number of slave crates, the RPC collaboration decided to adopt the second solution, i.e. to have the whole HV system in

an accessible and not hostile area as the electronic room.

The EASY project

EASY stands for Embedded Assembly SYstem [63] and is the CAEN master/slave power supply solution for operation in magnetic field and radioactive environment, indispensable for the LHC experiments. The master SY1527 (mainframe) houses up to 16 the A1676A boards that is the interface between the master and the slave system; the EASY 3000 crate. The EASY3000 can house different EASY boards (high and low voltage, ADC and DAC). The channels of the EASY3000 boards operate as channels of the A1676A and can be accessed through the mainframe. The EASY architecture foresees two independent 48 V power supplies: the first (48 V Power) to power the channels regulators, the other (48 V Service) to power the control logic. The use of CAEN 48 V power sources (Mod. A3484 and A3485), allows to integrate into the channels control also the management of the 48 V power supplies. When the master/slave structure has been decided up to the channels level the User has to configure the A1676A to operate with the EASY crate, by using a provided software tool, the CAEN EASY Rack Builder. The configuration file contains all the information about number, type and position of the boards in remote EASY crates. When the physical layout of the boards and EASY crates is changed, a new configuration file should be uploaded on the branch controller. The EASY system is connected to the external world through a serial port and an ETHERNET³ interface on the mainframe. This allows the user to monitor and control the whole system with different softwares; from a very easy TELNET interface to a more sophisticated OPC protocol. Through the OPC protocol any SCADA application has, therefore, the possibility to set or monitor operational channel parameters, control alarm messages for each channel and for the mainframe, and monitor the communication from inside the network. This was the communication procedure adopted also for the control system developed during this thesis work. The communication schema is shown in figure 3.11. OPC (OLE for Process Control) [64] is most popular standards in industry automation. OPC is an open interface based on the OLE/COM (now ActiveX) and DCOM technology. Its main advantage is the reduction of the number of driver developments which hardware manufacturers implement for their components to only one. The OPC server/client for the EASY system has been developed by CAEN and the IT-CO group at CERN. In the EASY system the OPC client applications can communicate with the OPC server to exchange data in a standard way. Each device property is accessed via an OPC item. An OPC server creates OPC items on behalf

³ETHERNET is family of computer networking technologies for local area networks (LANs). The name comes from the physical concept of the ether. It defines a number of wiring and signaling standards for the physical layer, two different means of network access, and a common addressing format.

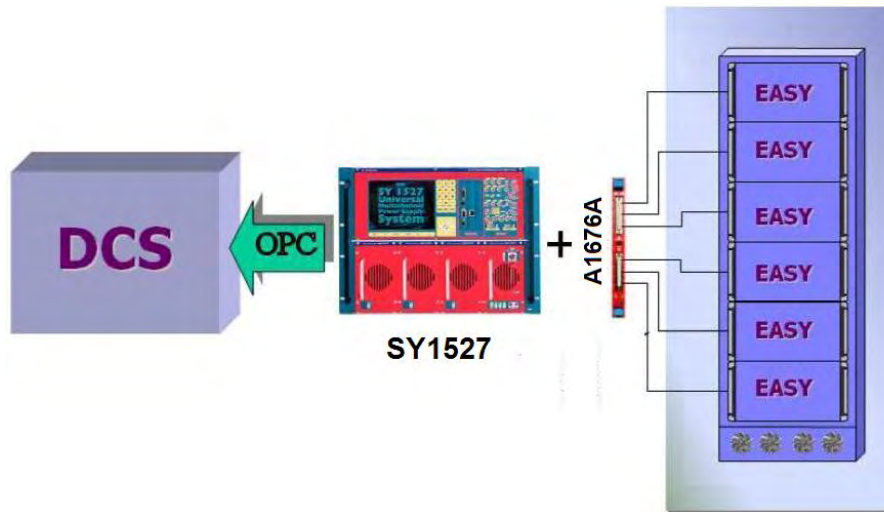


Figure 3.11: Interfacing of the DCS with the power distribution system.

of an OPC client. The client's OPC items are organized in OPC groups with a hierarchical structure. The JCOP framework CAEN tool, provides the necessary OPC client to control and monitor hardware through PVSS applications.

The mainframe

The mainframe is housed in a 19'-wide, 8U-high euro-mechanics rack and hosts four main sections:

- - the Board Section, with 16 slots to house boards, distributors and branch controllers;
- - the Fan Tray Section, housing 6 fans arranged on two rows;
- - the Power Supply Section, which consists of the primary power supply and up to 3 power supply units;
- - the CPU and Front Panel Section which includes all interface facilities. The board section can hold up to 16 branch controllers. The RPC collaboration has chosen to use A1676A EASY Branch Controller.

The EASY crate (slave)

The EASY crate can house all EASY boards in any configurations. It has been designed to work in an hostile area with a magnetic field up to 2kGauss and a radiative environment up to $1 \times 10^{11} p/cm^2$ TID, $2 \times 10^{12} n/cm^2$ TID and 15 kRad TID.

The High Voltage hardware

The Model A3512 [65] is a double width board with 6 H.V. floating 12 KV/ 1 mA channels with either positive or negative polarity. The six channels have an independent return in order to avoid any possibility to generate noise due to ground loop (long cable between HV boards and chambers). To follow the strong requirement made for the RPC detectors the board has been designed with an output voltage that can be programmed and monitored in the range 0-12 kV with 1 V resolution and with a monitored current resolution of 0.1 A. This current resolution allows the DCS system to study the current behavior of every chamber with a precision of at least 1/10 of the measured current (between 10 and 20 A per chamber). The board is equipped with a set of hardware warning and alarms for abnormal operating conditions. For example, if the output voltage differs from the programmed value by more than 3% of voltage full scale range, the channel is signaled to be either in OVERVOLTAGE or UNDERVOLTAGE condition. Moreover, for each channel, a voltage protection limit SVMAX can be fixed via software with 1 V resolution and the output voltage can not be programmed beyond this value. The technical characteristics of the A3512 board are given in table 3.2.

Polarity	Positive (A3512P) or negative (A3512N) with floating return
Output Voltage	0 ÷ 12 kV
Max. current output	1mA
Voltage Set/Monitor resolution	1 V
Current Set/Monitor resolution	100 nA
Vmax hardware	0 ÷ 12 kV
Vmax software	programable (0 ÷ 12 kV)
Voltage ripple	< 50mV pp

Table 3.2: Channel characteristics of the Mod. A3512 HV Board.

The Low Voltage hardware

The CAEN A3009 [66] is a 12 Channel 8V/9A Power Supply Board for the EASY Crate. It has been developed for operation in magnetic field and moderate radioactive environment. The connector output voltage range is 1.5 ÷ 8 V with 5 mV monitor resolution. Channel control includes various alarms and protections. The board is provided with Remote Sensing Lines to compensate for the voltage drop over the connection cables. If the output voltage differs from the programmed value by more than 3% of voltage full scale range, the channel is signaled to be either in OVER VOLTAGE or UNDER VOLTAGE condition. Moreover, for each channel, a voltage protection limit SVMAX can be fixed via software with 5 mV resolution and

the output voltage can not be programmed beyond this value. The output current is monitored with 10 mA resolution; if a channel tries to draw a current larger than its programmed limit it is signaled to be in OVERCURRENT condition; the SY1527 system detects this state as a fault and reacts according to the setting of the TRIP parameter, which can be programmed in 0.1s steps from 0 to 1000s. Actually TRIP = 1000 s means infinite: in case of TRIP infinite the output current is permitted to keep the programmed limit. If the maximum output current value is reached the channel behaves like a constant current generator. In case of $\text{TRIP} < 1000 \text{ s}$, the output current is permitted to keep the limit only for programmed time interval and then is switched off. The maximum output voltage (VMAX) and the maximum output current (IMAX) can be fixed for each channel, through trimmers located on the front panel. The technical characteristics of the A3512 board are given in table 3.3.

Output Voltage	$1.5 \div 8 \text{ V}$
Max. current output	9 A
Voltage Set/Monitor resolution	5 mV
Current Set/Monitor resolution	10 mA
Vmax hardware	$1.5 \div 8 \text{ V}$
Vmax software	programmable ($1.5 \div 8 \text{ V}$)
Voltage ripple	$< 20 \text{ mV pp}$
Output power	45 W per channel

Table 3.3: Channel characteristics of the Mod. A3009 Power Supply Board.

The RPC High and Low Voltage description

One CMS RPC chamber is made by four or in some cases six gaps (gas volume) organized as bi-gaps as already shown in figure 2.7. In the barrel, each sector is arranged in four detector stations, RB1 (RB1in and RB1out), RB2 (RB2in and RB2out), RB3 and RB4. Both RB1 and RB2 host 2 bi-gaps, each of RB3 and RB4 stations host 4 bi-gaps and only 60 chambers RB2 type host 3 bi-gaps. Although each gap requires one High Voltage (HV) channel to be supplied, the choice of the RPC collaboration is to have one HV channel per chamber, in order to reduce the cost of the HV system by keeping the chamber an independent unit. The LV system has been designed with two low voltage channels per chamber; one for the analog part of the front-end boards and one for the digital part. The idea to have only floating channels for both the high and low voltage and to keep the chamber as an independent unit without mixing different chamber and/or sector has been strongly dictated by the necessity to reduce, as well as it is possible, the noise of the RPC chambers and of the other subdetectors

placed close to the RPCs. The total number of barrel HV and LV channels, in this configuration, is 480 and 720, corresponding the 80 HV boards and 60 LV boards. The LV boards will be placed around the detector in 20 EASY 3000 crates (4 per wheels) and they will be connected to one master crate placed in the control room. The whole HV system will be place in control room and consists of 14 EASY 3000 crates and one master mainframe. The endcap power system has been designed following the same architecture and consists of about the same numbers of boards and crates, but it is not under Italian responsibility.

3.5.2 Temperature Monitoring

Resistive Plate Chambers are very sensible to environmental changes, and the importance of knowing the chamber temperature has been extensively pointed out in 2.6. Differences in temperature can result in different chamber response and efficiency, leading to systematic errors. Any detector based on Resistive Plate Chamber technologies is to follow these requirements:

1. work at a temperature between 20 and 24 °C in order to keep both dark current and noise rate at nominal values.
2. monitor the temperature and atmospheric pressure in order to compensate, in real time, the operating point (high voltage value) of every chamber. The danger is to work at low effective voltage and therefore, in an inefficient region or at a high effective voltage, speeding the ageing effects on the detector.

The RPC project was designed keeping in mind these two very important points and stressing the crucial role of the cooling and DCS systems. A lot of tests and studies have been performed by the CMS collaboration to understand the temperature map of the iron and to estimate the possible heating sources in the front-end electronic system of the DT and RPC detectors in order to design the cooling systems in the best way. To ensure “thermal” coherence throughout the detector, the muon system is provided with two dedicated cooling networks. One for the Drift Tubes and RPC electronics and one magnet iron return yoke. The coolant used is water. This precaution was taken even if CMS is collocated about 100 meters underground and the RPC detectors are placed in the iron (~ 2000 t per wheel). Despite the cooling system, temperature differences are possible among the various chambers and for the same chamber at different moments. The RPC DCS (see section 3.6) has the task to monitor the temperature for each chamber and archive the information for offline analysis.

The INFN group of Naples designed and built the Temperature Sensor (T-sens) system for the RPCs, both from the hardware and software point

of view. The software part is one of the main items of this thesis and will be described in the following sections. Coming back to the hardware, the temperature system is formed by one sensor per chamber to monitor the RPC temperature of the iron gap and two sensors on hot spots of the front-end electronic boards. This adds up to a temperature network of about 480 sensors in the iron and about 5000 sensors for the frontend electronics. This, combined with information coming from the cooling system, is more than enough to map the chambers' temperature.

After extensive tests on various temperature sensors, the choice fell on the AD592BN sensor produced by Analog Devices [67]. The sensors is designed to work in hostile environments (as in LHC experiments) and has a good quality - price ratio.

After choosing the sensor, the attention was focused on the way to read-out the sensors using the DCS system. The INFN group of Naples designed and built, in collaboration with CAEN, a board specifically for the sensor and compatible with EASY crates already used in the HV e LV systems (thus reducing costs), the A3801A [69]. This board is an ADC with 128 channels, equipped with an input stage able to supply 12 Volts to the sensors and in parallel to read the current generated by them with a resolution of less than $0.5 \mu\text{A}$ corresponding to 0.5°C .

The temperature sensor: AD592BN

The AD592BN [67] is a two terminal temperature transducer that provides an output current proportional to absolute temperature. Its operating principle is based on the characteristics of silicon transistors. When these transistors are opportunely polarized, the output characteristic is linearly proportional to the temperature. At this point, the output current (in μA) is forced equal to the temperature in degrees Kelvin. This temperature transducer acts as a high impedance temperature dependent current source of $1\mu\text{A}/\text{K}$. Because the AD592 is a temperature dependent current source, it is immune to voltage noise pickup and IR drops in the signal leads when used remotely. The operating temperature range is $-25^\circ\text{C} - +105^\circ\text{C}$, while the supply voltage can vary between 4V and 30V. The precalibration error if 0.5°C at 25°C , fulfilling our requirements of 1°C accuracy.

Three primary limits of error are given for the AD592. They are the calibration accuracy at $+25^\circ\text{C}$, and the error over temperature from 0°C to $+70^\circ\text{C}$ and -25°C to $+105^\circ\text{C}$. These specifications correspond to the actual error the user would see if the current output of an AD592 were converted to a voltage with a precision resistor. Figure 3.12 graphically depicts the guaranteed limits of accuracy for an AD592BN.

The AD592 has a highly linear output compared to older sensors like thermistors, thermocouples, etc. The nonlinearity, that is the maximum deviation from the mathematical best fit, is typically 0.1°C and never greater than 0.35°C . Figure 3.13 is a plot of typical AD592BN nonlinearity over the

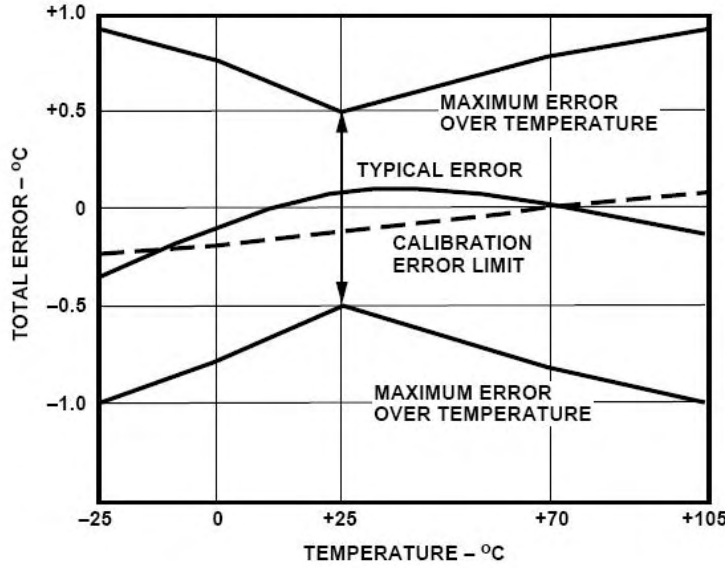


Figure 3.12: Error specifications for the AD592BN sensor [67].

full rated temperature range.

Calibration error can be removed with a simple temperature trim. The schema to be followed is shown in figure 3.14. To trim the circuit the temperature has to be measured by a reference sensor and the value of R should be adjusted so the output (V_{OUT}) corresponds to 1 mV/K. More complicated trimming schemas are possible.

The sensors actually mounted on the detector, have been tested at the INFN laboratories of Naples (Italy), but were not calibrated before installation. The sensors were operated with a power supply of 5 V. The output current flew through a resistor of known value and the voltage drop at its ends was measured. The temperature obtained, T_s assuming an ideal behavior of the sensor (output current in μA equal to the temperature in Kelvin) was compared to the temperature measured by a reference sensor, T_r . Subsequently, the reference temperature and output current were related, to test the linearity of the sensors. The results obtained for a specific sensor are presented in figures 3.15.

The tests showed the reliability and good linearity of the sensors; qualities for which this sensor model has been chosen from the RPC collaboration, along with a competitive price.

Sensor power supply and reading

The power distribution and reading of the sensors is done through an

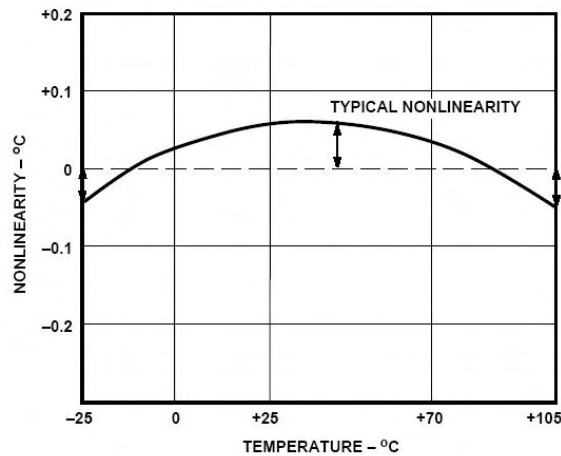


Figure 3.13: Non linearity error for the AD592BN sensor [67].

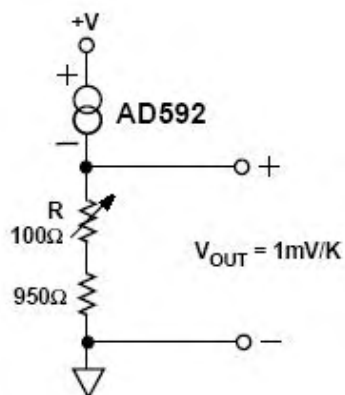


Figure 3.14: Voltage temperature trim schema.

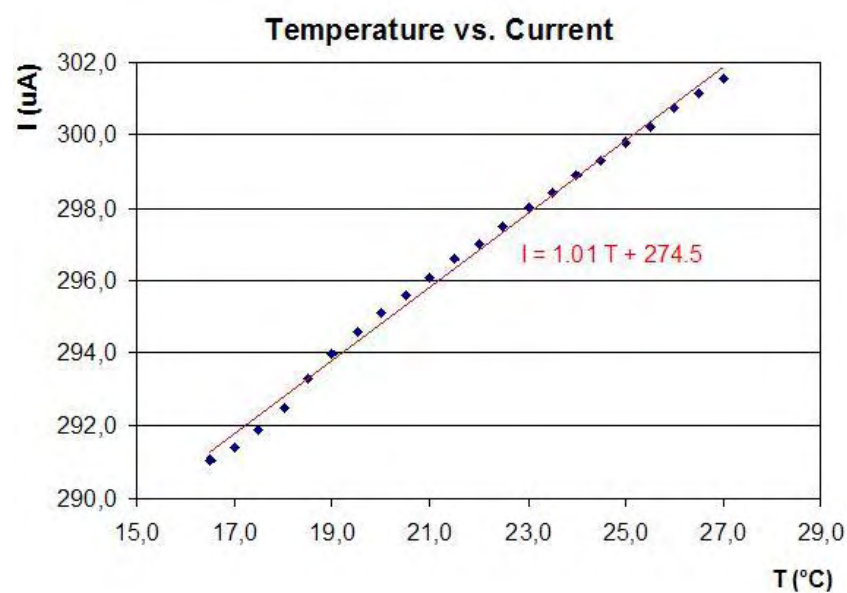


Figure 3.15: Reference temperature in degrees Celsius versus measured current in μA (Studies performed on a AD592BN at the INFN laboratories in Naples).

ADC CAEN modules, precisely the A3801A board [69], specifically designed for the AD592 family of sensors. This module is a 128 channel ADC board with an input range from -45°C to $+125^{\circ}\text{C}$ and 0.1°C resolution, corresponding to $1\ \mu\text{A}$. The temperature values are returned at 2s rate. The technical characteristics of the A3512 board are given in table 3.4.

This module, integrated in the EASY system, is developed to operated

Input range	$-45 \div +125^{\circ}\text{C}$
LSB	0.1°C
Integral non linearity	0.1% of FSR
Interchannel isolation	60 dB
Conversion rate	2 s (for all channels)
Temperature stability	$0.5\ \text{LSB}/^{\circ}\text{C}$

Table 3.4: Channel characteristics of the Mod. A3801A temperature sensor Board.

in intense magnetic fields and highly radioactive environments. The choice made is to place the A3801A boards around the detector in EASY 3000, as already done for the LV system. The ADCs, as all EASY boards, can be controlled remotely through the SY1527 and the OPC server by any SCADA system. How this board was integrated in the RPC DCS is explained in section 3.6.

3.6 Design and Development of the RPC DCS

The main objective of this thesis was the development of a control and monitoring system for the RPCs of CMS and its integration in the general CMS DCS. The DCS application developed uses all the potentialities of PVSS II and of the JCOP framework described in section 3.4. Its main role is the control and monitoring of the power distribution for auxiliary systems and the monitoring of the operating environment. All DCS requirements, specific for CMS and general for the LHC experiments, have been met and framework specifications followed, to insure a uniform and coherent DCS.

3.6.1 Architecture of the DCS

The main challenges for the RPC DCS are the large number of channels and parameters to monitor (~ 15000), the large data volume ($\sim 25\text{MB}/\text{h}$), and the necessity to run the DCS during the whole CMS detector life time. To encounter all these needs, the RPC DCS was developed in a hierarchical

double tree structure: the supervisor FSM tree and the hardware FSM tree. Both trees offer information about the RPC system, but they present it with different points of view. The hardware view is useful when a problem occurs in a particular sub-system (for example the high voltage) and affects several detector parts. The users would need to open multiple panels to correlate the information and understand it. On the other hand, if the troubled sub-system corresponds to a single node in a tree, the correlation is immediate and the solution more rapid. The hardware FSM tree adopted for this DCS application summarizes the different sub-system in single tree elements: the HV system, the LV system, the power supply system (SY1527 crates) and temperature system.

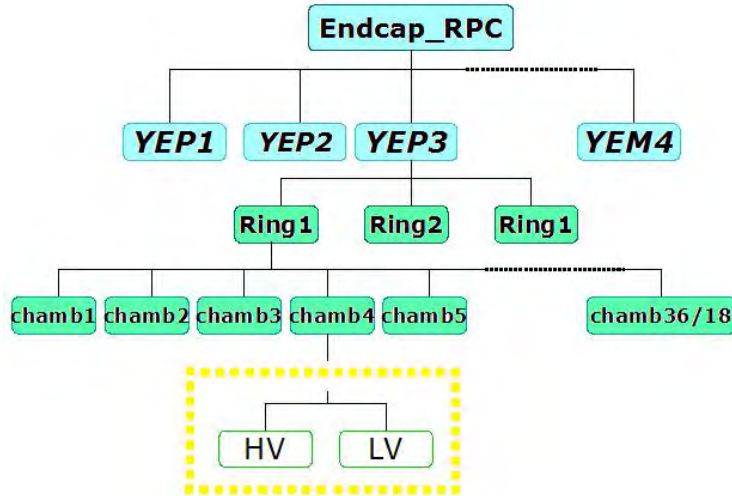


Figure 3.16: Supervisor FSM tree schema.

The supervisor FSM tree, instead, closely follows the geometry of the detector. In particular, the endcap RPC system counts eight discs (four on each end: YEP1,2,3,4 and YEM1,2,3,4), each divided in r in three rings with 18 or 36 chambers per ring. The muon stations YEP4 and YEM4 (farthest from the interaction point) are staged, as well as the chambers in the inner ring of the remaining discs (region at high η). Nevertheless the control system here discussed has been developed thinking at the complete RPC system, but may be used to operate any available fraction of it. The supervisor FSM tree, schematized in figure 3.16, follows this structural layout. The tree is terminated with reference nodes to the high and low voltage channels that power respectively the gaps and the frontend electronics of each chamber. The same approach has been used for the supervisor FSM tree of the barrel region. The geographical division in wheels (WP1,2,3,4 and WM1,2,3,4), sectors (12 per wheel), and chambers has been followed.

The commands are propagated towards the lower levels of the hierarchy trees, i.e. from *parent* to *child node*, where the different levels interpret the commands received and translate them into the corresponding commands specific to the system they represent. The propagation of commands ends at the lowest level, the *device level*. The devices are representations of the actual hardware. The data flow will only be vertical: commands flowing downwards, states and alarms going upwards. A command may trigger state changes at lower level, that in turn may cause state changes at higher ones.

Another important advantage of having a hierarchical structure is the possibility to partition the command hierarchy, essential for a detector like CMS. Partitioning implies that a branch of the main tree is cut off. In this way components can be operated independently from the rest of the tree: the corresponding subdetectors operate independently from the rest of the system. This mode of operation will be used mainly for maintenance, calibration, system testing and trouble shooting. The partitioning modes made available in PVSS by the framework are the following: *Included*, *Excluded*, *Manual*, and *Ignored*. The meaning of each is clearly illustrated in figure 3.17.

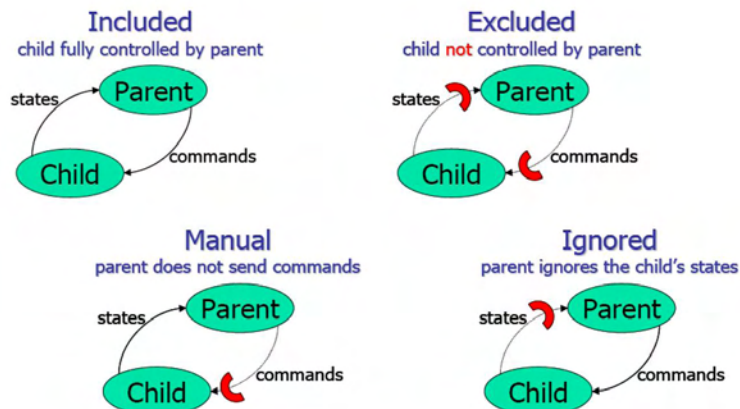


Figure 3.17: Partitioning modes.

3.6.2 The Final State Machine: design and implementation

The RPC system in CMS is a complex and massive structure. These characteristics impose a high rate of automation for control processes, to reduce human errors and optimized recovery procedures. Automation comes with the need to describe the behavior and evolution of the system in the most accurate way. A solution is to view all system subelements (either ab-

stract or physical) as controllable objects whose behavior is defined through finite state automaton. A finite state automaton, or more simply a finite state machine (FSM), is a model of behavior for any complex or simple object with a finite number of states, transitions and actions. A state stores information about the past, i.e. it reflects the input changes from the system start to the present moment. A transition indicates a state change and is described by a condition that must be met to enable the transition. An action, instead, is a description of an activity that is to be performed at a given moment. The action may be executed when entering the state, exiting it or during the transition.

The FSM trees described above are made of three different types of nodes: *Control Units* (CUs), *Logical Units* (LUs), and *Device Units* (DUs). The specific tasks of a DU are to interface to the actual hardware device, implement the actions to be taken on the device, retrieve the device's state, and generate alarms. A CU, instead, is able to configure, monitor and control its children, recover errors, handle alarms and partition the subtree it holds. LUs have the same functionalities as CU, but they may not start a partition, i.e. they can not be root nodes.

The FSM toolkit in PVSS is based on SMI++ and is provided by the JCOP framework. A friendly user interface allows to define the FSM structure for every node. It is possible to specify states, accepted commands, allowed transitions between states and eventual actions to undertake. These functionalities have been used in the RPC DCS. Abstract behaviors have been defined for every node type defined in the FSM supervisor tree (chamber, ring , disc, top node). The states implemented represent possible configuration of the RPC system based on its peculiarities already described. The top node states, actions, and accepted commands have been optimized for the integration of the application in the central CMS DCS. The central DCS treats the different subdetector DCS as children nodes. Therefore the states of each subdetectors top nodes must be recognized by the central DCS and the commands sent back to the subdetectors must be correctly interpreted. General CMS specifications for the DCS impose only the four following states for the root node [70]:

ON - The system is ready to take data.

OFF - The system is not ready to take data, but no problem nor error has occurred.

STANDBY - The system is not ready to take data, but it is in a intermediate state, where the power distribution is not completely turned off.

ERROR - An error has happened and the system is now trying to react to it. Error conditions and recovery procedures are set by each subdetector

depending on its specific needs.

Instead, the implemented commands are:

ON - brings the sub-detector to the state ON.

OFF - brings the sub-detector to the state OFF.

STANDBY - brings the sub-detector to the state STANDBY.

The FSM bubble schema for the RPC top node is shown in figure 3.18. The commands are received by each subdetector and propagated down the FSM tree to the devices, where they are interpreted according to the specific characteristics of the subsystem. When STANDBY is sent to the RPC FSM tree the system reacts keeping the LV off and turning on the high voltage system. The HV value to be reached is read from the configuration database (see section 3.6.4) and is an intermediate value around 6 kV. Thus, the chambers start their ramping towards the operation point, but the amplification factor is still low. This is a safe state for the detector where the operators can perform checks directly on the system. In addition it protects the LV during test and dirty beam runs. The LV is finally turned on and the operating point is reached when the ON command is received. OFF, obviously, turns off the entire system.

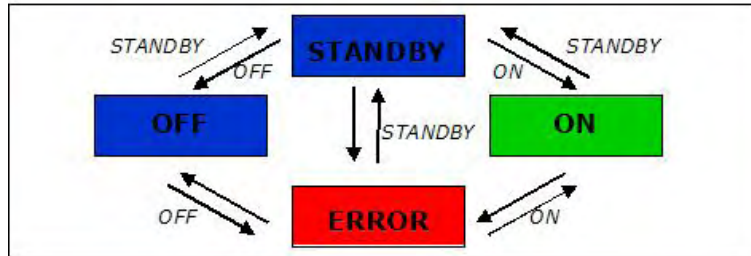


Figure 3.18: FSM bubble schema for the RPC top node.

The FSM objects chamber, ring, disc as well as wheel and sector, have been developed following a common architecture (figure 3.19). This ensures stability and coherence throughout the system. The FSM structure for these nodes has been developed constantly thinking at the hardware components they represent. A total of six states have been defined: ON, OFF, STANDBY, RAMP1STEP, RAMP2STEP, and ERROR. The states RAMP1STEP and RAMP2STEP monitor the system during transaction

between stable states. The system migrates to the ERROR state when the

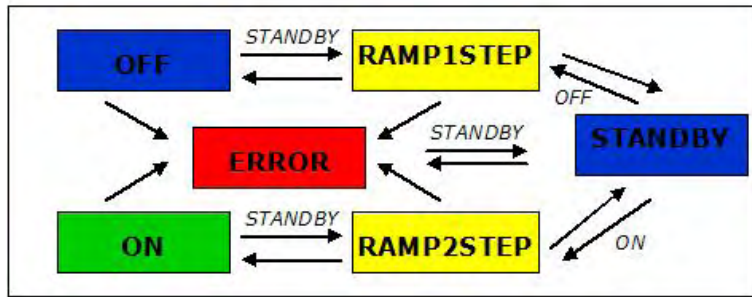


Figure 3.19: FSM bubble schema for the RPC chamber, ring, and disc node.

error conditions are met. This state starts automatic procedure to protect the integrity of the detector.

Finally, the Device Units are not equipped with a standard FSM logic. Instead, they translate the commands in actions on the actual devices and define their stated from the hardware configuration. The RPC DCS developed during this thesis, implements the DUs for all high voltage and low voltage channel. A set of seven states, to ensure a complete understanding of the hardware, have been defined: ON, OFF, RAMPING UP, RAMPING DOWN, WARNING, TRIPPED, and ERROR.

3.6.3 Alarm Handling

An important functionality of a control system is to provide adequate alarm handling. An alarm is issued each time the system unwontedly leaves the desired state or if a given parameter deviates from a predetermined range. The control system alerts the human operator offering details on the anomalous event. Unfortunately, the presence of an alarm does not imply an automatic response of the system. To avoid that the necessary recovery or safety procedures are complete responsibility of the operator on shift, the JCOP framework has developed a robust and coherent alarm handling structure. This alarm handling toolkit allows to implement different alarm typologies and complete them with additional information on the origin, severity level and relation with other alarm condition. There are two types of alarms which are proposed by the JCOP Framework. These are the simple boolean alarm (good value and alarm value) and analogue alarms for which we can define up to five ranges. The possible severity levels are: Warning,

Error, and Fatal. When the alarm condition requires particular attention from the operator an *Acknowledge* condition can be imposed, independently from the severity level. The operator is then forced to certify he or she took vision of the alarm for the alarm itself to disappear.

Alarms can be also summarized, through a *Summary Alarm*, to obtain a level of abstraction. A Summary Alarm can be defined for any group of alarms. When active, a Summary Alarm indicates that at least one of the alarms in that group is active. It can be used to provide an abstraction for higher levels in the controls hierarchy. Alternatively, a Summary Alarm could be used to group alarms across multiple branches of the hierarchy. For example, each sub-detector may have a LV system and one might wish to have a Summary Alarm that groups all LV alarms independent of the controls hierarchy. If more than one alarm in the group is active, the alarm with high severity is shown.

These tools have been used in the RPC DCS. In particular, alarm conditions have been set for the value of the current of the RPCs. Default alarms are set at the initialization of the system, while a custom user interface allows the operator to change these values as needed during runtime.

3.6.4 The Configuration and Condition Databases

The high number and heterogeneity of the RPC system subelements, make configuration and installation procedures particularly laborious. All the structural information of the subelements, their interconnection, installation and configuration information for hardware and software components are initially stored in the PVSS internal database and then stored in an external *Configuration Database*. This is done with the help of a friendly user interface provided by the framework. The information stored is divided in three main categories depending on its nature:

Static System Configuration Data contains the description of the system layout and of its subelements.

Device Static Configuration Data represents all non frequent changing parameter, like an address, archiving, and alarm configurations of the physical devices.

Device Dynamic Configuration Data holds frequently changing variables, such as values and alarm settings.

For the present control system, the Configuration DB has been used to store the structural layout of the hardware devices and their physical and logical addresses. In addition, the system configuration values for ON and STANDBY states have also been archived here.

The Configuration Data base photographs the system in its initial conditions. The eventual evolutions and possible variations from the starting

point are recorded in a different database, the Condition Database. This information is fundamental since changes in the detector configuration may affect the quality of the data taken. In general the Condition Database will hold all parameters for the run of the detector, its operational parameters, notes of eventual malfunctioning parts, the information inherent to alignment and calibration and environmental parameters. For what concerns the RPC DCS, all parameters relevant for the understanding the status of the high and low voltage system and the readout chamber temperatures are stored.

3.6.5 The Graphical User Interface

Particular attention has been put in the realization of the graphical user interface. The goal was to create an intuitive tool for the control and monitoring the detector, easily usable also by non-experts. The interface was developed using the GEDI editor provided in PVSS II. Information presented and the possible actions the operator may perform through the interface are defined by custom scripts of various nature. The programming language used is C with extensions. The graphical vest of the interface (the panels in PVSS language) offers the following functionalities:

- an easy navigation throughout the entire system structure, thanks to a combination of text, graphical objects and synoptic diagrams;
- visualization and setting of any process variable;
- global parameter setting, thus speeding operations and reducing human error in repetitive actions;
- plots, diagrams, and table for a quick visualization of the evolution of a parameter in time;
- complete visualization of the alarm condition on all critical elements.

The interfaces have been developed, at least at supervisor level, separately for endcap and barrel. This decision comes from the different geometry of the two systems. At device level, this distinction disappears. A concise yet complete description of the main panels that were realized for the endcap RPC DCS follows. Elements of the barrel region will be also presented.

The Top Node Panel

The *top node panel* (figure 3.20) was realized to give the operator a quick and complete view of the entire endcap system. The status of system is constantly visible in the top section of the panel, while the status of each disc, its children, is given on the left. By clicking on the status button of each element, the list of allowed actions is prompted in a cascade menu

form. It is also possible to modify the partitioning of the system, including or excluding various nodes. This feature was implemented following the template provided by the JCOP framework and has been repeated in all FSM panel.

The graphical aid on the right, which covers the majority of the panel, represents the forward RPC region with its eight discs. As it can be noticed, the disc configurations are subdivided in three rings. Status changes, in any or all rings, trigger changes in the color of the corresponding graphical element. The color code proposed by the JCOP team has been followed throughout the entire project. The led in the top right corner indicates the correct connection to the hardware. If the connection is lost the led turn red and a text message alerts the shifter. Finally, the disc interested in the *Magnet Test & Cosmic Challenge* is highlighted in magenta (see section 4 for further information).



Figure 3.20: Graphical interface for the endcap root node.

Moreover, through this panel the user has the possibility to configure alarm and archiving conditions for the whole system. Simply clicking the button “Set Global Alarm” the panel pops up. This interfaces allows to set the alarm severity levels and the displayed text for all high and low voltage channels. Default alarm conditions are automatically set through postinstall scripts, when the system is uploaded for the first time.

In an analogous way, the *archive panel* is called. Hence, the user can choose which parameters to archive and where (internal PVSS or external database) with few simple clicks. Also in this case, default archiving para-

meters are set by the postinstall script. The values of the monitored voltage and current, the status and on set voltages and currents for all channels are archived on the external RPC Conditions database.

The top node panel for the barrel supervisor tree is shown in figure 3.21. It follows the same criteria used in the realization of the endcap top node panel and offers the same level of information.

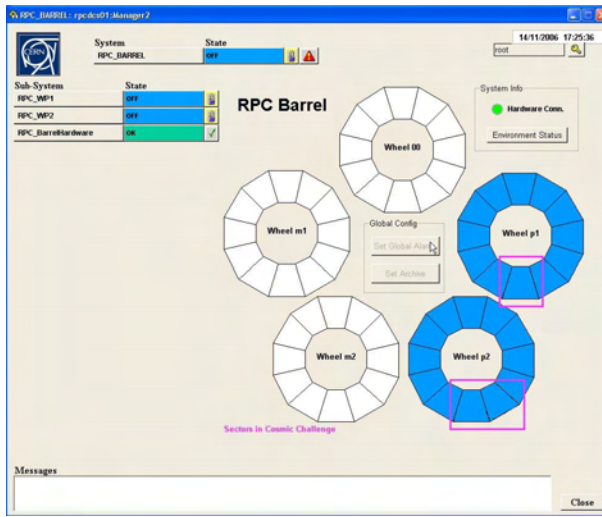


Figure 3.21: Graphical interface for the barrel root node.

The Disc Panel

Going downwards in the FMS tree, the second level is occupied by the **disc node**. The *disc panel* varies depending on the number of chambers; the one shown in figure 3.22 refers to YEP1 which has a total of 108 chambers. The disc slice active during the *Magnet Test & Cosmic Challenge*, as before, is highlighted in magenta (we send to chapter 4). The graphical representation of the disc is subdivided in chambers. The chambers are clickable objects. If an error or any problematic situation occurs in one or more chamber, the *chamber panels* can be accessed directly from this level.

The button “Disc Global Set” at the center of the disc, opens the “Global Configuration panel”. Through this interface the user may switch on/off and set the main parameters of all high voltage and low voltage channels of the disc with few clicks.

In the barrel supervisor FSM tree, this level corresponds to the *wheel panel*, presented in figure 3.23. The chambers are not clickable, but the panel is embellished by useful indicator of the active portion of the wheel.

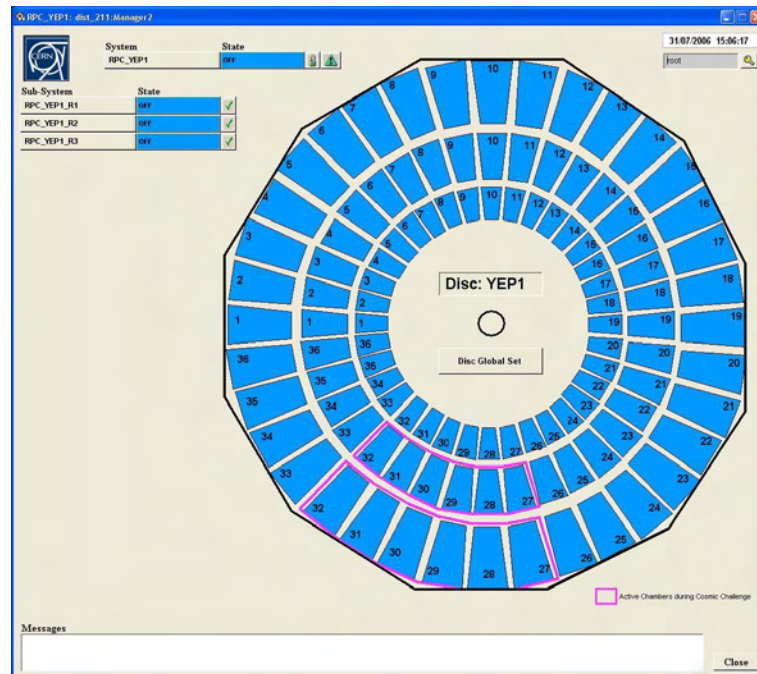


Figure 3.22: Disc node panel.

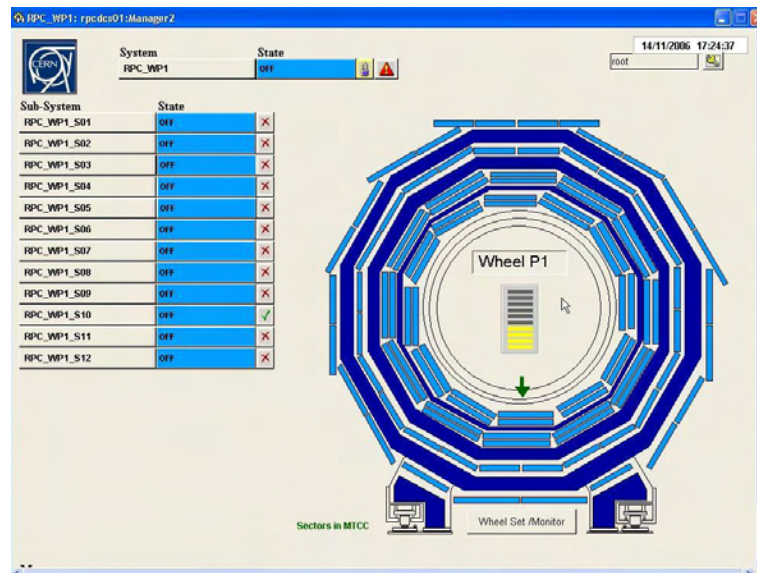


Figure 3.23: Panel for the wheel node.

The Ring Panel

Beneath the **Disc** we encounter the **Ring**, whose panel is given in figure 3.24. The solution here adopted is a concise, yet complete, information table. The logical name and the status of every channel is presented to the user in a single glimpse. The specific *channel panel* can be accessed clicking the *Details* column of the corresponding row. By using the framework Trending

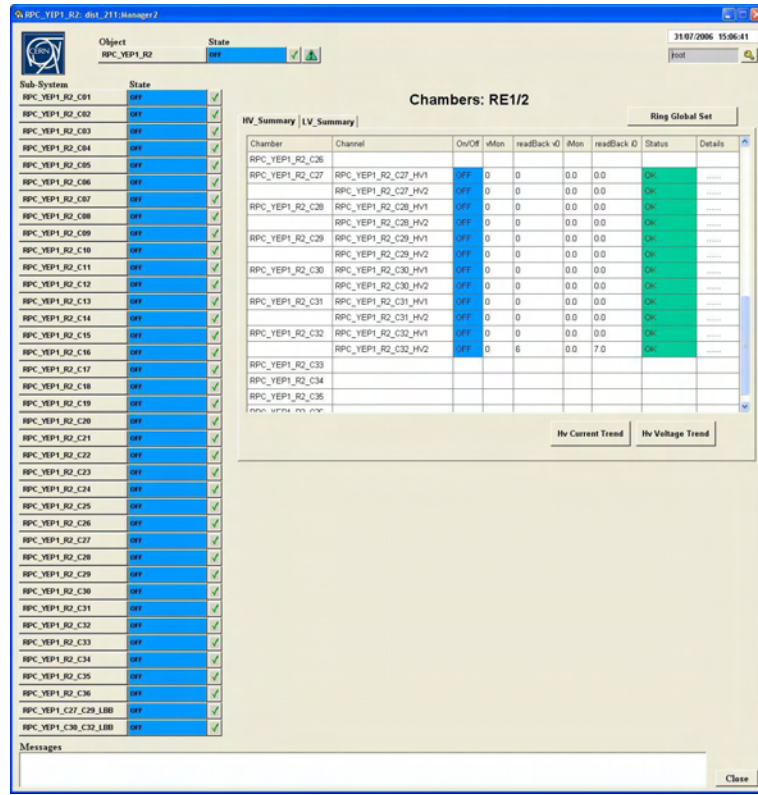


Figure 3.24: Ring node panel.

tool it was possible to design the panel in figure 3.25 and analogous panel to show the evolution of current and voltage in time. These panels are accessible through the “Current” and “Voltage Trend” buttons.

Also the corresponding barrel panel, the *sector panel*, offers the user a simple consultable table with the same information on high and low voltage channels.

The Chamber Panel

The last level of the supervisor FSM tree is the **Chamber**. The related panel (figure 3.26) offers a intuitive interface for the control and monitoring of each single chamber. The main functionalities are:

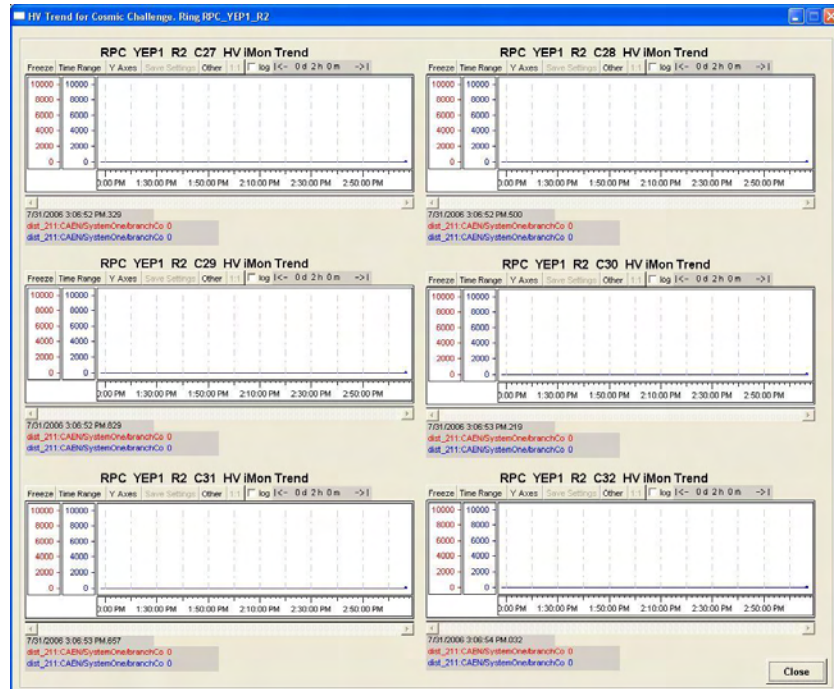


Figure 3.25: Current trend panel.

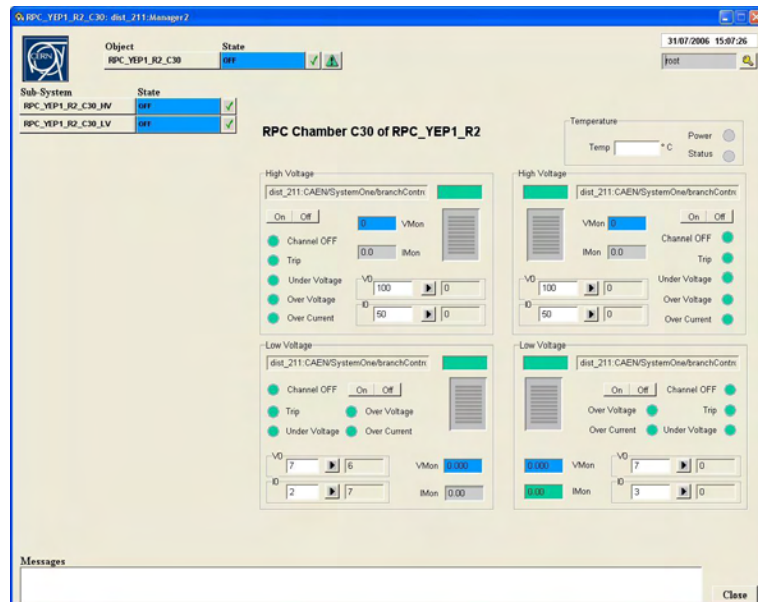


Figure 3.26: Chamber node panel.

- Recognize the device types and their specific characteristics. New devices can be easily integrated in the system.
- Allow a complete visualization of the alarm status. Boolean indicators are present for each individual channel and can be clicked to mask or unmask it.
- Buttons and text boxes allow to modify the operational parameters of each channel, switch them on or off and monitor their evolution.
- The temperature of the chamber is constantly monitored and displayed on the panel along with the status of the temperature sensors.

The temperature sensors are read out by CAEN ADC boards (A3801A) as described earlier. At the time of this thesis, these boards were not part of the CAEN framework component and, thus, not integrated in PVSS. Therefore, a custom component was developed. In fact, the possibility for a control system expert to develop his own device drivers is contemplated by the Core framework component, i.e. the fundamental framework package. The design of the device data structure, the device definition for the ADC board has been made as compatible as possible to the other CAEN board drivers and integrated in the control system. A copy has also been sent to the framework group for its insertion in following framework versions.

From this level on, there are no differences between barrel and endcap, at least for what concerns the graphical appearance of the interfaces. The differentiation between the systems is done in the code, invisible to the user. Hence, the operators will learn to interact with the tool more quickly.

The Device Panel

The devices are the leaf level of the hardware FSM tree and are connected to the supervisor FSM tree as references. Selecting a node or its reference, recalls the same panel. The panel proposed for the high and low voltage CAEN modules is shown in figure 3.27. The similarities of the two module types have used to find a common solution. The panel presents all the possible parameters that characterize the behavior of a channel. These parameters are divided in two groups, depending on their nature, read or write. The left part of the panel is clickable. The operator can change the setting of the channel following few intuitive steps. The right side of the panel displays all parameter necessary for the comprehension of the channel's behavior. An important aspect of the panel is the presence of a history plot that offers the course of the monitored voltage and current over a user specified period.

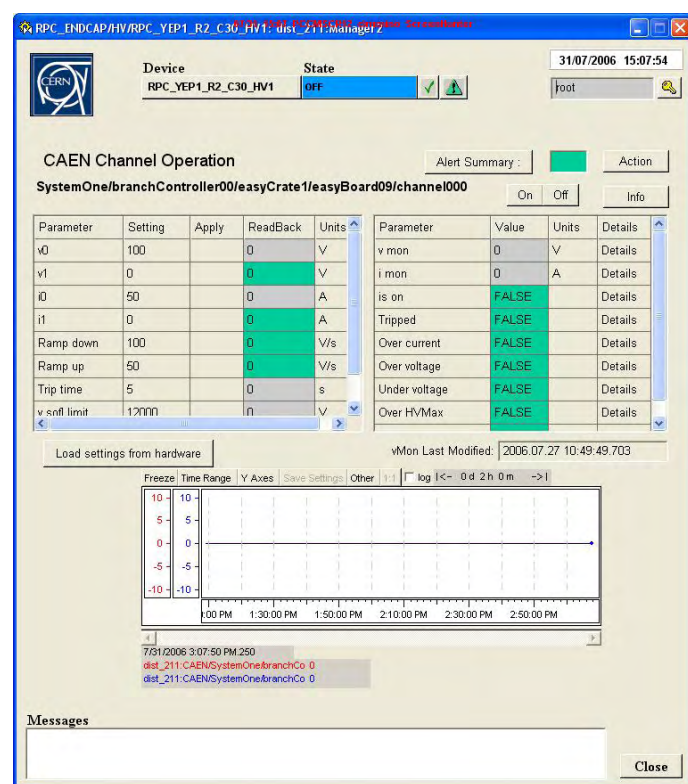


Figure 3.27: Developed panel for power supply channels.

3.6.6 Integration in the Central CMS DCS

After the development phase, a consistent effort has been put in the integration of the RPC DCS application in the central CMS DCS. This has been done over a three month period spent at CERN. The integration procedure, in fact, consisted of several steps. First of all, since the RPC system in CMS covers both regions of the detector, the DCS applications for the RPC barrel and endcaps, have been developed as two different project, capable of running standalone. This surely optimizes resources and allows a more detailed monitoring of the detector, but it contrasts with CMS specification [70]. The central DCS accepts only one child node per subdetector. Therefore, the two applications have been integrated to form a single system capable of operating as a whole, but also easily partitionable. Since this requirement was clear from the beginning, the architecture of the two systems was developed as coherent as possible. Hence, the developing effort was reduced and the blending was facilitated. Secondly, once the complete RPC DCS had been tested and proved functioning, it was integrated in the central DCS. The first step was to control if naming conventions had been respected. In fact, naming conventions are intrinsically necessary for communication. Using these conventions uniquely identifies applications, systems, FSM nodes, FSM types or files and creates a coherent DCS language.

Subsequently, the control application has been created in the form of a component. Components are software packages which include libraries of code, a set of graphical user interface panels, configuration data and, if they relate to a hardware device, the device definition is included as well. This format allows for it to be installed in any project already existing by means of the JCOP framework installation tool. Version tracking is also gained and applications can be moved from one project to another redistributing the load among the production systems. This component like system allows for easy installation of the controls, easy update while keeping track of changes made and allows also to bring back an application to an older working version if needed. A central and tidy installation is possible using this system. It ensures coherency (there are not several copies of same file) and maintainability (there is only one place to go to fix a bug) across the distributed system.

Finally, the system was connected to the common CMS Condition database, for data storing. This database has the advantage of being accessible to everybody from the network, at the webpage:

<http://cmsdaq.cern.ch/cmsmon/cmsdb/servlet/DatabaseBrowser>.

At the moment the RPC DCS has been divided in four components: Barrel Supervisor and Device components, Endcap Supervisor and Device component. The components have been equipped with installation scripts, that run at installation time. Through these scripts the system accesses the configuration database to retrieve the latest system configuration, sets

default alarms, creates the FSM structure, and connects to the condition database for data storing. All four components have been copied for storage in a central repository and installed on two dedicated DCS machines. The central DCS application, connects to the RPC DCS application by importing the RPC FSM top node as a reference child node (as shown in figure 3.28). The RPC FSM tree, therefore, is accessible and controllable from the central DCS. Standalone operation is always possible by simply partitioning.

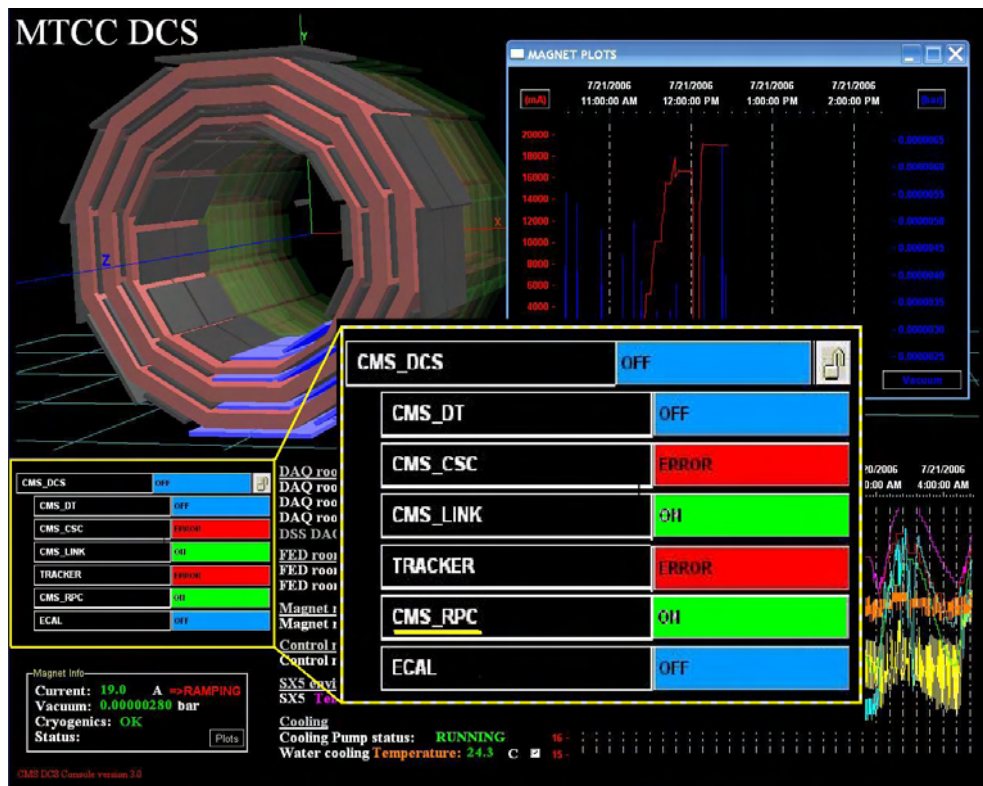


Figure 3.28: Central CMS DCS user interface.

The DCS application developed during this thesis work and described in the present chapter, has been used for the control and monitoring of the RPC system during the Magnet Test & Cosmic Challenge (MTCC) data taking. What is MTCC, its main objectives and a few preliminary results are presented in chapter 4.

Chapter 4

The MTCC: preliminary results

The CMS magnet system had to be tested before lowering. In addition, installation and commissioning of all subdetectors are being done in a surface hall. This brought the CMS Commissioning Task Force to propose, in the late 2004, the testing of all subdetectors as a collective system in the presence of B field. That is, to make use of the magnet test to check key installation and maintenance strategies and to demonstrate the operation of a slice of CMS with a cosmic trigger. This is how the Magnet Test & Cosmic Challenge (MTCC) first appeared. The main objectives of the MTCC are given in section 4.1. The subdetectors layout is presented in section 4.2.

The MTCC proved to be an incredible opportunity also for testing the reliability and robustness of the RPC DCS (see chapter 3). In fact, the control system was used throughout the entire Cosmic Challenge, for the control and monitoring of 35 RPC detectors. The data collected was stored in the common CMS Condition database, and retrieved with a custom tool developed as the concluding part of this thesis. Some results on the data, collected with the RPC DCS by me developed, are proposed in section 4.5, while preliminary chamber data is shown in section 4.6.

4.1 Main objectives

The MTCC main objectives are:

1. Test and commissioning of the magnet, including cooling, power supply and control system.
2. Map the magnetic field.
3. Check closure tolerances, movement under field and the muon alignment system.

4. Check field tolerance of yoke mounted components.
5. Check installation and cabling of : ECAL/HCAL/Tracker inside coil.
6. Measure the effect of the fringe field on muon chamber performances and on electronics.
7. Test combined subdetectors in a slice of CMS with magnet, using as near as possible final readout and auxiliary systems.
8. Check noise and inter-operability.
9. Test muon alignment systems.
10. Trigger and record cosmics.
11. Test the DCS system.

The test of the DCS system can be split in the following main goals:

- Integrate all DCS systems developed by the subsystems (Tracker, ECAL, HCAL, CSC, DT, RPC, Gas, Cooling) in the Central CMS DCS.
- Test Central CMS DCS during data taking; looking and studying in details the panels, alarms and logfiles generated by the singles subsystems.
- Test how the Run Control is able to communicate with the DCS.
- Test DCS configuration setup and how the DCS can handle the configuration database.
- Test the final state machines of every subsystem.
- Test how the DCS writes/readback data from the Condition database (where DCS data are stored).
- Analyze the DCS data to understand detector operation and to test the DCS system itself.
- Begin to write documentation and manuals for people in shift.

The accomplishment of all these goals was subdivided in two phases: MTCC Phase I, where magnet commissioning was done and all subdetectors were operated; MTCC Phase II, focused on magnet field mapping, without the Tracker and the ECAL. Removal of these two subdetectors was, in fact, necessary to place the field mapper inside the coil. Phase I officially started at the beginning of August 2006, but much effort was spent for its preparation in previous months. All was done without retarding the schedule for CMS completion. The first phase ended on the 28th of that same month and

was a great success for the collaboration. MTCC II started only on the 9th of October and was terminated on the 31st. The cosmic shutdown period in between was used to open the detector, remove ECAL and Tracker, and place the field mapper (FM). The mapper consisted of two rotor arms, 2 meters in length, each equipped with 5 Hall probe¹ assemblies. The Hall probes measured the field components in the longitudinal, radial and azimuthal coordinate. The mapper was mounted on two precision rails laid on the floor of the HCAL barrel unit, in the z direction.

4.2 Subdetectors in MTCC

In 2004, when the MTCC was first proposed, the goal was to see a curving muon track in all subsystems: something like figure 4.1 a. Finally in August 2006, the event number 3981 was recorded (figure 4.1 b).

All subdetectors have participated to the MTCC, covering different sections off both regions (barrel and forward), to exploit both barrel and endcap muon triggers. We give a short description of the various subdetector elements present:

- The **Tracker** [71] participated with 133 silicon strip modules, equivalent to 1% of its final layout. The setup for the MTCC comprises segments of the Tracker Inner Barrel (TIB), the Tracker Outer Barrel (TOB) and Tracker Endcaps (TEC) detectors. All pieces have been transported inside the dummy tracker support tube to the CMS experimental hall.
- The **ECAL** [72] turned on two supermodules over a total of 36. The modules roughly correspond to $\frac{\pi}{2} < \phi < \frac{11}{18}\pi$, i.e. a 20 degree coverage in ϕ .
- The **HCAL** [73] active sections in the barrel where sectors 6 through 8, which correspond to $\frac{\pi}{2} < \phi < \frac{5}{6}\pi$ and sectors 14 to 17, that cover the interval $1\frac{7}{18}\pi < \phi < 1\frac{5}{6}\pi$. The outer hadronic calorimeter (HO) participated with sectors 3, 4, 10 and 11, i.e. $\frac{\pi}{4} < \phi < \frac{7}{12}\pi$ and $1\frac{5}{12}\pi < \phi < 1\frac{9}{12}\pi$, distributed on the wheels W0², WP1, and WP2. Also sections of the endcap HCAL (HE) have been tested, in particular sectors 14 through 17, that match the sectors in the barrel region.
- The **Muon system** participated with all three chamber types. The CSCs [74] have configured a 60 degree slice of the inner three discs of

¹A Hall probe is a semiconductor based detector for measuring the strength of a magnetic field. A current is passed through the semiconductor which, when placed in a magnetic field, experiences a voltage drop across it. This is known as the Hall Effect.

²The CMS barrel is divided in 5 wheels, one at the center (W0), two on the plus side (WP1, WP2), which is closest to the Jura mountains, and two on the minus side (WM1, WM2).

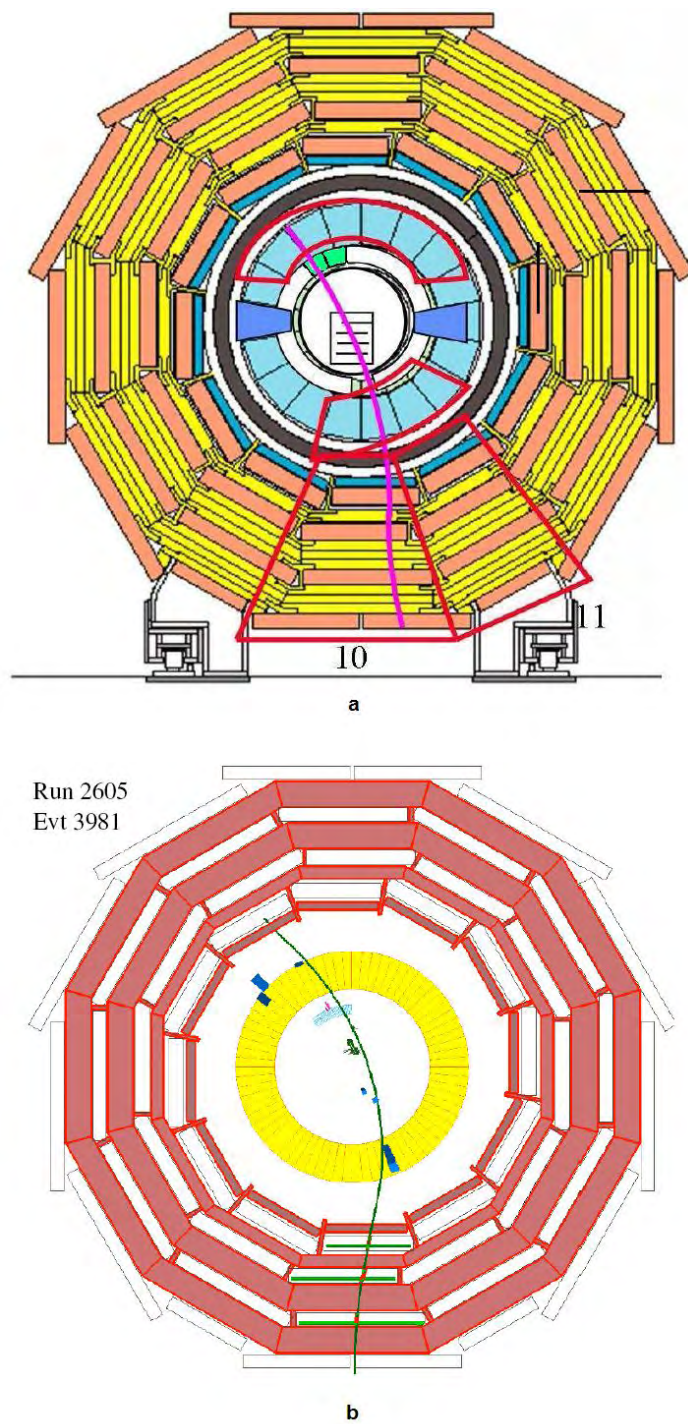


Figure 4.1: The goal of the MTCC was to see a curving muon track (purple line) in all subdetectors.

the plus side of the detector. In the coordinate ϕ , these 36 chambers correspond to $[1\frac{5}{12}\pi, 1\frac{9}{12}\pi]$. The DTs [75] and RPCs [76] had three fully operational sectors; sector 10 in WP1 and sectors 10 and 11 in WP2 ($1\frac{5}{12}\pi < \phi < 1\frac{9}{12}\pi$). The RPCs had active chambers also on the innermost endcap disc. These chambers in the forward region, 12 in total, correspond to sectors 10 and 11 of the barrel.

The infrastructures used were as close as possible to the final ones. These count the closing system, racks, power distribution, alignment, trigger, DCS, DSS, DAQ (pre-series), DQM, databases, network, data storage, data transfer, gas, and cooling. Obviously, everything was scaled to the “limited” dimensions of the experiment. In truth, the DSS was required in its complete functionalities to provide the safety of the system, even if temporary. Despite good efforts, a few dedicated MTCC elements were necessary: the Tracker needed a 1:1 scale dummy tube, cabling for barrel ECAL and Tracker was designed for the occasion, and a local trigger controller card was used in place of the global one.

4.3 MTCC Phase I and Phase II

The MTCC Phase I [77] lasted almost a month. A total of 50 million events were recorded over the whole period, both with $B = 0$ T and $B = 3.8$ T. 25 million events were labeled “good events”, that is with at least DT trigger and both ECAL and HCAL readouts (see figure 4.2). During the data taking, all subdetectors were included in the readout and trigger. Nevertheless, each subsystem identified a program of standalone hardware, local DAQ and self-triggered tests in addition to the period of combined operation. A fraction of a few thousand events were recorded in all 4 CMS subsystems. The first event to fulfill this benchmark is exactly the one shown in figure 4.1 b. The total event size is about 200 kByte, dominated by ECAL and HCAL, that did not have zero suppression in readout. These numbers, even if far from what the final system will produce, placed great stress on the Storing Manager of the CMS software (CMSSW). The performance achieved a peak output bandwidth of $\sim 40MB/s$ and a sustained bandwidth of $\sim 30MB/s$. The typical trigger rate was of ~ 200 Hz. Data taking was done at up to 90% efficiency.

The MTCC Phase II [78] started in the second week of October 2006, after the removal of the Tracker and ECAL. The main objective was to map the magnetic field. There was a warmup period at 2 T that lasted 38 hours. The full volume was scanned with a measurement reproducibility of a few Gauss (1 Tesla = 10,000 Guass). The next step was to measure the field map at 3.0, 3.5, 3.8 and 4.0 T, thus easing precise interpolation to actual operating currents. The magnet had already proved to reach 4.0 T during

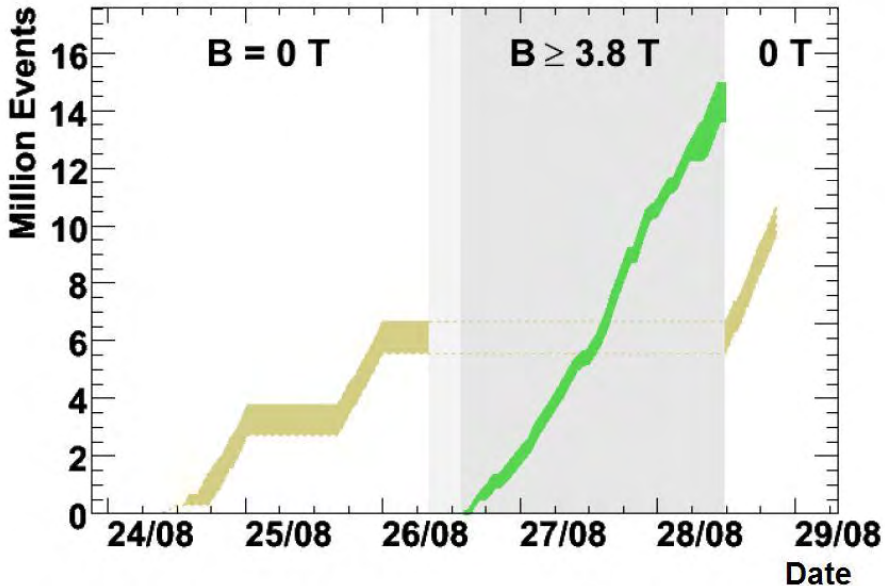


Figure 4.2: Events recorded during MTCC Phase I at $B = 0\text{ T}$ ($\sim 10\text{M}$) and $B = 3.8\text{ T}$ ($\sim 15\text{M}$).

Phase I, but in that case it stayed at nominal value (corresponding to 19 kA) for two hours only. This second time, to allow the complete mapping procedures, the magnet was kept at 4.0 T for two days.

During Phase II, the data taking continued with the muon detectors and the HCAL in order to study detector performances. About 250 million events were recorded. They were used for calibration, alignment and efficiency tests. Unfortunately, since Phase II was completed during the finishing period of this thesis, the available data is limited and preliminary (needs still a bit of understanding). This is also true for the field mapping information. Moreover, it was decided to analyze Phase II data only after heavy lowering started.

The MTCC was defined a “cosmic success”. It proved CMS can be opened and closed on intended timescales, the magnet can be work safely at 4.0 T, the subdetectors can be integrated with central DAQ, trigger, DCS, DSS, DQM, etc., commissioning strategies generally worked, and it can operate as a unified system (both humans and machines). All problems came from expected sources: stray field, difficulties in cabling, limited infrastructures, power distribution failures, insufficient cooling, human errors, faulty alarm signals, difficulties with detector readout commissioning, and an over crowded control room. Nevertheless, it was nothing as the final system. Compared to CMS, the MTCC was a factor 10 to 100 smaller in terms of

components (only 4% of the RPC system operated), the trigger rate was 100 times lower, only 25% of the software capacity was needed and the many systems were not centralized. But at the end, MTCC was an excellent exercise, to test everyone's capabilities, individually and as a team. All problems encountered have been solved or are under investigation; hence they are out of the way of the startup run in 2007.

4.4 The RPC DCS in the MTCC

As already discussed, the DCS is an indispensable element for the operation of a modern detector. The need for a fully operational DCS was present even during the MTCC, where only subsets of the subdetectors where active. This proved to be a once in a life time opportunity to test the RPC DCS hardware and software parts (extensively described in chapter 3). In fact, the control system was used to control and monitor all RPC chambers active during the cosmic challenge. The DCS was installed on two dedicated rack mounted PCs in the control room (Green Barrack) and integrated with the central DCS. The system was optimized for the RPC MTCC layout and the user interfaces were adjusted for the occasion. An *ad hoc* FSM devices tree was structured, scaled to the limited dimensions of the apparatus. The hardware configuration and setups, as well as the logical mapping of the electronics were stored in a development Configuration database. Referring to figure 4.3, there were 23 chambers in the barrel region - each with 1 HV channel, 2 LV channels and 1 temperature sensor on almost every channel - and 12 chambers on one endcap disc - with 2 HV channels and 2 LV channels shared by adjacent chambers. For the HV and LV channels, all main parameters were archived in the common CMS Condition database to ensure the quality of the data. A list of such parameters and their archiving criteria are given in table 4.1.

Parameter	Archiving criteria
Monitored Voltage	deadband of: 15 V for HV 0.2 V for LV
Monitored Current	deadband of: 0.3 μ A
Voltage Setting	at change
Current Setting	at change
Channel Status	at change
Temperature	deadband of: 0.3 °C for MTCC I 0.2 °C for MTCC II

Table 4.1: Archived parameter using the RPC DCS and their archiving criteria.

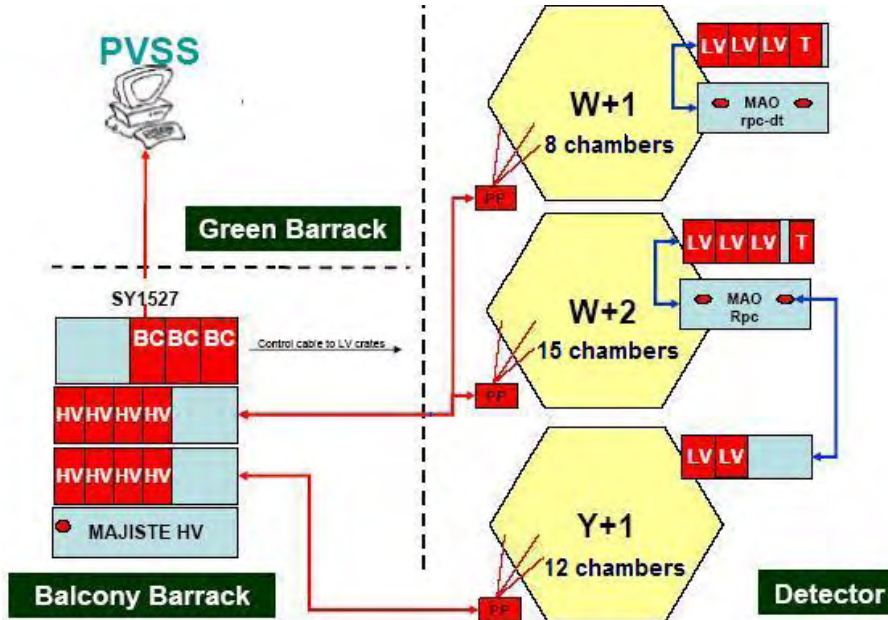


Figure 4.3: Schematic layout of the HV and LV system for RPC during the MTCC.

The LV boards and the ADC boards needed for the temperature sensors, were collocated directly on the detector, while the high voltage module were placed in a nearby room (“balcony barrack”) along with the mainframe.

The DCS was turned on few days before the official start of the MTCC. All connection, hardware and software, were checked. The system, after a short debug phase, ran without problems for the entire test period. The only interruptions were due to power failures and communication problem with the mainframe, for which the fridge field is thought responsible. The DCS proved to be robust, reliable, and, most important, user friendly.

The MTCC was also the first time in which the RPC group organized a set of daily shifts (3 per day) with non DCS experts. The shifters were called upon to use the DCS and Run Control to operated the detectors and take data. The test was very important for the DCS, for it is the interface between the detectors, the shifters or the physicist interested in detector data analysis. All people involved were trained by the DCS experts on the use of the systems: how to take data and check the detector operation. The RPC DCS was used by a lot of people and it resulted a friendly detector interface. The main complication were related to the database interface. That part was completely automated and did not give problems. The graphical user interface (GUI) and the Final State Machine were used extensively, showing to be robust and stable. Nevertheless, some improvements have to be made

for the final phase when the 34 chambers of the MTCC will become more than 1000.

Once the MTCC stared, the data flowed copious and were stored in the Condition database. A custom tool for its retrieval and realtime analysis was developed and tested in the DCS framework, to give the possibility to check online the performance of any RPC or RPC subsystem.

4.5 Results of DCS data

The last part of this thesis was the development of a software application to analyze the DCS data of the MTCC and a preliminary data analysis. The aim of the application was to study the behaviors of the 23 RPC barrel chambers producing also some overview plots and statistical results able to identify some "unusual" functioning of the chamber. In the next future this application will be integrated in the so called Data Quality Monitor. The application has been written in ROOT and the programming language used was C++. The data analysis can be divided in the following steps:

1. retrieve RPC data from the CMS Condition database (Oracle DB) using a set of SQL³ queries.
2. produce a series of root files, containing all the info needed for the analysis.
3. analyze the data producing plots and statistical results.

The first step was accomplished using C++ libraries, that allow to access and interface to an Oracle DB. The routine was based on a set of queries able to select data of a specific chamber and/or from a specific time interval and/or under specific cuts on different parameters. The output of the selection was a root file per operational parameter (monitored current, voltage, temperature, etc.) containing information on the chamber, time stamp, and value. The root files can be easily correlated in order to produce summary plots and statistical results. A problem encountered in the correlation, was the synchronization of the DB data. In fact, information from different chambers and from different parameters of a same chamber are not time related. This is due to the fact that the DCS writes data in the DB in an asynchronous way: in our case when the "last" monitored value differs from the previous by more than a specified bandwidth. In this way, the amount of data written in the DB, compared to the a synchronous readout, is significantly reduced, but needs a software for *a posteriori* synchronization. The development of a routine to correlate all possible information was mandatory and has been developed using standard algorithms for searching

³Structured Query Language, or SQL, is the most popular computer language used to create, modify, retrieve and manipulate data from database management systems.

specific elements in an ordered vector.

The last part of my thesis work was focused on analyzing part of the MTCC data. The first step was to plot the monitored current and the temperature of every chamber during the full period to check data correctness and consistency. Examples for a specific chamber (RB2in wheel+2 sector 11) are given in figures 4.4 and 4.5. After that, a “particular” period, in which the Magnet, the cooling system, the gas system and the RPC detectors were stable was chosen, in order to analyze the performance of the RPCs without external interferences. The preliminary results are here described.

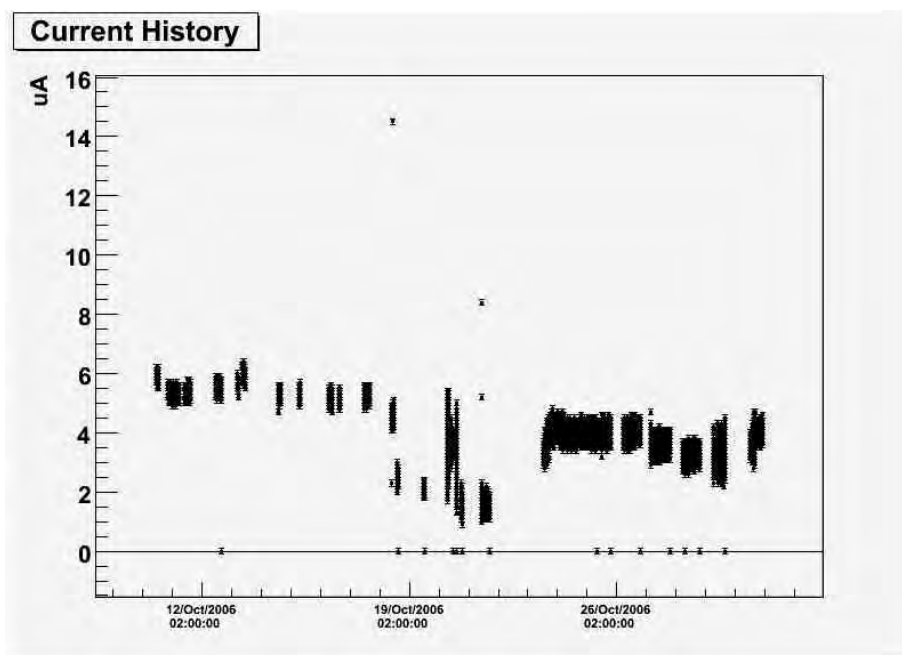


Figure 4.4: Current history plot for chamber RB2in wheel plus 2 sector 11. The current values were recorded during the MTCC Phase II and with the chamber at operation point (9200 V).

From the overall period plots, it is possible to individuate intervals in which the RPC system was not stable. The instabilities were due to a long sets of test made by the magnet, cooling, and gas groups. In any case, it was very interesting to see that the chamber temperature was stable in an interval of 4 degree Celsius. This shows us how more stable is the temperature in the iron even if the cooling system is not properly working. In fact, during the summer period and with the wheels open, we observed a differences in the chamber temperature up to 10°C. In addition, we recorded an increase of 7 °C in temperature going from the internal chambers (RB1) to the ex-

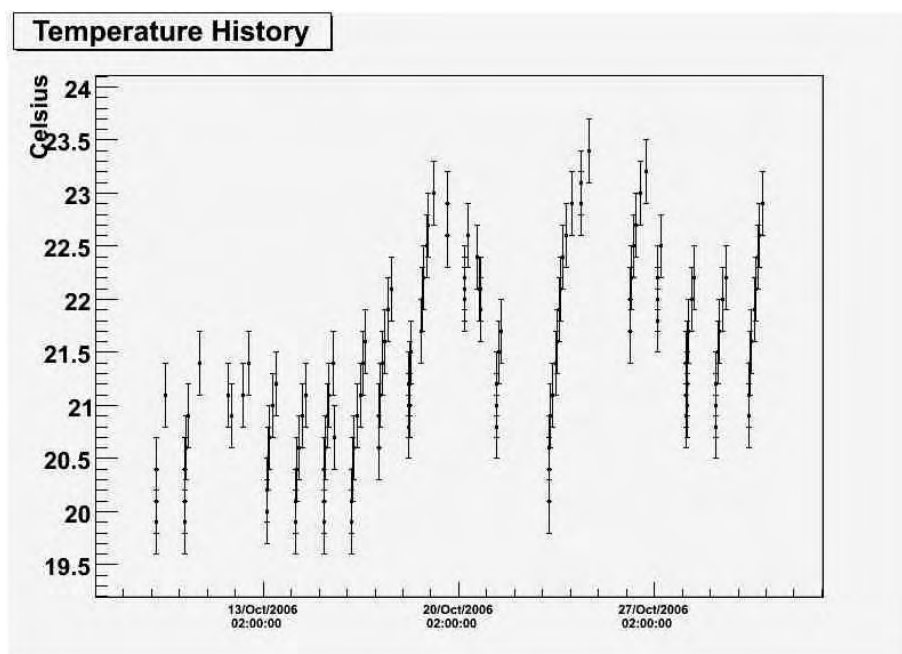


Figure 4.5: Temperature values recorded during the MTCC Phase II for the chamber RB2in wheel plus 2 sector 11.

ternal one (RB4) inside the same sector. These temperature discrepancies have been completely reduced once the wheels were closed and the cooling system for the electronics and iron was switched-on. It is also important to remember that all these test have been done at the ground level, while CMS will work 100 meters underground, where the ambient temperature is stable around 19-20 °C. As proof of what just stated, we attach the plot of the temperatures in the experimental whole. The values were registered by the central CMS DCS with a 0.2 °C deadband and accessed through the web. The plot clearly shows a ~ 8 °C maximum temperature excursion over the entire period, twice the value recorded for the chambers.

After checking and studying the non-stable periods on the CMS electronic logbook, we concentrated our attention on the so called “stable” period (24th to the 28th of October). During this time period, the DCS worked without any interruptions and the 23 barrel chambers were always at the nominal voltage of 9.2 kV. The first variable analyzed was the average temperature of each. The average temperatures of the 23 chambers are reported in figure 4.7. All chambers present an average temperatures between 21 °C and 24°C : values close to estimated ones and very stable along the 4 days. Only one chamber (W+2 - S10 - RB1out) has a mean temperature of about 19 °C. The nature of this discrepancy is actually under investigation to understand

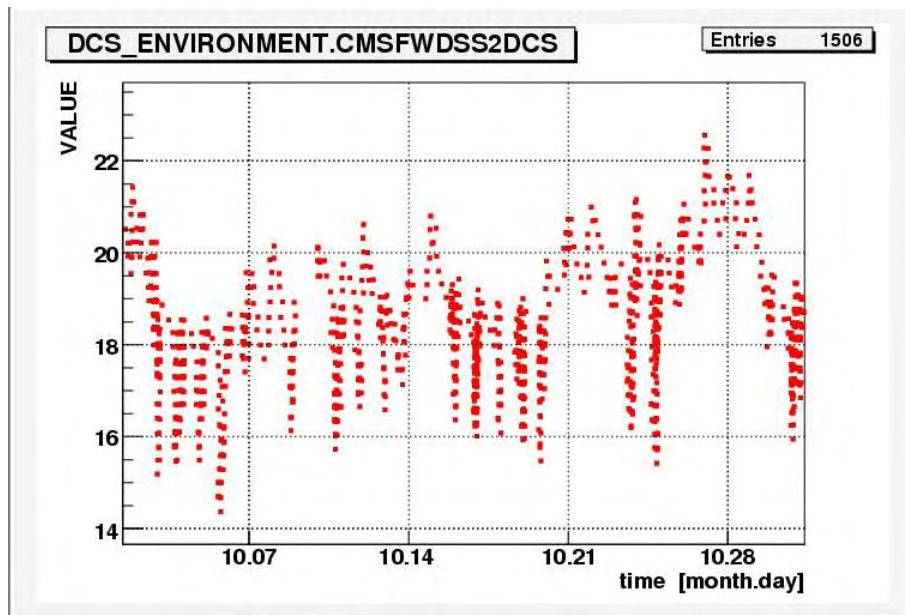


Figure 4.6: Experimental hall temperature values during the month of October.

if there is some problem in the cooling or if the sensor or ADC channel is not working properly.

Figure 4.8 shows the distribution of the average currents of all barrel RPCs over the stable period, after having subtracted the different offsets of the HV channels. The HV board A3512N has 6 independent channel. Every channel is equipped with a current monitoring stage based on an 16 bits ADC. The ADC reads the voltage on a fixed resistor with a resolution of 0.1 A on a range of 1 mA. Every monitoring stage can have an offset which differs up to 1 A channel per channel. The offsets are measured at every run with a dedicated calibration and are store in a database. All chambers (with 4 or 6 gaps) show an average current lower than $7 \mu\text{A}$, below the upper limit of $10 \mu\text{A}$ used for chamber acceptance during production tests performed in Italy and at CERN. The average current of the 23 chambers is $2.5 \mu\text{A}$ with a very narrow distribution ($\sigma = 1.3 \mu\text{A}$) although there is one chamber with current higher than $7 \mu\text{A}$.

Afterwards, I studied the current distribution of every chamber in the stable period to identify if there were “nervous” chambers. In figure 4.9 the current RMS distribution of every chamber is shown. This gives us an estimation of the instability of the current of a single chamber in this 4 days period. The calculated average RMS was $0.5 \mu\text{A}$, showing a very stable

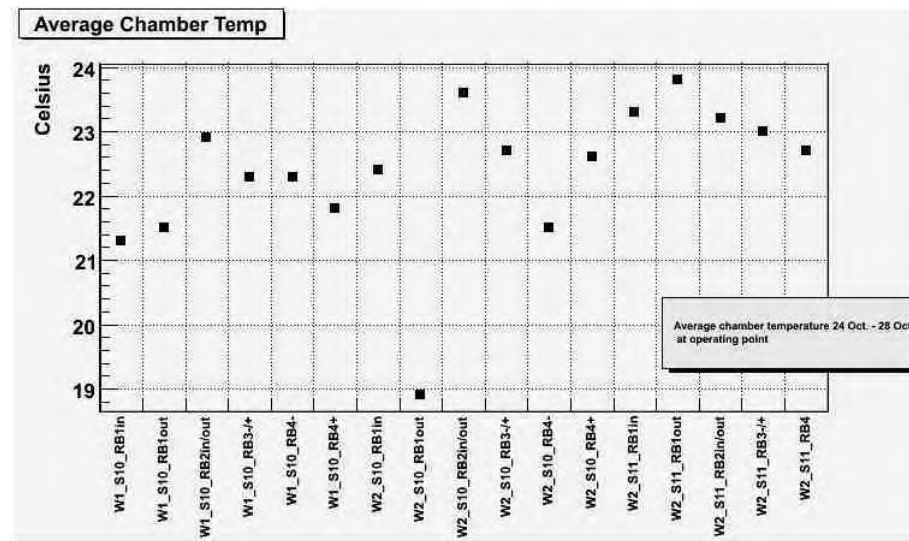


Figure 4.7: Average temperature for barrel chambers.

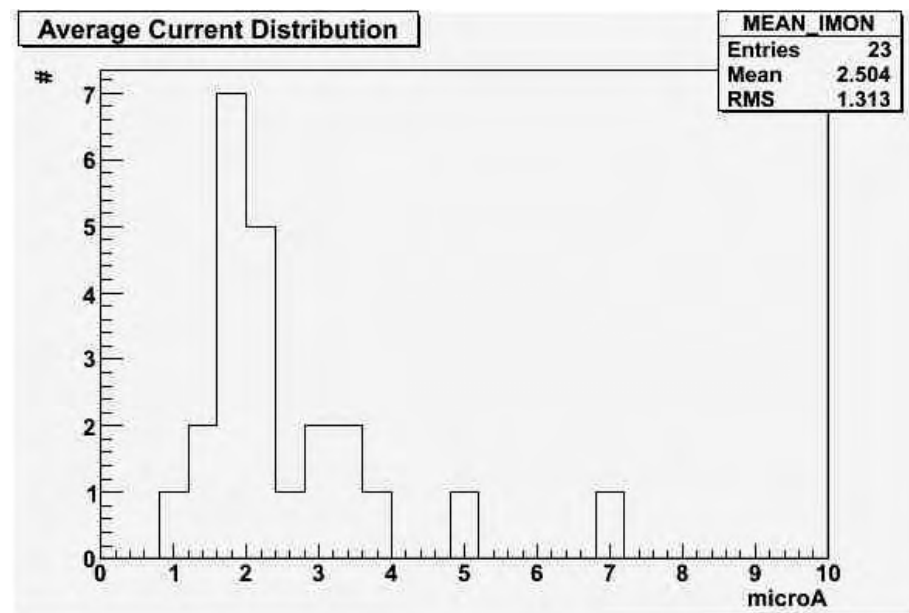


Figure 4.8: Average current distribution in the barrel. The period analyzed is 24/10/2006 - 28/10/2006. The value were corrected for channel offsets.

behaviour of the chambers in a long period test and in a configuration very close to the final one. 22 chambers have an RMS lower than $0.7 \mu\text{A}$. Only one chamber has $\text{RMS} = 1.0 \mu\text{A}$. This chamber is under study to figure out if the difference was intrinsic or due to some malfunctioning of the HV connector/cable. Using only these two distributions it was possible to identify a chamber with a “unusual” behaviour showing us how crucial it is to develop online tools able to analyze the DCS data. Then, the shifter can react promptly by using the DCS control panels or calling an expert.

To conclude, the correlation between RPC current and temperature

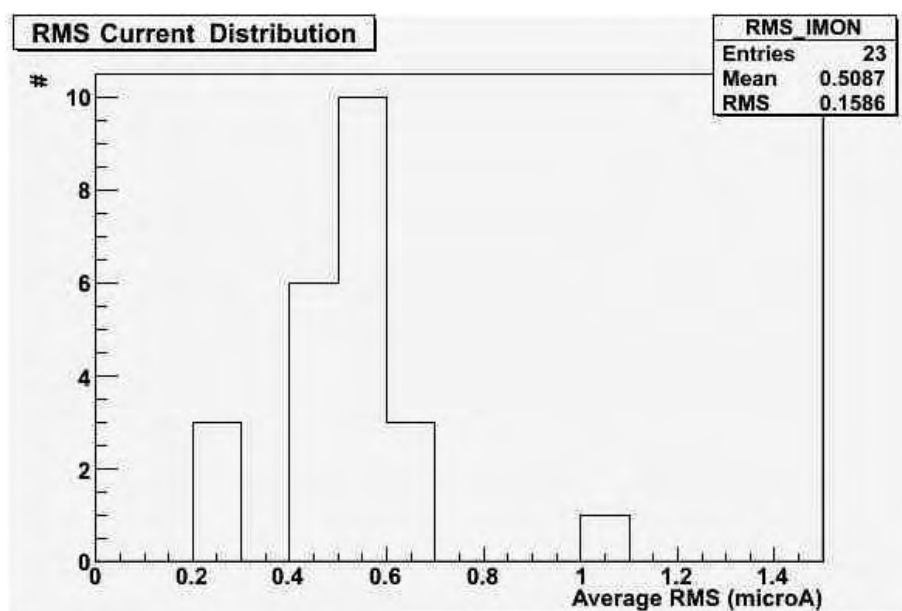


Figure 4.9: Average current RMS (i.e. standard deviation) distribution in the barrel. The period analyzed is 24/10/2006 - 28/10/2006.

was analyzed. These two parameters, as explained in chapter 2, are strictly related. To accomplish this analysis, a second *stable* period, i.e. 23/10/2006 - 24/10/2006, was chosen. This time interval was characterized by an evident temperature rise due to malfunctioning of the cooling system. Figure 4.10 shows the correlation between temperature and drawn current for a particular chamber in the barrel region. As expected the current increases with temperature. Experimental data shows that to a temperature rise of about 0.8°C corresponds an increase in current from $3.2 \mu\text{A}$ to $4.5 \mu\text{A}$, that is about 40%.

These preliminary results have been presented during two CMS meetings at CERN and were a very important proof of how well the RPC system

operated during the whole MTCC.

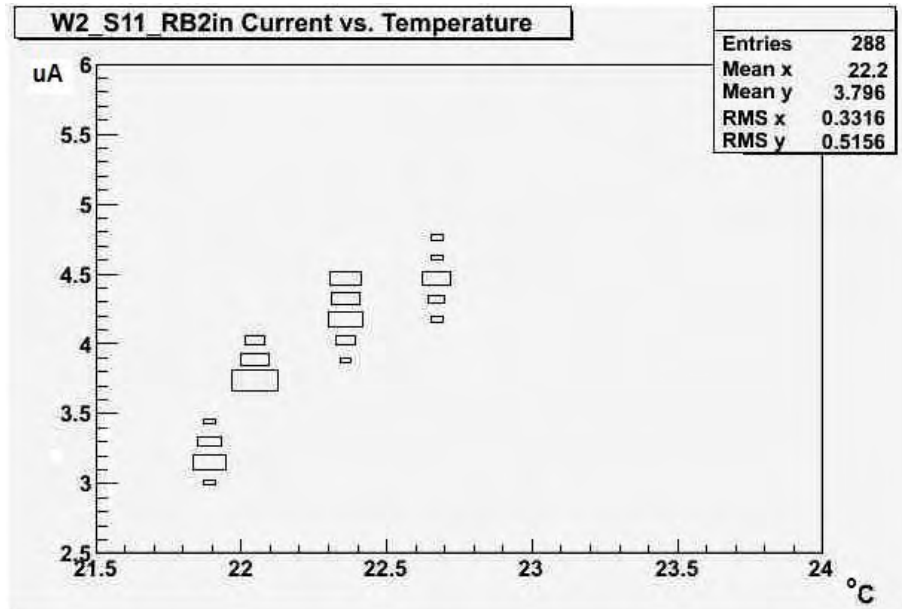


Figure 4.10: Correlation between temperature and current for chamber RB2in wheel+2 sector 11 (23/10/2006 - 24/10/2006).

4.6 Results of chamber data

To prove that the whole RPC system worked well during the MTCC, an analysis of the RPC trigger and muon system, together with DCS data, was performed. The DCS data were acquired with the control system developed during this thesis. RPC detector and trigger performances have been evaluated using cosmic muons detected by CMS [48]. The goal of this preliminary analysis was to characterize the chambers by their efficiency, detector noise and cluster size. The cosmic muons used for this analysis were triggered and reconstructed using only DT chambers. The muon tracks, therefore, were completely independent from the RPC detectors, which we want to analyze. For every reconstructed muon track, the interaction point on the RPC chambers was extrapolated to determine the presumed impact point. Afterwards, the RPC data were analyzed to see if there was one or more RPC hits corresponding to the estimated impact point and if there was an eventual RPC trigger. In this way, it was possible to measure the following performance parameters:

- RPC trigger efficiency was measured by counting how many DT triggered muons had also been triggered by RPC. Knowing the RPC im-

pact points (therefore the chambers are involve), the trigger efficiency was also be studied as function of the wheel and of the sector or angular regions.

- RPC detection efficiency was measured counting how many selected muons have been detected by the RPC chambers present along the track. It is very important to extrapolate the RPC impact point with a spatial resolution of a millimeter in order to study very well the dead zones of every chamber.
- Noise rate was measured counting the average number of hit outside the trigger window and normalized to the chamber surface.
- Cluster size, defined as the number of contiguous strip fired when the RPC is hit by a single muon track, was measured.

The detection efficiency of a single chamber (RB1out wheel plus 2 sector 10) as function of the high voltage working point (efficiency plateaux) is shown in figure 4.11. The efficiency goes from 20% to 80% in about 400 V. At about 9600 V, the high voltage plateaux begins with an efficiency of about 98%. The same encouraging results have been found for the other barrel and endcap chambers. These very preliminary results will be studied in detail in the months following the end of this thesis. Thanks to the very high statistic of cosmic muons, the goal is to obtain a detailed map of the chamber efficiency with a definition of a couple of cm^2 .

The noise rate distributions at different value of B field are shown in figure 4.12. In CMS, this very important parameter must be less than 50 Hz/cm^2 to avoid fake trigger signals, as we have discussed in section 2.6. The noise rate distribution for the MTCC presents an average value well below 0.1 Hz/cm^2 . That is a factor 50 less than what measured during the acceptance tests performed in Italy. These preliminary results are under investigation but a large reduction of the noise was expected. New LV and HV (very low ripple) were used and an improved grounding schema was designed for the final system.

The cluster size, i.e. the number of contiguous fired strip inside a trigger window, is a way to understand the discharge size and the electrical insulation of the strips. An excessive cluster size could result in faulty muon track reconstruction. Extensive tests made in Italy and at CERN, during the chamber production, showed a typical cluster size < 3 strips. An average cluster size of 1.7 has been found at 9600 volts as shown in figure 4.13 confirming the good results of the RPC system during the MTCC.

In conclusion, the MTCC was a success for the whole CMS experiment. In particular, the RPC system (barrel and endcap) operated efficiently, triggering cosmic muons and showing encouraging results. The later confirmed

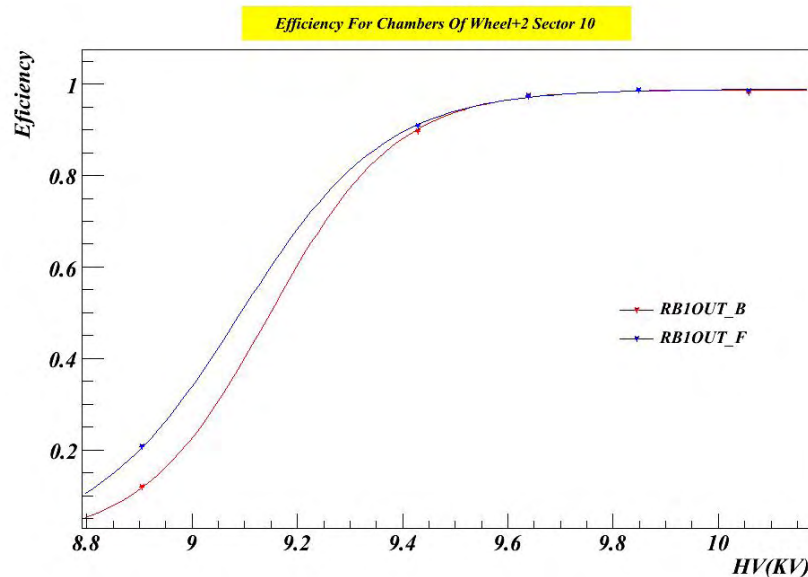


Figure 4.11: Efficiency for a particular RPC chamber.

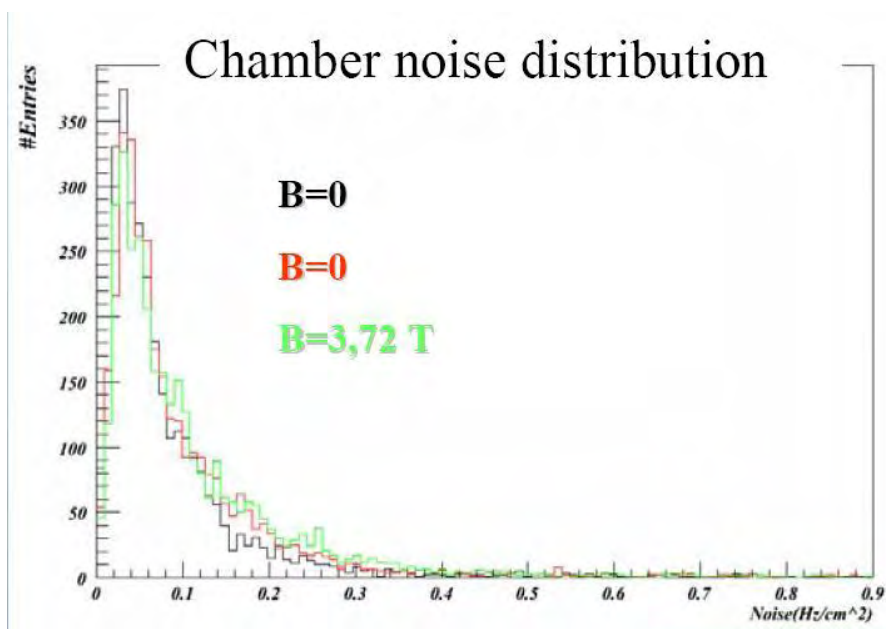


Figure 4.12: Distribution for chamber noise rate measured during the MTCC.

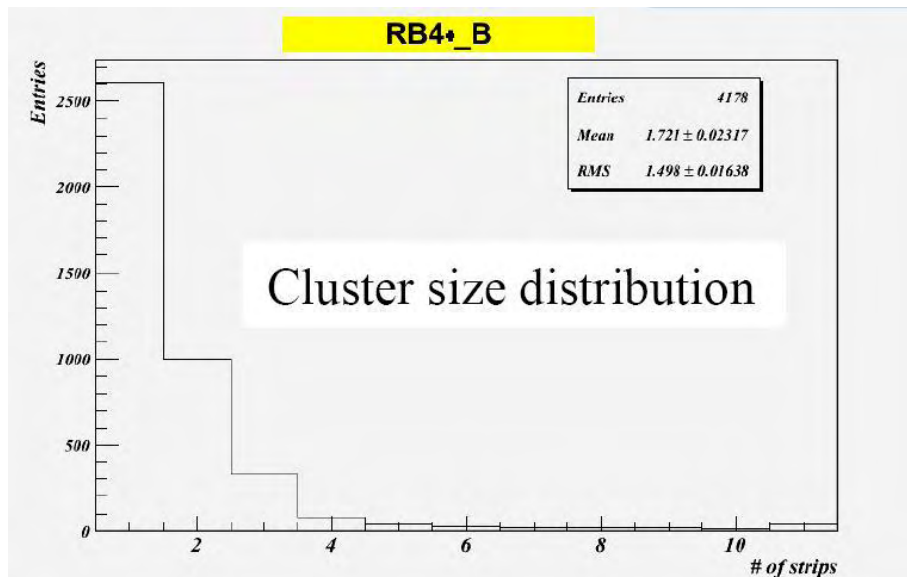


Figure 4.13: Cluster size distribution for the MTCC.

results obtained in earlier tests performed in Italy and at CERN (see section 2.7). The whole RPC collaboration received a great boost to continue installation and commissioning of the remaining chambers. We can reliably say that the RPC system will be ready for collision data in October 2007, for the LHC startup.

Conclusions

This thesis is focused on the design and development of the RPC DCS for the CMS experiment and on the first cosmic data taking made in summer 2006. The thesis has been developed in collaboration with the INFN group of Naples, the CMS DCS group and with the JCOP CERN group. After a careful analysis of the subcomponents and finalities of CMS, the attention has been moved on the characterization of the RPC chambers. Their key role for the muon trigger has been stressed. As a consequence of the complexity and importance of the experimental apparatus, the necessity to develop an online control system to ensure the detector stability and data quality was underlined.

The RPC DCS system was developed following the requirements of the RPC group and of the CMS DCS group and a first working prototype was delivered for the Magnet Test and Cosmic Challenge (MTCC). The main goal of my thesis was the design and development of the RPC DCS of the endcap region. During my thesis period I had the opportunity to follow three software courses (PVSS 1 and 2 and Final State Machine) and learn modern hardware and software technologies used in detector control systems. Part of my thesis work was developed at CERN, in collaboration with the central DCS group, in order to speedup the learning phase and the integration in the CMS experiment. Thanks to intense collaboration with CERN groups, I was able to implement the endcap DCS part in a uniform way, following all the CMS guidelines; the integration of the RPC DCS in the central DCS system was straightforward. After having carefully tested the DCS using a complete hardware setup, I have presented my work to the CMS Collaboration with a specific talk. Following some improvements and modifications suggested by RPC experts, the project was officially approved by the CMS DCS working group. Then, it was integrated with the RPC barrel project in the CMS DCS central system and it was tested in collaboration with the other subdetectors.

The concomitance of the MTCC with this thesis proved to be an incredible opportunity. It was the first real test of CMS and of the DAQ. I had the unique possibility to participate to the first CMS data taking, using all the software developed by the Naples group and myself. The RPC DCS system was used by ~ 100 people of the CMS Collaboration during shifts

of cosmic challenge data taking. It proved to be reliable, robust and user friendly, as shifters quickly grow accustomed to it. The RPC Final State Machine adequately followed the detectors behavior and never lost control of the hardware. Data taken by the RPC DCS system were analyzed and monitored in real time, producing a set of tables, plots and results. At the same time the data were stored in the official CMS database, ready to be used in online and offline analysis. In the last part of my thesis I developed a software tool capable of retrieving DCS data from the database and analyzing them. This tool proved to be a powerful way to monitor the correct operation of the chambers, giving important information on eventual malfunctioning of the detectors. Preliminary results on RPC performances, obtained using cosmic muons during the MTCC, were presented in the concluding paragraphs.

Acknowledgments

First of all, I wish to thank my supervisors, Prof. Crisostomo Sciacca and Dr. Pierluigi Paolucci, for their constant support and for all they taught me. I am also much indebted to Dr. Giovanni Polese, for the fruitful collaboration in the development of the RPC detector control system and for all the stimulating conversations. It was a pleasure to work with all the members and friends of the RPC Collaboration, the CERN JCOP group, and the CMS DCS group. Special thanks go to the INFN Naples Group, particularly to Dr. Davide Piccolo, Dr. Luca Lista and Dr. Francesco Fabozzi, always available to answer any question. Finally, I want to thank my family and all my friends, whose kindness and love were invaluable for me.

Bibliography

- [1] C. Quigg, *Gauge Theories of the Strong, Weak and Electromagnetic Interactions*, Benjamin-Cummings, Reading (1983).
- [2] I. Aitchison and A. Hey, *Gauge Theories in Particle Physics*, Institute of Physics Publishing, 2004.
- [3] S. Weinberg, Phys. Rev. Lett. **36** (1976) 294.
- [4] T. Hambye and K. Riesselmann, *Matching conditions and Higgs mass upper bounds revisited*, Phys. Rev. D **55** (1997) 7255.
- [5] The LEP Collaborations ALEPH, DELPHI, L3, OPAL, the LEP Electroweak Working Group and the SLC Heavy Flavour Group, hep-ex/0312223, (Prepared from contribution of the LEP and SLD Experiments to the 2003 Summer Conferences).
- [6] S. Söldner-Rembold, *Standard Model Higgs Searches and Perspectives at the Tevatron*, submitted to proceedings of Les Rencontres de Physique de la Vallee d'Aoste, Italy, 5-11 March 2006.
- [7] T. Appelquist and C.W. Bernard, Phys. Rev. **D22** (1980) 2000.
- [8] Results presented at the XXXth International Conference on High Energy Physics, Osaka (2000).
- [9] G. 't Hooft *Recent Developments in Gauge Theories*, ed. G. 't Hooft et al. (Plenum Press, 1980).
- [10] P. Ramond, Phys. Rev. **D3** (1971) 2415.
- [11] P. Fayet, S. Ferrara, Phys. Rep. **C32** (1977) 249.
- [12] A.P. Heinson (for the CDF and DØ Collaborations), *Top Quark Mass Measurements*, Fermilab-Conf-06/287-E DØ Note 5226 August 2006.
- [13] P. Horava, E. Witten, Nucl. Phys. **B460**, 569 (1996).
- [14] C. Jarlskog *Phenomenology of CP violation*, eds. J. Bernabeu, A. Ferer, J. Velasco, World Scientific.

- [15] G. Altarelli and M. L. Mangano (editors), *Proceedings of the Workshop on Standard Model Physics (and more) at the LHC* (2000) CERN 2000-004.
- [16] The LHC Study Group, *Large Hadron Collider Conceptual Design*, CERN/AC 95-05, 1995.
- [17] T. S. Virdee, *Detectors at LHC*, Phys. Rept. **403-404** (2004) 401-434.
- [18] The ATLAS Collaboration : *ATLAS Detector and Physics - Performance Technical Design Report*, Vol. I, CERN/LHCC 99-14, 1999.
- [19] The CMS Collaboration, *The Compact Muon Solenoid - Technical Proposal*, CERN/LHCC 94-38, 1995.
- [20] ALICE collaboration, *ALICE technical proposal*, CERN/LHCC 95-71 LHCC / P3, 1995
- [21] LHCb collaboration, *LHCb technical proposal*, CERN/LHCC 98-004 LHCC / P4, 1998.
- [22] TOTEM Collaboration, *TOTEM - Technical Design Report*, CERN/LHCC 2004-002 (2004).
- [23] M. Spira and P. M. Zerwas, *Electroweak Symmetry Breaking and Higgs Physics*, CERN-TH/97-379 (1997).
- [24] B. Muller, *The physics of the Quark Gluon Plasma*, Lecture Notes in Physics (1985) 255.
- [25] The CMS Collaboration, *CMS Physics - Technical Design Report* Volume 1, CERN/LHCC 2006-001, 2006.
- [26] The CMS Collaboration, *The Magnet Project - Technical Design Report*, CERN/LHCC 97-10, CMS TDR 1 (1997).
- [27] The CMS Collaboration, *The Tracker Project - Technical Design Report*, CERN/LHCC 98-6, CMS TDR 5 (1998).
The CMS Collaboration, *Addendum to the CMS Tracker TDR*, CERN/LHCC 2000-016, CMS TDR 5 Addendum (2000).
- [28] The CMS Collaboration, *The Electromagnetic Calorimeter - Technical Design Report*, CERN/LHCC 97-33, CMS TDR 4 (1997).
- [29] The CMS Collaboration, *The Hadron Calorimeter - Technical Design Report*, CERN/LHCC 97-31, CMS TDR 2 (1997).
- [30] The CMS Collaboration, *The Muon project - Technical Design Report*, CERN/LHCC 97-32, CMS TDR 3 (1997).

- [31] Y.N. Pestov e G.V. Fedotovich, Preprint IYAF 77-78, SLAC Translation 184 (1978).
- [32] R. Santonico e R. Cardarelli: *Development of Resistive plate counters*, University of Chicago, E. Fermi Institute('04), Nucl. Instr. and Meth. 187 (1981);
R. Santonico e R. Cardarelli: *Progress in Resistive plate counters*, Nucl. Instr. and Meth. A 263 (1988).
- [33] W. R. Leo, *Techniques for Nuclear and Particle Physics Experiments*, 1987
- [34] A. von Engel, *Ionized Gases*, Clarendon Press, Oxford, 1955.
- [35] W. Price, *Nuclear Radiation Detection*, McGraw-Hill, New York (1958).
- [36] M. Maggi, *Preliminary results on double-gap RPC in a high background environment*, Proceedings at the IV International Workshop on RPC and related detectors, Napoli (1997).
- [37] M. Abbrescia et al., *A Model for the simulation of RPCs in avalanche mode*, Proceeding in the 4th International Workshop on Resistive Plate Chambers and Related Detectors, Napoli 1997.
- [38] M. Abbrescia et al., *The Simulation of RPCs in avalanche mode*, Proc. of the 4th Int. Workshop on RPC and Related Detectors, Napoli, Italy, 15-16 Oct. 1997.
- [39] G. Bruno, *A Simulation Study of the RPC Muon Trigger for CMS*, CMS Note;
M. Abbrescia et Al.: *The Resistive Plate Chambers for CMS and their simulation*, Nucl. Instr. and Meth. A 471 (2001).
- [40] M. Abbrescia et al., *Resistive Plate Chambers in avalanche mode: a comparison between model predictions and experimental results*, Preprint submitted to Elsevier Preprint 1997.
- [41] P. Vitulo et al., *Properties of Bakelite surfaces*, Proceeding in the 4th International Workshop on Resistive Plate Chambers and Related Detectors, Napoli 1997.
- [42] A. Paoloni et Al.: *RPC operation at high temperature*, Nucl. Instr. and Meth. A 508 (2003).
- [43] M. Abbrescia et Al.: *Production and quality control of the barrel RPC chambers of the CMS experiment*, submitted to Nucl. Instr. and Meth.
- [44] R. Trentadue, Ph.D Thesis, Università degli studi di Bari, 2005.

- [45] M. Abbrescia et al., *The simulation of resistive plate chambers in avalanche mode: charge spectra and efficiency*, Nucl. Instr. and Meth. A 431(1999) 413-427.
- [46] M. Abbrescia et al., *Properties of C₂H₂F₄ based gas mixtures for avalanche mode operation of Resistive Plate Chambers*, CMS Note 97/004.
- [47] P.Camarri et al., *Streamer suppression with SF₆ in RPCs operated in avalanche mode*, Nucl. Instr. and Meth. A 414 (1998).
- [48] G. Pugliese, *The RPC System for the CMS Experiment*, at the IEEE Conference, San Diego 1-November 2006.
- [49] A. Sharma et al., *Beam test of the first production forward RPC*, CMS NOTE 2004/037.
- [50] M. Abbrescia et Al.: *Effect of the Linseed Oil Treatment on the Performance of the Resistive Plate Counters*, CMS NOTE-1997/018 .
- [51] The CMS Collaboration, *The Trigger and Data Acquisition project, Volume1 - Technical Design Report*, CERN/LHCC 2000-38, CMS TDR 6.1 (2000).
- [52] The CMS Collaboration, *The Trigger and Data Acquisition project, Volume2 - Technical Design Report*, CERN/LHCC 2002-26, CMS TDR 6.2 (2000).
- [53] V. Brigljevic et al., *Using XDAQ in Application Scenarios of the CMS experiment*, CMS conference report 2003/007.
- [54] V. Brigljevic et al.: *Run Control and Monitor System for the CMS Experiment*, CERN, Geneve, Svizzera.
- [55] J. Varela: *Integration of Run Contrl and Detector Control Systems*, CMS internal note 2005/015.
- [56] S.Luders, R.B.Flockhart, G. Morpurgo, S.M. Scheling: *The CERN Detector Safety System for the LHC experiments*, CERN, Geneve, Svizzera.
- [57] CERN Safety Alarm Monitoring (CSAM), see <http://st-div.web.cern.ch/st-div/Groups/ma/se/CSAM/CSAM.htm>
- [58] P. Gras et al., *Front end electronics configuration system for CMS*, eConf C011127 (2001) WEDT 005.
- [59] A. Daneels and W. Salter, *What is SCADA?*, Int. Conf. on Accelerator and Large Experimental Physics Control System, Trieste, 1999.

- [60] Beate Briss, Matthias Schagginger, Leo Knipp *PVSS II - Getting Started - Basics* Version 2.0 (July 2004).
- [61] JCOP Framework Team: *JOINT CONTROLS PROJECT (JCOP) FRAMEWORK SUB-PROJECT GUIDELINES AND CONVENTIONS*, CERN-JCOP-2000-008.
- [62] CAEN: *User's Manual MOD. SY 1527 UNIVERSAL MULTICHANNEL POWER SUPPLY SYSTEM*, 6 October 2005 Revision n. 13, Italy.
- [63] CAEN: *User's Manual MOD. EASY3000/4000 EMBEDDED ASSEMBLY POWER SUPPLY SYSTEM*, 9 May 2006 Revision n. 9, Italy.
- [64] CAEN: *Technical Information Manual - OPC SERVER FOR CAEN POWER SUPPLIES Release 2.X*, Revision n. 4, 14 October 2003, Italy.
- [65] CAEN: *Technical Information Manual - MOD. A3512 6 CH 12 kV / 1 mA POWER SUPPLY BOARD*, Revision n. 4 , 26 October 2005, Italy.
- [66] CAEN: *Information Manual - MOD. A3009/A3009B 12 CH 8 V / 9 A / 45 W POWER SUPPLY BOARD*, Revision n. 7, 3 January 2006, Italy.
- [67] Analog Devices: *Low Cost, Precision IC Temperature Transducer: AD592*, data sheet, printed in USA.
- [68] I. Crotty, F. Hahn, G. Iaselli, S. Nuzzo : *RPC Gas Distribution Layout*, CMS Internal Note, May 11, 2001.
- [69] CAEN: *Technical Information Manual - MOD. A3801A 128 CH TEMPERATURE SENSOR BOARD*, Revision n. 2, 12 September 2006, Italy.
- [70] F. Glege, R. Gómez-Reino, J. Varela: *CMS DCS Integration Guidelines - Version 2.0*, April 2006, Geneva
- [71] See <http://cdsweb.cern.ch/record/950801> for reference.
- [72] S.Zelepoukine: *ECAL DCS in MTCC phase 1 (operational experience report)*, at CMS DAQ/DCS CERN, 19 September 2006, CERN.
- [73] P. De Barbaro *MTCC Report - HCAL Subsystem*, at the jetMET meeting, 9 November 2006, CERN.
- [74] V. Sytnik: *CSC-DCS status in MTCC*, at CMS week September 2006, CERN.
- [75] M. Passaseo: *DT trigger in MTCC*, at L1 Trigger: Commissioning and Emulator, 30 August 2006, Padova (Italy).

- [76] I. Segoni for RPC group: *RPC in MTCC*, at CPT-MTCC meeting, November 2006, CERN.
- [77] W. Van Doninck (Editor-in-chief):*CMS Bulletin*, number 06-03, 18 September 2006, CERN.
- [78] A. Ball: *MTCC I and II Lessons Learnt Documentation*, at Run Meeting, 10 November 2006,CERN